

## **Analytical Methods in Diffusion Studies**

**Daniele J. Cherniak**

*Department of Earth and Environmental Sciences  
Rensselaer Polytechnic Institute  
chernd@rpi.edu*

**Richard Hervig**

*School of Earth and Space Exploration  
Arizona State University*

**Jürgen Koepke**

*Institut für Mineralogie  
Leibniz Universität Hannover*

**Youxue Zhang**

*Department of Geological Sciences  
University of Michigan*

**Donggao Zhao**

*Department of Geological Sciences  
University of Texas at Austin*

### **INTRODUCTION**

In this chapter, we provide an overview of analytical methods used in diffusion studies. These methods fall into two broad categories – direct profiling and bulk release/exchange. Direct profiling methods, where the concentration of diffusant vs. depth is determined, can employ a variety of techniques, and can access diffusivities ranging from  $\sim 10^{-9}$  to  $10^{-24}$  m<sup>2</sup>/s. Among these methods are the “classical” techniques of serial sectioning and autoradiography, which, despite a long history of application in diffusion studies, are now rarely used, having been superseded by other analytical methods with better depth resolution and greater flexibility. Direct profiling can also be subdivided into methods involving step-scanning, with measurements made by stepping across a sample cut normal to the diffusion interface, and depth profiling, where analyses are performed parallel to the diffusion direction. Step-scanning may be used in cases where diffusion profiles are at least many tens of micrometers long, as it is limited by the beam spot size (typically  $\geq 2$   $\mu$ m; although transmission electron microscopes have much better spatial resolution, they are not used extensively in diffusion studies due to the difficulties in sample preparation) of the analytical tool used and the minimum number of points necessary to define the diffusion profile. The electron microprobe is used for diffusion measurements by step-scanning, as is the ion microprobe (Secondary Ion Mass Spectrometry, SIMS), and IR spectroscopy. SIMS instruments can also be used in depth profiling mode when smaller diffusion distances are measured. The accelerator-based ion beam techniques Rutherford Backscattering Spectrometry (RBS), Nuclear Reaction Analysis (NRA) and Elastic Recoil Detection (ERD) are also applied in measuring short diffusion distances. This group of techniques is capable of high depth resolution ( $\sim 10$  to a several tens of nm) and thus can be used

to measure the slow diffusivities characteristic of many species in minerals. In addition, other promising techniques have been developed, including synchrotron x-ray fluorescence (SRXRF), primarily used in measuring diffusion in glasses, and laser-ablation inductively coupled mass spectrometry (LA-ICPMS), which is being applied in diffusion studies of minerals and metals.

In the other broad group of methods, involving bulk release or exchange, mineral grains or crushed fragments of material are exposed to a reservoir containing a radiotracer or isotopically tagged tracer (typically an aqueous solution or gas source, depending on the diffusing species), with the degree of exchange determined using mass spectrometry (in the case of tracer isotopes) or counting of activity (in the case of radiotracers). Variants of these methods have been used, for example, in early studies of C and O diffusion in carbonates (e.g., Anderson 1969, 1972) and alkali diffusion in feldspars (e.g., Foland 1974; Lin and Yund 1972), more recently in sulfur diffusion in sulfides (Hoeppener et al. 1990), and for oxygen diffusion in a variety of mineral phases (e.g., Hayashi and Muehlenbachs 1986; Fortier and Giletti 1991). However, such “bulk exchange” methods have several limitations, including the difficulty in evaluating diffusional anisotropy, and of sorting out potential contributions from transport along extended defects or other diffusional “fast paths” from those of lattice diffusion when profiles are not directly measured. In addition, assumptions are often made regarding diffusion models used to evaluate diffusivities, the effective surface areas of crushed grains or powders, and compositions of reservoirs acting as sources or sinks for the diffusing species.

A similar approach, involving bulk loss, is taken in measuring noble gas diffusion in minerals. The gas released from sized mineral grains or grain fragments over a series of heating steps is measured by mass spectrometry, with the amount of gas released under these controlled time-temperature conditions used to calculate diffusivities. These methods, with numerous refinements, have been used over many decades to characterize diffusion of Ar (e.g., Fechtig and Kalbitzer 1966; Giletti 1974; Harrison 1981; Foland and Xu 1990; Baldwin et al. 1990; Lovera et al. 1991; Grove and Harrison 1996; McDougall and Harrison 1999) and He (e.g., Wolf et al. 1996; Reiners and Farley 1999; Farley 2000; Shuster et al. 2003; Reiners et al. 2004; Boyce et al. 2005; Blackburn et al. 2007; Farley 2007) in a range of mineral phases.

Along with these methods, a variety of “indirect” techniques have been used to evaluate diffusion coefficients in minerals, including observation of homogenization of exsolution lamellae in feldspars and pyroxene, which have provided information about K-Na and NaSi-CaAl interdiffusion in feldspars (e.g., Brady and Yund 1983; Grove et al. 1984; Yund 1986; Liu and Yund 1992; Baschek and Johannes 1995), and Ca-Mg diffusion in pyroxene (Brady and McCallister 1983), electron paramagnetic resonance to constrain Al diffusion in quartz (Pankrath and Flörke 1994), electrical conductivity measurements to determine diffusivities of alkalis in quartz (e.g., Verhoogen 1952), and study of Fe-Mg reaction kinetics between M1 and M2 sites in orthopyroxene to infer Fe-Mg interdiffusion coefficients (Ganguly and Tazzoli 1994).

Analytical methods used in diffusion studies of geological materials have previously been reviewed by Ryerson (1987). Since that time, SIMS instruments have made considerable technological advances with the development of Focused Ion Beam and nanoSIMS capabilities, which further improve spatial resolution. Accelerator-based ion beam techniques have found increased application in diffusion studies of geological materials, with RBS used to measure diffusion of many medium to heavy elements in a variety of mineral phases, and NRA employed in the investigation of diffusion of light elements and isotopic tracers; additional refinements of extant methods have enhanced their utility in studying geological samples. Improvements in instrumentation and analytical protocols have also benefited the application of IR spectroscopy, synchrotron XRF, and electron microprobe analysis in measurement of diffusion profiles.

In the sections that follow, we will present a brief overview of several analytical techniques, beginning with classical approaches of serial sectioning and autoradiography, followed by the

electron microprobe, secondary ion mass spectrometry, laser ablation ICPMS, accelerator-based ion beam methods (RBS, NRA and ERD), IR spectroscopy, and synchrotron XRF. In each section, the basic principles of the techniques will be outlined, along with practical considerations for their use in diffusion studies and examples of applications.

A brief summary of the quantitative analytical capabilities of each instrument or method as applied in geological studies is given below.

- **Serial Sectioning and Autoradiography:** For measurement of radioactive tracer isotopes with resolution to about a micrometer, for diffusivities down to  $\sim 1 \times 10^{-18}$  m<sup>2</sup>/s.
- **Electron Microprobe (EMPA):** For analyses of major and minor elements from Be to U with spatial resolution of a few micrometers, for diffusivities down to  $\sim 1 \times 10^{-17}$  m<sup>2</sup>/s.
- **Ion Microprobe (SIMS):** For analyses of essentially all elements and isotope ratios at major or trace level with spatial resolution of about 10  $\mu$ m in step-scanning mode and about 20 nm in depth profiling mode. Newly developed nanoSIMS has the potential to improve spatial resolution.
- **Laser Ablation Inductively Coupled Mass Spectrometry (LA-ICP-MS).** For analyses of essentially all elements and isotope ratios at major or trace level with spatial resolution of a few tens of micrometers in step-scanning mode and about 0.5  $\mu$ m in depth profiling mode.
- **Rutherford Backscattering Spectroscopy (RBS):** For analyses of heavy to medium-mass elements in a matrix of predominantly lighter elements, in depth profiling mode with depth resolution to  $\sim 10$  nm.
- **Nuclear Reaction Analysis (NRA):** For analyses of light to medium-mass elements (H to  $\sim$ Ti) and isotopes in depth profiling mode, with depth resolution  $\sim 10$ -50 nm.
- **Elastic Recoil Detection (ERD):** For analyses of light elements (H to Ne) in depth profiling mode, with depth resolution  $\sim 20$ -50 nm.
- **Infrared Spectroscopy and Raman Spectroscopy:** For analyses of H- and C-bearing species such as OH, H<sub>2</sub>O, NH<sub>3</sub>, NH<sub>4</sub><sup>+</sup>, CO<sub>2</sub>, CO<sub>3</sub><sup>2-</sup> in glasses and minerals in step-scanning mode, with spatial resolution of a few tens of micrometers.
- **Synchrotron X-ray Fluorescence Microanalysis ( $\mu$ -SRXRF):** For analyses of heavy elements (from Mn to Pb) in step-scanning mode, with spatial resolution of  $\sim 2$   $\mu$ m depending on capillary used and sample geometry.

## “CLASSICAL” METHODS FOR MEASURING DIFFUSION PROFILES USING RADIOACTIVE TRACERS

### Serial sectioning

The technique of serial sectioning has long been used in diffusion studies (e.g., McKay 1938; Miller and Banks 1942), coming into use in the mid-1930s with the availability of artificial radioisotopes produced in accelerators, and later in nuclear reactors. The first applications were in the area of materials science, studying self-diffusion in metals. Among geologically significant materials, the method has been used primarily in investigations of simple oxides (e.g., Lindner and Parfitt 1957; Chen and Peterson 1975, 1980, Peterson et al. 1980), fluorides (Baker and Taylor 1969; Berard 1971), phosphates (e.g., den Hartog et al. 1972), sulfide minerals (e.g., Gobrecht et al. 1967; Chen and Harvey 1975), glasses (e.g., Jambon 1983; Magaritz and Hofmann 1978a;b), as well as a variety of silicates (e.g., Sippel 1963; Sneeringer et al. 1984; Behrens et al. 1990; Morioka and Nagasawa 1991; Morioka et al. 1997).

The method is employed by depositing a radioactive tracer on a sample surface or otherwise exposing the surface to the radiotracer, performing the diffusion anneal, then sequentially removing sample material in the direction normal to the diffusion direction, for a “one-dimensional” configuration to measure diffusion. The sequential removal of material is typically performed by grinding or dissolution. The thickness or weight of material removed is measured at each step, and the concentration of diffusant is measured either in the material removed or the remaining portion of the sample (with the latter called the residual method). Since a radiotracer is generally used as the diffusing species, the activity of the tracer measured is used to determine its concentration, for example with a scintillation detector for  $\gamma$  radiation and a surface-barrier detector for  $\beta$  particles.

Serial sectioning tends to have relatively limited depth resolution, with resolution constrained by the thickness of the material that can be reproducibly removed and adequately quantified. If only the activity of the removed portion is measured, this results in a stepped, rather than smooth, profile, with step width dependent on the thickness of the removed layers. Better depth resolution can be obtained with the residual method, where both the thickness removed and the activity in the remaining material are measured, but the limitations in depth resolution are ultimately based on the amount of material that can be sequentially removed and evaluated, so depth resolutions are typically larger than 0.5  $\mu\text{m}$ , with the finest scale range achieved by measurement with micrometers or careful weighing of materials having well-known density and fixed geometries. Diffusivities down to  $\sim 1 \times 10^{-19}$   $\text{m}^2/\text{sec}$  have been achieved for Sr in diopside (Sneeringer et al. 1984) and to  $\sim 3 \times 10^{-20}$   $\text{m}^2/\text{sec}$  for Ce diffusion in obsidian (Jambon 1983); but the latter approach (involving HF etching of the glass), is not applicable for most silicate minerals.

Along with limitations in depth resolution, other potential problems with the serial sectioning method include the possible presence of diffusional fast paths, which cannot always be readily distinguished from volume diffusion when relatively coarse-scale depth profiling methods are used. Surface diffusion of the tracer to the back and sides of samples can also occur, as can transport of the tracer in the volatile components in the salts or solution in which they were deposited on the sample surface. Some of these can be circumvented by low-temperature anneals to stabilize the diffusant in a near-surface layer, and by grinding away sample sides and edges to remove surface-diffused tracer. Another practical problem is the availability and expense of suitable radiotracers, as well as radiation safety considerations.

### **Autoradiography**

Autoradiography is another radiotracer method, based on the detection of distributions of radiotracer species with photographic emulsions or other spatially sensitive detectors. The species detected may be from decay of radiotracers, or from fission of high-Z (where Z is the atomic number) elements during neutron irradiation. Typically, diffusion samples are cut parallel to the diffusion direction, polished and placed in contact with a track detector. Most studies employing this method have used beta-emitting radiotracers, such as  $^{14}\text{C}$ ,  $^{61}\text{Ni}$ ,  $^{151}\text{Sm}$ ,  $^{45}\text{Ca}$  (e.g., Hofmann and Magaritz 1977; Medford 1973; Watson 1979a,b, Watson et al. 1982); Seitz (1973) used mapping of fission tracks from neutron irradiated samples to measure U and Th diffusion in apatite and pyroxene. Track densities from track detectors have been determined by a variety of methods over time, including microdensitometers, optical examination, SEM, or microprobe traverses of silver halide emulsions. Limitations of the technique include broadening of beta distributions due to non-zero beta ranges, multiple decays, where a beta emitter decays to another species that is also a beta-emitter (e.g.,  $^{210}\text{Pb}$  decay to  $^{210}\text{Bi}$ ) which may lead to miscounting, and non-linear detector response, where saturation above certain concentrations may lead to undercounting of the decayed species, and, as in the case of serial sectioning, the availability of radiotracers. Because beta-particle ranges are typically on the

order of 100  $\mu\text{m}$  (International Commission on Radiation Units and Measurements 1984), the length of diffusion profiles must be on the order of 1 mm or more for diffusivities to be reliably determined. Some early data in the literature using the autoradiography method do not meet this criterion, because beta-particle ranges were thought to be much shorter. Profiling using autoradiography does not have the spatial resolution of the serial sectioning method; practical lower limits for diffusivities measured by autoradiography is  $\sim 1 \times 10^{-14} \text{ m}^2/\text{sec}$ .

## ELECTRON MICROPROBE ANALYSIS

Electron microprobe analysis (EMPA), also known as electron probe microanalysis, is an electron microbeam technique used primarily to quantitatively determine the chemical composition of solid materials on the micrometer scale and to qualitatively map elemental distributions in materials. It is an *in situ*, almost non-destructive method, and can be used to determine concentrations of elements from Be to U. Electron microbeam techniques, which also include scanning electron microscopy (SEM), transmission electron microscopy (TEM) and scanning transmission electron microscopy (STEM), use a focused (SEM, EMPA and STEM) or parallel (TEM) electron beam to bombard a sample, and the different types of signals generated by the beam-sample interactions are detected using appropriate detectors. The term “electron microscope” was first used by Knoll and Ruska (1932), who made the concept of an electron lens a reality. Ruska was awarded the Nobel Prize in 1986 for this technical innovation and its development. For further details on SEM, TEM or STEM, readers may refer to Goldstein et al. (2003) and Williams and Carter (1996), two widely-read and recent books on electron microscopy. References for EMPA include Smith (1976), Potts (1987), Reed (1993, 1995, 2005), and the EMPA special issue of *Microscopy and Microanalysis* (2001).

In this section we follow the paths or trajectories of signals, first the electron and then X-ray, to discuss the basic principles, instrumentation and applications of EMPA. We will start from the top of an electron microprobe, at the electron gun, then move down along the electron column to electromagnetic lens and beam current and regulation, and then move down further to the sample chamber, vacuum system, and electron beam-sample interaction. Once the electron-induced X-ray is generated, we will shift our discussion to X-ray detection in EMPA, i.e., the wavelength dispersive spectrometer (WDS), and matrix effects. Finally we will present a few examples to illustrate the applications of EMPA in diffusion studies of geological materials.

### Principles of EMPA

The development of the first electron microprobe was reported by Castaing (1951) in his Ph.D. thesis at the University of Paris. An electron microprobe allows elemental concentrations on the micrometer-scale in materials to be measured routinely at levels as low as 100 ppm or 0.01 wt%. Using long count times at high beam currents, a detection limit of 10 ppm or 0.001 wt% is achievable for some specific applications, for example the measurement of Ti in quartz for the Ti-in-quartz thermometer (Wark and Watson 2006). The basis for qualitative analysis, i.e., the identification of individual elements, is the so-called Moseley law. The X-rays emitted during inner-shell electron ionization and transition are called characteristic X-rays because their energies and wavelengths are unique to the excited element. Moseley (1913) discovered that the wavelength of the characteristic X-ray emitted from an element is inversely related to its atomic number  $Z$ :

$$\gamma = \frac{B}{(Z - C)^2} \quad (1)$$

where  $B$  and  $C$  are constants that differ for each X-ray family (from different groups of electron shells), and  $\gamma$  is the wavelength of the characteristic X-ray. By comparing the intensity of a

characteristic X-ray from an unknown sample with that from a known standard, quantification of elemental compositions can be achieved.

In EMPA, characteristic X-rays are generated by a focused electron beam that bombards and interacts with solid materials. During inelastic collisions of the incident electrons with atoms in a sample, the incident electrons lose part of their energy. If the lost energy is high enough to overcome the critical ionization energy of an element, it will be able to remove an inner-shell electron from the atom, which leaves an inner-shell vacancy. The removed electron is called a secondary electron. The excited atom is not stable and a higher-shell electron will fall into the vacancy, resulting in release of the extra energy, either as an X-ray photon or as an Auger electron. The generation of the characteristic X-ray from an element is illustrated schematically in Figure 1. EPMA analysis is generally considered to be non-destructive. However, the electron beam can damage soft materials, such as glasses, and cause migration and loss of components in alkali- or volatile-bearing phases, which could result in underestimation of the concentration of such components.

The emission of characteristic X-rays is a relatively inefficient process. Most interactions occur between the primary electron beam and electrons in outer shells of atoms within the sample. The primary beam electrons are decelerated and lose energy under the influence of the electric fields of the outer orbital electrons, resulting in the production of continuous or bremsstrahlung X-rays. This band of continuous X-rays extends in energy from zero up to the incident energy of the electron beam. In this regard, the electron microprobe could be considered as a giant X-ray tube with the sample as the target.

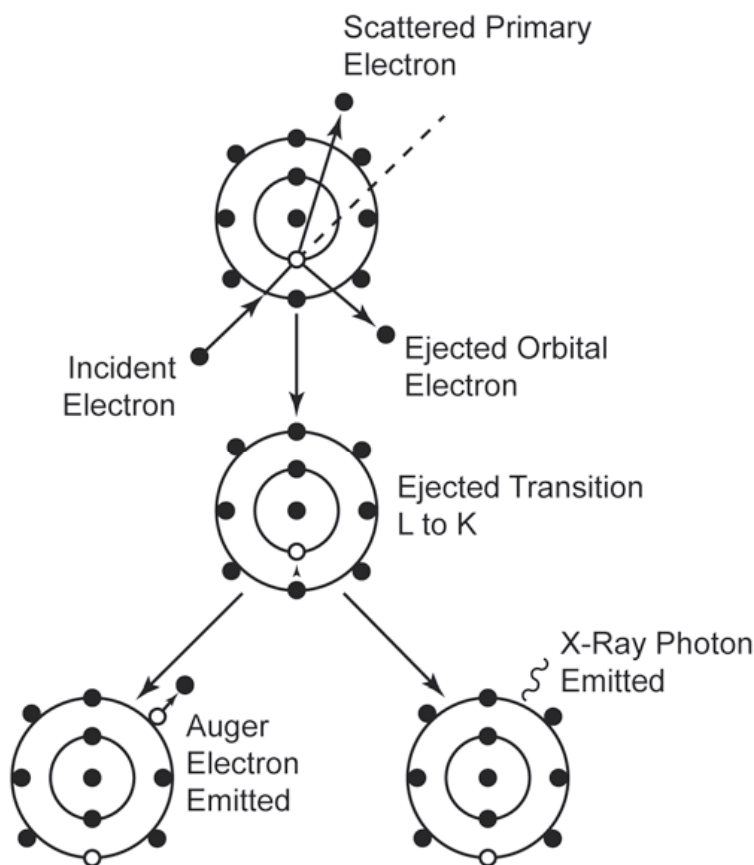


**Figure 1.** Inner shell ionization in an atom and subsequent de-excitation during electron beam-material interaction. The difference in energy from an electron transition is released either as a characteristic X-ray photon or as an Auger electron (from Goldstein et al. 2003).

## Instrumentation for EMPA

The first electron microprobe built by Castaing (1951) used a Geiger counter to detect the X-rays generated from the sample. Since the Geiger counter could not distinguish among different characteristic X-rays, Castaing added a quartz crystal between the sample and the detector to differentiate different characteristic X-rays by using Bragg diffraction. He also added an optical microscope to view the beam impact. The first commercial microprobe was manufactured by Cameca in 1956, and they remain, along with JEOL, as the major electron microprobe manufacturers today.

An electron microprobe consists of the following major components: 1) electron gun, such as a tungsten filament, LaB<sub>6</sub> or field emission gun, used to generate electrons, 2) electron column, composed of a series of electromagnetic lenses, used to manipulate the electron beam in a way similar to light optics, 3) sample chamber with a sample stage adjustable in *x*, *y*, and *z* directions, with a sample exchange door and a variety of detectors around the sample stage, 4) vacuum system for the column and chamber, 5) wavelength dispersive spectrometers (WDS), installed outside of the sample chamber around the electron column, which are used for detecting characteristic X-rays, 6) light microscope for optical observation of the sample, and 7) a control system composed of control interfaces and panel, and computers for data acquisition and processing. In addition to the computer operating system provided by the vendors, some electron microprobes may also use software for data acquisition and processing, for example, Probe for EPMA, previously called Probe for Windows. The components 1 to 4 above are also common constituents of a typical SEM. A modern electron microprobe now includes almost all functions of a SEM, equipped with secondary electron (SE), backscattered electron (BSE) and energy dispersive spectrometry (EDS) detectors, and sometimes with a cathodoluminescence (CL) and/or electron backscattered diffraction (EBSD) system. Hence, an electron microprobe is often considered as a specialized or modified SEM with the addition of wavelength dispersive spectrometers (WDS). Although some SEMs may also be equipped with a WDS detector, the primary applications of a SEM are to acquire images of a sample, and in some cases to qualitatively or semi-quantitatively obtain elemental compositions using an EDS detector, while an electron microprobe is designed primarily for quantitative chemical analysis with spatial resolution on the micrometer scale and detection limits down to 0.001 wt%. Major components of an electron microprobe are shown in Figure 2.

**Electron gun.** There are two types of electron guns - thermionic and field emission guns. Most electron microprobes use thermionic tungsten or LaB<sub>6</sub> filaments, but field emission gun electron microprobes are now also available (MacRae et al. 2006). Thermionic electron emission occurs when the filament material is heated to a temperature of 2600-2700 K so that electrons have a sufficiently high thermal energy to overcome the work function energy of the filament material. A thermionic electron gun is composed of three parts – the filament or cathode at the top, Wehnelt cap in the middle and anode at the bottom. A negative electrical potential (~500 V) is applied to the Wehnelt cap to create so-called space charge, a collection of electrons in the space between the filament tip and Wehnelt cap, and to ensure that electrons only emit from a small area at the tip of the filament. The electrons at the bottom of the space charge emit from a hole in the center of the Wehnelt cap, and then are attracted and accelerated rapidly by high voltage of the anode through the electron column. Between the Wehnelt cap and the anode, the divergent electron beam emitted from the filament is focused into a crossover image of diameter 10 to 100 μm, which is subsequently demagnified by the rest of the electron column. The accelerating voltage of the anode is from 10 to 30 kV for SEM and EMPA and up to 300 kV for TEM and STEM.

The electron gun has to be saturated at the beginning of the probe current plateau in order to preserve long and stable filament life (Fig. 3). A thermionic tungsten filament for an EMPA usually lasts for a few months; high quality of vacuum within the gun area provided

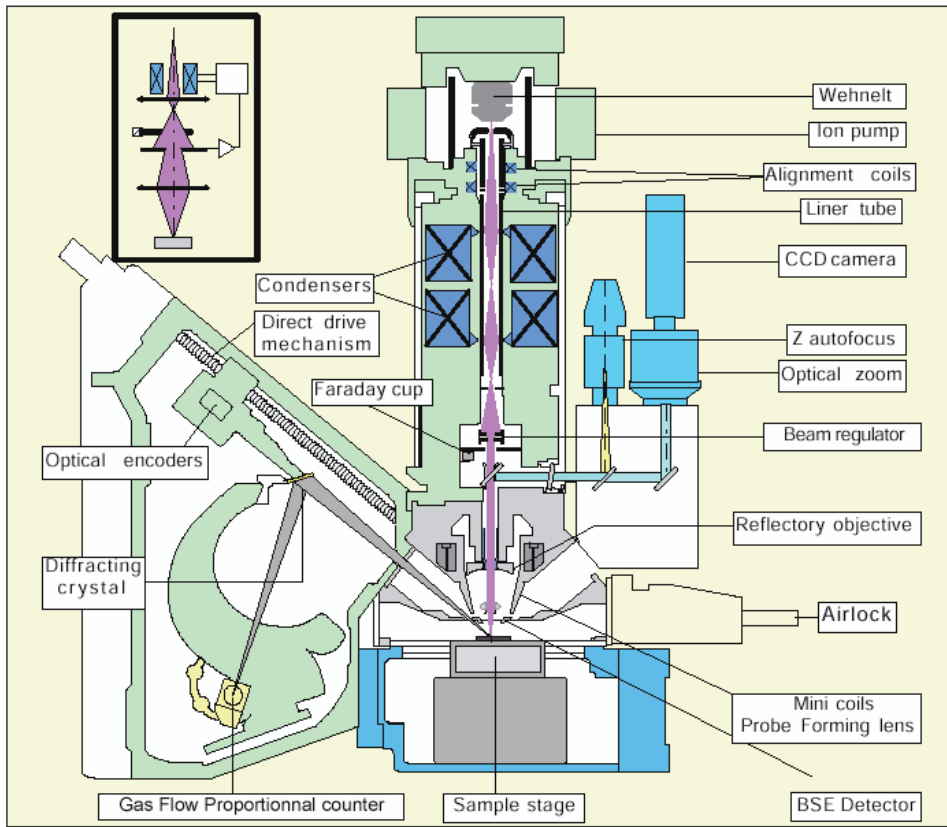


**Figure 2.** (top) Schematic diagram of a Cameca SX50 electron microprobe, showing the electron column with gun and lenses, sample chamber with sample exchange door, control console, and control computer monitors (image from a manual published by Cameca). (bottom) A JEOL JXA-8200 electron microprobe (Photo courtesy of the Electron Microbeam Laboratories at the University of Texas at Austin).

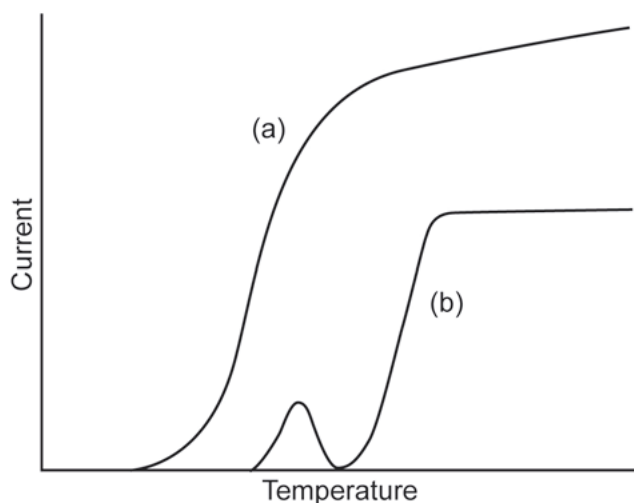


**Figure 3.** Effect of the filament temperature or current (x axis) on electron probe current from the gun (a) and current reaching the sample (b). The gun becomes saturated at the beginning of the current plateau (Reed 2005).

by an ion pump could make a tungsten filament last up to one year. Such a long life time is usually achieved by a LaB<sub>6</sub> filament. Stable emission and long lifetime may also be obtained by positioning the filament further away from the Wehnelt cap.

**Electromagnetic lens.** Electromagnetic lenses are used to focus and demagnify the electron beam emitted from the gun to an electron probe of approximately 1 to 10 nm on the specimen. An electromagnetic lens is composed of a hollow cylinder made from magnetic material, and copper wire coil through which the current is running. The lens is excited by passing a current through the copper coil, creating an intense electromagnetic field across the pole pieces to focus the electron beam. When a negatively charged electron passes through an excited lens, it is deflected to the direction perpendicular to the axis of the lens. This deflection, combined with electron velocity, results in the electron beam being focused at a point on the axis of the lens. Similar to an optical lens, the strength of an electromagnetic lens is measured by its focal length. The stronger the lens, the shorter the distance between focal point and pole pieces.

All lenses suffer from manufacturing defects or imperfections, so an electron beam may never be brought into perfect focus by an electromagnetic lens. Electrons in trajectories further away from the lens axis are bent more strongly by the lens magnetic field than those near the axis. For an imperfect lens, electrons are focused at different points in a horizontal disk rather than at a point where all electron rays converge. This phenomenon is called spherical aberration. Another type of aberration is chromatic aberration, which is caused by variations in the energy of electrons emitted by the gun. Effects of aberrations cannot be completely canceled by using combinations of lenses as in light optics. However, in EMPA the aberration effects can be minimized by using concentric apertures to intercept the unwanted part of the electron beam.

**Beam current and its regulation.** The accuracy of quantitative analysis depends partly on the stability of the electron probe current. Probe current must be regularly monitored and corrected during an analytical session. One way to achieve high current stability over long analytical sessions is to use a beam regulating system. A beam regulator is composed of two apertures. The fraction of the electron beam passing through the first aperture falls on the inner aperture, which is used to continuously monitor the probe current. If this current changes, a signal generated in a feedback circuit will cause the current passing through the condenser lens be adjusted for the current drift.

Several definitions related to current are used in discussions of electron microprobe analyses, and these are often not clearly explained. For example, in analytical methods sections of published papers, both beam current and probe current are used, and they can refer either to a Faraday cup current or the current on sample or on the brass of a sample holder.

To avoid confusion, Potts (1987) distinguished uses of these definitions of current as follows: 1) Filament current is the current used to heat the filament for electron emission. 2) Lens current is the current passing through the coil of an electromagnetic lens. An increase in the lens current causes an increase in the strength of the electromagnetic field, which reduces the focal length. 3) Beam current is the total current emitted by the filament. 4) Probe current is the total current delivered to the specimen, which can be measured by using a Faraday cup, i.e., probe current detector (PCD). The probe current represents only a portion of the original beam current from the filament. The probe current must be maintained at a constant value throughout an analytical session as emphasized above, and is a value that should be reported in published papers. In the literature, probe current is often referred as beam current. 5) Specimen current is the residual fraction of the probe current that stays within the sample. Some of the probe current bombarding the sample is backscattered out of the sample. For a constant probe current, the specimen current may vary from sample to sample depending on the mean atomic number and conductivity of the sample.

**Electron beam-sample interaction.** The capabilities and limitations of electron microprobe analysis are related to interactions that occur within the sample in a volume of approximately  $300 \mu\text{m}^3$ , in which a variety of collisions occur. The region typically has a truncated pear shape (Fig. 4) and is called the interaction or excitation volume. The shape and size of the interaction volume are of interest since they represent the source from which analytical signals originate. The range of electrons and X-rays within a sample depends on the energy of the electron beam and average atomic number of the sample. In addition to inelastic collisions of the incident electrons with atoms in a sample, which result in generation of secondary electrons, X-ray photons and Auger electrons (Fig. 1), a small fraction of the collisions are elastic, in which the primary electrons are scattered back from the sample without losing any appreciable energy. However, the majority of the primary electrons stay in the sample. Because of this, non-conducting samples must be coated with a thin ( $\sim 25 \text{ nm}$ ) layer of carbon to prevent charging of the specimen surface. The transfer of energy during collisions between primary beam electrons and sample atoms may also cause phenomena such as sample heating and emission of photons in cathodoluminescence.

**Wavelength dispersive spectrometers (WDS).** X-ray wavelength dispersive spectrometers (WDS), the key component of an electron microprobe, utilize Bragg diffraction through a diffracting crystal to disperse wavelengths of characteristic X-rays. Once a specific X-ray wavelength is selected, it is focused onto gas-flow or sealed proportional counters for

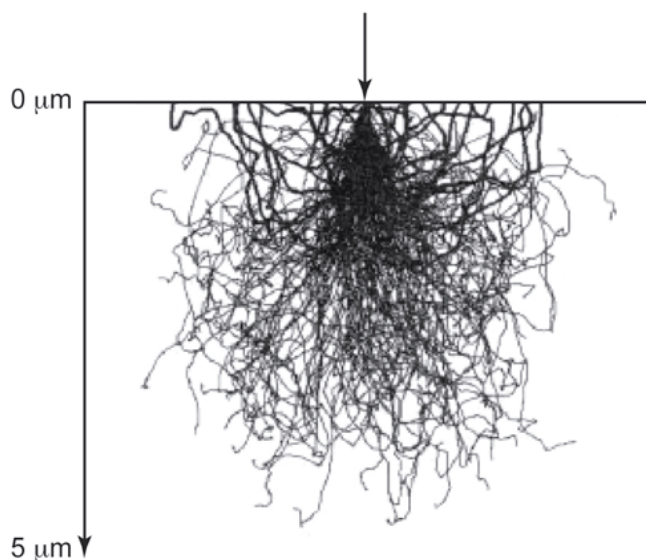


**Figure 4.** Monte Carlo simulations of interaction between a 20 keV electron beam and silicon. The beam electron trajectories that emerge as backscattered electrons are shown as thick traces (Goldstein et al. 2003).

measurement. Only a small portion of the X-ray photons from the sample reach a diffracting crystal; and the intensity of the X-ray in a WDS is generally lower than that in an energy dispersive spectrometer (EDS) detector for a given beam current. For a specific interplanar spacing  $d$  of the diffracting crystal and an X-ray wavelength  $\gamma$ , there is an angle  $\theta$  at which the diffracted characteristic X-rays are in phase and their intensity is constructively enhanced. As illustrated in Figure 5, the wavefront of an X-ray beam approaches the diffracting crystal and is then reflected from the parallel crystal planes. Of the two X-ray paths shown in Figure 5, the difference in path length between these two paths is  $ABC = 2d \sin \theta$  where  $d$  is distance between adjacent lattice planes of the diffracting crystal. If this distance  $ABC$  equals to an integral multiple  $n$  of wavelength  $\lambda$ , then the reflected X-ray beams will be in phase and an intensity maximum will be detected by the proportional counter. This relationship is known as Bragg's law:

$$n\lambda = 2d \sin \theta \quad (2)$$

where  $\theta$  is the angle of incidence of the X-ray beam on the diffracting crystal and  $n$  is the order of reflection. A reflection is called the first order when  $n = 1$ , which is usually the strongest reflection and normally used in EMPA. Higher orders of reflection create unwanted peaks in the WDS spectrum, which can be suppressed by pulse-height analysis (PHA) through a single-channel analyzer (SCA).

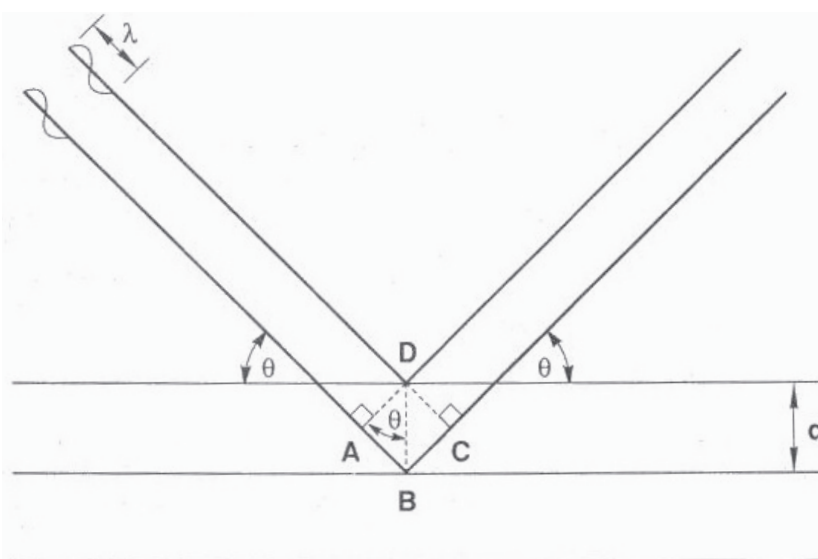


**Figure 5.** Diffraction according to Bragg's law. Strong scattering of X-rays of wavelength  $n\lambda$  occurs only at angle  $\theta$ . At all other angles scattering is weak (Goldstein et al. 2003).

**Diffracting crystals.** Most electron microprobes are equipped with multiple WDS spectrometers with more than one crystal, which are necessary not only for analyzing multiple elements simultaneously, but also for optimizing performance in different wavelength ranges. Figure 6 lists some of the most commonly used crystals from major electron microprobe manufacturers. Mathematics tells us that  $\sin \theta$  cannot exceed unity; therefore, Bragg's law,  $n\lambda = 2d \sin \theta$ , establishes an upper limit of  $2d$  for the maximum wavelength diffracted by a given crystal. More practical limits are imposed by the spectrometer design itself. A lower wavelength limit is imposed by Bragg's equation because it becomes impractical to physically move the diffracting crystal too close to the specimen, which limits the value of theta. Most naturally occurring crystals like LiF are limited to shorter wavelengths because their interplanar spacings are small. Synthetic crystals, like TAP, provide a very useful extension of the measurable wavelength range, but still do not have sufficiently large  $d$  spacings to

Crystal d spacing	2d (nm)	5 B	10 Ne	15 P	20 Ca	25 Mn	30 Zn	35 Br	40 Zr	45 Rh	50 Sn	55 Cs	60 Nd	65 Tb	70 Yb	75 Re	80 Hg	85 At	90 Th
LIF	.4027	[Analysis range bars for LIF]																	
PET	.875	[Analysis range bars for PET]																	
TAP	2.576	[Analysis range bars for TAP]																	
PC0	4.45	[Analysis range bars for PC0]																	
PC1	6.22	[Analysis range bars for PC1]																	
PC2	9.80	[Analysis range bars for PC2]																	
PC3	19.95	[Analysis range bars for PC3]																	

**Kα**                      **Lα**                      **Mα**

LIF Lithium fluoride 200  
 PET Pentaerythritol  
 TAP Thallium acid phthalate

PC0 W/Si Multilayer crystal  
 PC1 W/C Multilayer crystal  
 PC2 V/C Multilayer crystal  
 PC3 Mo/B4C Multilayer crystal

Crystal d spacing	2d (nm)	6 C	14 Si	22 Ti	30 Zn	38 Sr	46 Pd	54 Xe	62 Sm	70 Yb	78 Pt	86 Rn
LIFH	0.4027	[Analysis range bars for LIFH: 20Ca, 31Ga, 50Sn, 79Au]										
LIF	0.4027	[Analysis range bars for LIF: 19K, 37Rb, 48Cd]										
PETH	0.8742	[Analysis range bars for PETH: 14Si, 22Ti, 37Rb, 56Ba, 72Hf]										
PET	0.8742	[Analysis range bars for PET: 13Al, 25Mn, 36Kr, 70Yb, 65Tb]										
TAPH	2.576	[Analysis range bars for TAPH: 9F, 13Al, 24Cr, 35Br, 47Ag, 70Yb]										
TAP	2.576	[Analysis range bars for TAP: 8O, 15P, 24Cr, 46Pb, 41Nb, 79Au]										

**Kα, β**                      **Lα, β**                      **Mα, β, λ**

**Figure 6.** Analysis ranges of crystals for a Cameca electron microprobe (top), and for a JEOL electron microprobe (bottom) (adapted from figures in manuals published by Cameca and JEOL).

cover the longest wavelengths encountered, for example, the  $K\alpha$  for Be, B, C, and N. The measurement of these long wavelengths requires the use of “pseudocrystals,” i.e., layered synthetic microstructures with large  $d$  spacings; lighter elements (H, He and Li) with even longer wavelengths cannot be analyzed by EMPA.

**X-ray source and matrix correction.** For quantitative EMPA, the concentration of a given element in an unknown sample is obtained by comparing the intensity of a characteristic X-ray of the element with that from a standard with known chemical composition. The intensities of an X-ray line of both sample and standard must be corrected for dead time, background and instrumental drift, overlapping and matrix effects in order to obtain accurate results. According to the Castaing approximation, the intensity  $I$  of a characteristic X-ray is proportional to the mass concentration  $C$  of the element measured. To first approximation, the concentration for a given element  $A$  in a sample can be expressed as:

$$C'_A(\text{unknown}) = C_A \left( \frac{I_A(\text{unknown})}{I_A(\text{standard})} \right) \tag{3}$$

where  $C'_A(\text{unknown})$  is the uncorrected concentration in the unknown sample. The ratio  $I_A(\text{unknown})/I_A(\text{standard})$  is called the  $k$  ratio. The measured X-ray intensity of an element in

EMPA is affected by the concentrations of all the other elements present in the sample. These so called matrix effects include the influence of atomic number (Z), X-ray absorption (A) and secondary fluorescence (F) and must be corrected for in order to obtain the actual concentration of an element. There are several matrix correction methods, which include calibration curves, these are Bence-Albee, ZAF and PAP.

In the ZAF correction, the measured X-ray intensity is multiplied by a number of factors that model the influences of the effects listed above. The atomic number correction (Z) deals with differences in the behavior of incident electrons between an unknown sample and a standard, and includes two factors: the stopping power of the sample and backscattering of electrons from the sample. The stopping power is the ability of a material to reduce the energy of an incident electron by inelastic scattering. The transfer of energy from electrons to the sample is related to the generation of X-rays. As a result, the X-ray intensity increases with atomic number. Backscattering of electrons, an elastic process, is strongly affected by atomic number. The effect of backscattering is to decrease the X-ray intensity with increasing atomic number, which is opposite to the effect of stopping power. However, since the backscattering effect is greater; the overall atomic number correction follows the same trend as the backscattering effect. Since these two factors tend to cancel each other, the atomic number correction factors are not very large in most cases. The absorption correction (A) considers effects of the mass absorption coefficient, incident electron energy, and X-ray take-off angle. X-rays are generated throughout the analytical volume during an analysis. X-rays produced at depth must pass through a certain distance within the sample and may be absorbed during that time. Hence, the intensity of X-rays will be reduced by absorption from the elements in the material. In the ZAF correction, absorption is also one of the terms in the correction, and is often the largest correction made to the X-ray intensities in quantitative microanalysis. Therefore, its accuracy most directly influences the accuracy of the quantitative results. In the last few decades much work has been done to describe the absorption correction as a function of the depth distribution of the generated X-rays within the sample. Finally, the fluorescence correction (F) needs to be considered if the characteristic X-rays from an element B have high enough energy to excite another element A. Fluorescence excitation may also be caused by continuous X-rays, but this effect usually is negligible.

The ZAF correction does not account for depth distribution of X-rays and is not very reliable for light elements, i.e., elements with X-ray energies less than 1 keV. A modified ZAF correction procedure called the PAP method (Pouchou and Pichoir 1986a,b, 1988, 1991) can better account for the depth distribution of energies of X-rays produced from a sample. The PAP method uses a modified version of the  $\phi(\rho-Z)$  polynomial used in standard ZAF correction procedures. To further optimize quantitative analyses for elements with low X-ray energies, it is best to use a standard of similar composition to minimize matrix effects, for example, a fluorapatite standard rather than a fluorphlogopite or fluorite standard to analyze F in apatite.

**X-ray proportional counter.** The last major component is the gas proportional counter detector, shown in Figure 7. This highly efficient detector has an excellent dynamic range (0-50,000 counts per second or more) and covers a wide range of energies. It consists of a gas-filled tube with a coaxial thin wire, usually tungsten, held at a 1 to 3 kV potential. When an x-ray photon enters the tube through a thin window, it ionizes atoms of the gas and produces photoelectrons. The photoelectrons are then accelerated towards the anode wire and further ionize other gas atoms producing more electron-ion pairs. This "avalanche" effect produces an amplification of the initial signal, resulting in a charge pulse appearing on the anode. The amplitude or height of the pulse depends on the number of ionizations, which is related to the energy of X-ray photons. If the gas used by the counter is P10 (90% argon-10% methane), approximately 28 eV is needed to create one electron-ion pair. For the Mn  $K\alpha$ , which has an energy of 5.895 keV, about 210 electron-ion pairs will be directly created by the absorption

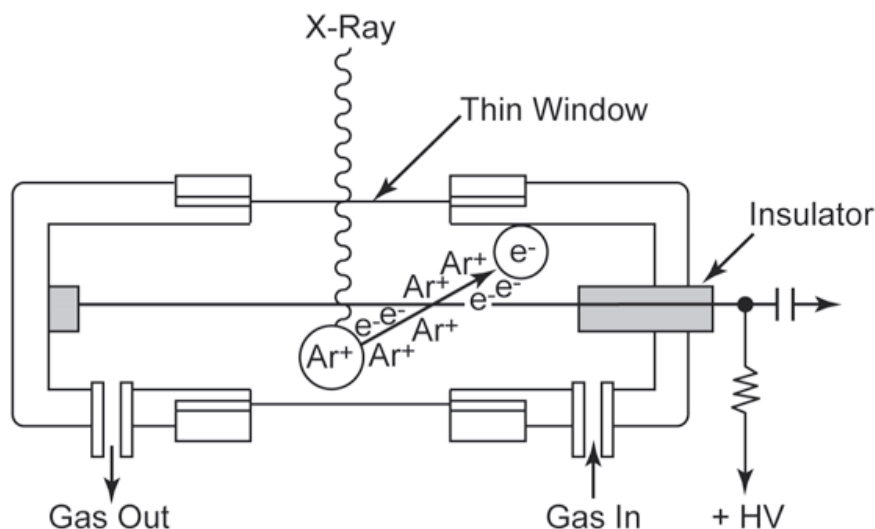


**Figure 7.** Schematic drawing of a gas flow proportional counter as used in WDS (Goldstein et al. 2003).

of a single Mn  $K\alpha$  photon. Electron multiplication in the counter depends on the anode voltage. At certain ranges of anode voltages in the counter, the pulse height is directly proportional to the energy of the incident X-ray.

The voltage distribution of pulses for a pre-selected time period can be obtained using a single-channel analyzer (SCA), which is used to select and transmit pulses within a predetermined voltage range for further processing. The SCA also serves as an output driver, causing the selected pulses to become rectangular pulses of a fixed voltage and time duration. The pulse height analysis process with a SCA is illustrated schematically in Figure 8.

### Applications and limitations of EMPA

Quantitative determination of the composition of an unknown phase by EMPA requires several steps: 1) a setup procedure which includes selection of elements to be analyzed, X-ray lines to be measured, standards and their compositions, accelerating voltage(s), probe current, analytical mode, beam size, diffracting crystals, background, count times, and other parameters, 2) standardization or calibration based on standards of known composition, 3) secondary standard check and evaluation of quantitative results, and 4) analysis of samples and assessment of errors. The EMPA technique is probably mostly used by materials (including earth materials) scientists for accurate chemical analysis of both natural and synthetic materials on small scales (Smith 1976; Potts 1987; Reed 1993, 1995, 2005; Goldstein et al. 2003; Mehrer 2007). For example, variations in elemental concentrations on the micrometer-scale from the center to the edge of a crystal can provide information on the history of crystal growth and elemental diffusion.

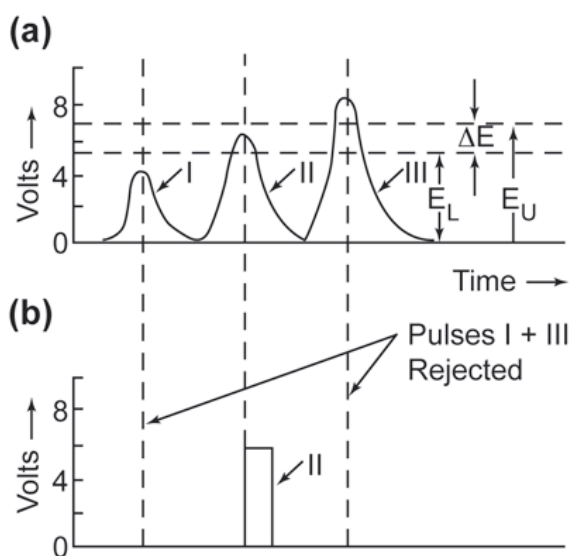


**Figure 8.** Schematic representation of a pulse-height analyzer. a) Main amplifier output; b) single-channel analyzer output.  $E_L = 5$  V;  $\Delta E = 2$  V;  $E_U = 7$  V (Goldstein et al. 2003).

In experimental diffusion studies, elemental concentration profiles are measured using EMPA by stepping across a sample along the diffusion direction (i.e., perpendicular to the diffusion surface or interface), also referred to as line scans. Such scans can be set up automatically by specifying the beginning and ending points and the number of points in between, with equal-distance spacing. If the profile is not perpendicular to the diffusion surface or interface, the distance from each point to the diffusion surface or interface can be calculated or measured optically after the microprobe analyses. Since the spatial resolution of the electron microprobe is a few micrometers, the half-length of the diffusion profile, roughly  $(Dt)^{1/2}$  (e.g., Zhang 2008), must be  $\geq 15 \mu\text{m}$  for the diffusivity to be accurately extracted from the profile (Ganguly et al. 1988). More generally, the half-length of the diffusion profile must be  $\geq 10$  times the spatial resolution (Ganguly et al. 1988). If the length of the diffusion profile is shorter, the averaged concentration that is measured would be significantly different from the actual concentration at the intended point, and the extracted diffusivity may differ significantly from the actual value because of this “convolution” effect.

Due to the constraints on the minimum length of diffusion profiles and practical limits on experimental durations (e.g., experiments lasting no more than 6 months), only relatively large diffusion coefficients ( $D > 10^{-17} \text{m}^2\text{s}^{-1}$ , e.g., Carroll 1991), such as those for diffusion in melts and inter-diffusion of rapidly diffusing elements in minerals, or diffusion at relatively high temperatures, can be measured using EMPA. Smaller diffusivities require other methods, such as Rutherford Backscattering or SIMS in depth-profiling mode.

Figure 9a shows an Ar concentration profile measured by EMPA (Behrens and Zhang 2001). The profile is a result of Ar diffusion into a dry Ar-free rhyolite melt at high Ar pressure and high temperature (Behrens and Zhang 2001). The profile is long and well-resolved. The data can be fit well by an error function (solid curve), indicating that the Ar diffusivity is independent of Ar concentration. Figure 9b shows an interdiffusion profile of FeO measured by EMPA between a high-silica rhyolite (77 wt%  $\text{SiO}_2$ ) and a lower-silica rhyolite (73 wt%  $\text{SiO}_2$ ) melts (Van Der Laan et al. 1994). These data show con-

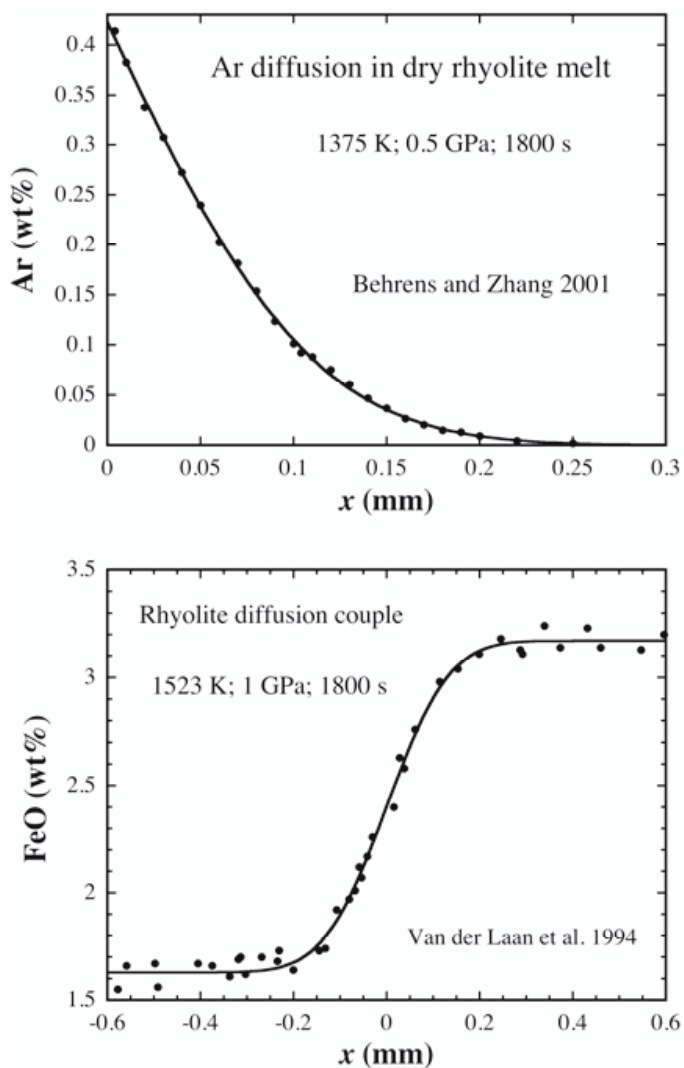


**Figure 9.** Two concentration profiles measured by EMPA. (a) Ar diffusion profile in dry rhyolitic melt (Behrens and Zhang 2001); (b) FeO interdiffusion profile for a rhyolite diffusion couple (Van der Laan et al. 1994). Experimental temperatures, pressures and durations are shown in the figures.

siderably more scatter than the example of Figure 9a. Within uncertainties, the data can also be fit well by an error function (solid curve), allowing the extraction of an effective binary diffusivity. Points analyzed by EMPA can be seen optically after the analyses, and can be used to confirm the spots analyzed (e.g., distance from the surface or an interface) and the distance between points.

The application of EMPA in diffusion studies may be affected by factors such as the phase boundary fluorescence effect (Zhao 1998; Reed 2005). As illustrated in Figure 4, the electron beam-sample interaction volume is limited to a few micrometers in depth. However, the fluorescence volume, in which secondary X-ray fluorescence occurs, is much larger than the interaction volume in which the primary X-rays are generated. When the interaction volume or fluorescence volume crosses a phase boundary, fluorescence corrections of the matrix effects for quantitative analysis may not be correct. For example, in a common mafic and ultramafic assemblage with chromite-olivine pairs (olivine is a common inclusion in chromite hosts), analyses of  $\text{Cr}_2\text{O}_3$  concentrations in tiny olivine inclusions in the chromite host could be affected by secondary fluorescence (Zhao 1998). When the electron beam bombards the olivine, the primary Fe  $K\alpha$  X-ray generated from the olivine will penetrate into a much larger fluorescence volume and may cross the olivine-chromite grain boundary. Since the chromite host has a high  $\text{Cr}_2\text{O}_3$  concentration and the chromium's critical ionization energy, 5.989 keV, is slightly lower than the energy of Fe  $K\alpha$  X-rays (6.403 keV) the Cr in the chromite will be excited by the primary Fe  $K\alpha$  X-rays, and secondary Cr  $K\alpha$  X-rays will be generated and detected. Therefore, the secondary fluorescence of Cr  $K\alpha$  in chromite by the Fe  $K\alpha$  from olivine will dramatically increase the apparent  $\text{Cr}_2\text{O}_3$  concentration of the olivine inclusion, making a correction of  $\text{Cr}_2\text{O}_3$  concentration in the olivine necessary to account for this effect. Figure 10 shows that the apparent increase in  $\text{Cr}_2\text{O}_3$  concentration from the center of the olivine inclusion to the olivine-chromite boundary, illustrating that the apparent  $\text{Cr}_2\text{O}_3$  concentration could be artificially increased even at the center of an olivine inclusion of 50  $\mu\text{m}$  in size. The secondary fluorescence effect was confirmed when higher apparent  $\text{Cr}_2\text{O}_3$

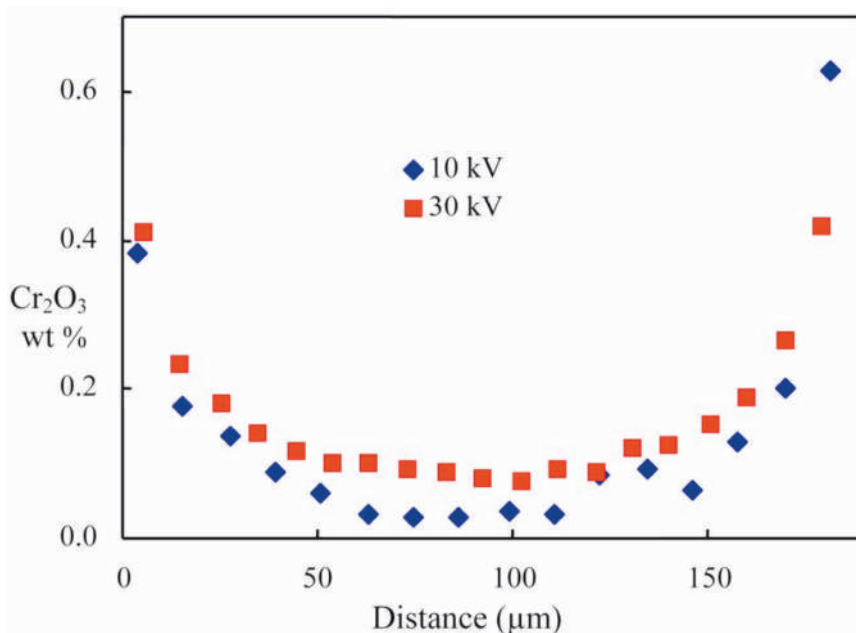


**Figure 10.** Variations of Cr content across an olivine inclusion in a chromite host. The samples were analyzed at two different accelerating voltages — 10 and 30 kV. The apparent increase in Cr concentration toward the chromite-olivine boundary is due to the effect of secondary fluorescence, where X-rays generated from Fe in the olivine excite Cr X-rays in the adjacent chromite. The effect becomes more pronounced with increasing accelerating voltage and when nearer the olivine-chromite boundary (Zhao 1998).

concentrations were obtained for same sample analyzed at 30 kV, a higher energy where the effects of secondary fluorescence are more pronounced. The effects of secondary fluorescence became more evident when the olivine was analyzed after removal of the chromite host, which resulted in  $\text{Cr}_2\text{O}_3$  concentrations for the olivine inclusion of  $\sim 0.10 \pm 0.02$  wt%. Therefore, the phase boundary fluorescence effect must be considered when small mineral inclusions are analyzed by electron microprobe, as well as when performing analyses near interfaces where there are compositional differences and the potential for secondary excitation.

### Summary

Electron microprobes can analyze almost all elements (from Be to U) with a spatial resolution of a few micrometers and a typical detection limit of 100 ppm (with detection limits of 10 ppm achievable for some elements under certain circumstances). They are the most widely used instrument for major and minor element analyses in the geological sciences, but are unable to analyze most elements at trace levels. Furthermore, they are unable to detect the lightest elements (H, He and Li). For example, hydrous components in minerals cannot be analyzed using EMPA. There are also overlaps of X-ray lines for some elements in WDS detection, making quantitative analysis difficult due to these interfering signals. In addition, EMPA cannot distinguish between the different valence states of an element, as in the case of  $\text{Fe}^{3+}/\text{Fe}^{2+}$ .

## SECONDARY ION MASS SPECTROMETRY (SIMS)

Secondary ion mass spectrometry (SIMS), also known as the ion microprobe, is a powerful microanalytical tool. It has found considerable application in characterizing the concentration and distribution of dopants in semiconductors, and is a crucial instrument in quality control (and research and product development) in this industry. The capabilities that make it essential in this context (high sensitivity and depth resolution) also make it well-suited to the characterization of diffusion profiles in geological materials.

### Basic principles of SIMS

In SIMS, atoms from a sample are ejected, or “sputtered” by the impact of energetic (several keV) primary ions on the sample surface. A schematic of this process (based on the Cameca SIMS design; <http://www.cameca.fr/>) is shown in Figure 11. The analyst has a choice of primary ion species and the polarity of the secondary ion beam; different primary beams enhance the ion signal for different elements. For example, elements with high electron affinities (e.g., F, S, As) show the best sensitivity when negative secondary ions are detected and an electropositive primary beam (such as  $\text{Cs}^+$ ) is used, while elements with low ionization potentials (e.g., Li, Be, Y) yield low levels of detection when positive secondary ions are sputtered by an electronegative primary species such as oxygen. The schematic (Fig. 11) shows the effect of changing the primary ions from  $^{16}\text{O}^-$  (most commonly used in geological studies) to  $^{16}\text{O}_2^+$  (most commonly used in the semiconductor industry). Most sputtered atoms are ejected as neutral species, some as molecular ions, some secondary electrons are generated, but some atoms in the sample form elemental ions in the sputtering process. Placing a high voltage on the sample accelerates sputtered ions away from the sample, and into a mass spectrometer where the ions are separated by their mass:charge ratio and then counted. Changing the primary beam polarity has several effects on the analysis, but the two most obvious from Figure 11 are the impact angle and the impact energy. Tutorials on SIMS are available on the web, with one from Evans Analytical Group ([http://www.eaglabs.com/training/tutorials/sims\\_theory\\_tutorial/](http://www.eaglabs.com/training/tutorials/sims_theory_tutorial/)) being commonly used. Sputtered neutral mass spectrometry (SNMS) is a related technique that ionizes the neutral species after ejection from the sample using electron impacts, ion impacts, or lasers. While not discussed in this chapter, the interested reader is referred to Williams and Streit (1986) and Vad et al. (2009).

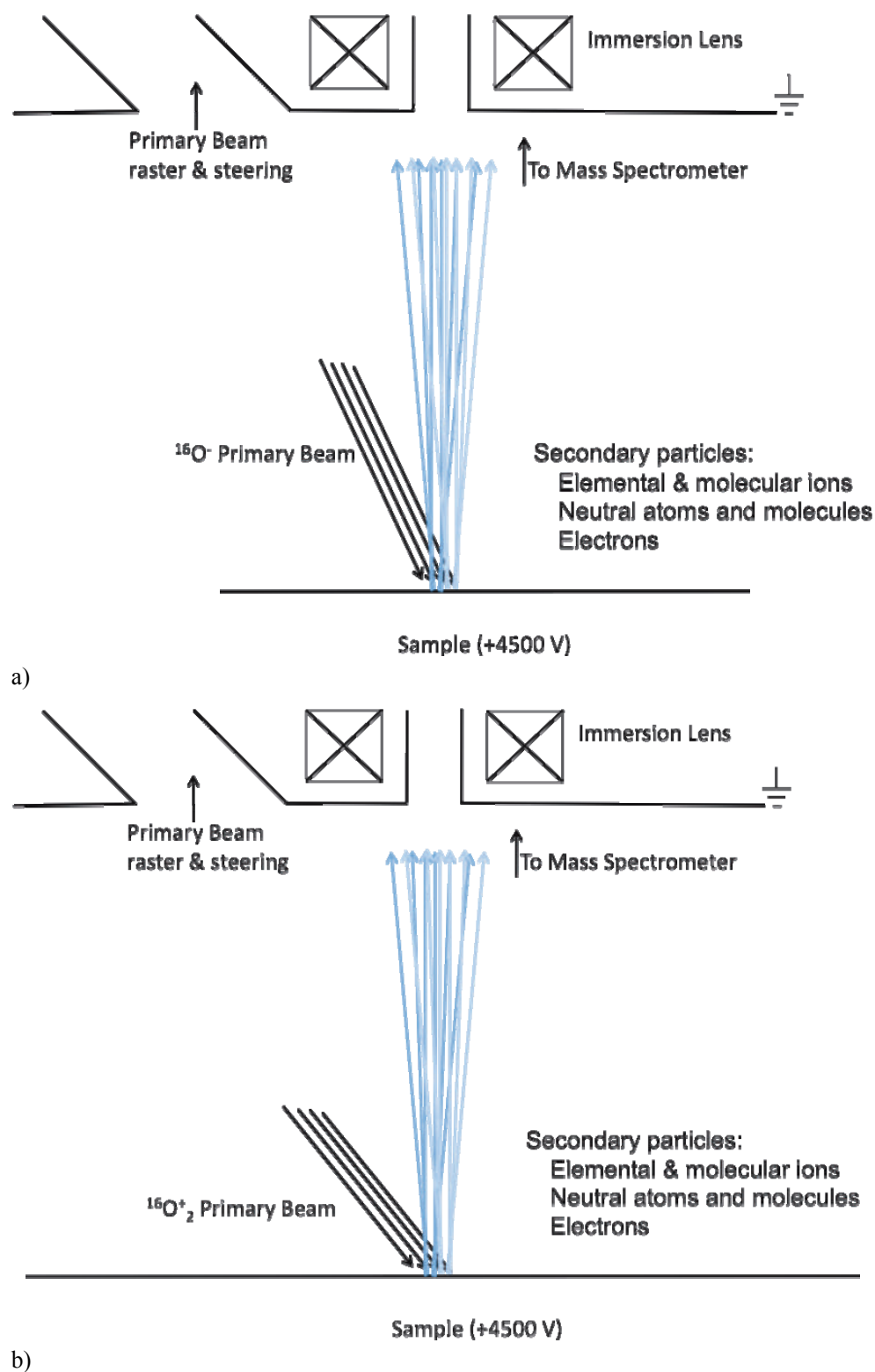


**Figure 11.** Schematic diagram of the sputtering process in SIMS. (a) Sample held at +4500 V and sputtered with a primary beam of  $^{16}\text{O}^-$  ions accelerated from a duoplasmatron held at  $-12.5$  kV. The primary ions strike the sample at an angle of  $\sim 25^\circ$  from the sample normal. (b) Same as (a) except that the primary beam is  $^{16}\text{O}_2^+$  with an impact angle  $\sim 39^\circ$  from the sample normal. Sputtered particles are indicated in light shades. The sample is  $\sim 5$  mm from the grounded plate in front of it. This creates a strong extraction field ( $\sim 1$  V/ $\mu\text{m}$ ) that results in efficient collection of secondary ions but also deflects the primary beam as it encounters this voltage gradient, requiring substantial changes in primary beam steering (not shown) as the primary polarity is changed.

### Using SIMS to measure diffusion profiles

There are two approaches to using SIMS for diffusion studies: 1) line scans and 2) depth profiling. Line scans (or “step” scans) are used in those cases where the diffusion length is many times larger than the diameter of the primary ion beam. In such cases, chemical, isotopic, and tracer diffusion can be determined. Depth profiles are used most often when the diffusion length is less than a few micrometers.

**Line scans.** One example of a diffusion experiment characterized by a line scan is shown in Figure 12. For this study, a platinum capsule was filled with rhyolite powder and melted at 1 atmosphere to produce a nominally dry cylinder of glass. The cylinder was then sealed in a larger capsule filled with  $D_2O$  and taken to 750 bars pressure, 850 °C in a cold seal pressure vessel (where the pressurizing medium was also  $D_2O$ ). Deuterium diffused into the molten rhyolite cylinder for 12 hours, after which the experiment was quenched. The quenched glass cylinder was embedded in epoxy, cut longitudinally, and polished (see Fig. 12). Step scans were conducted using SIMS to determine how far the deuterium had diffused into the silicate melt, and the resulting analytical craters are shown on Figure 12 while Figure 13 displays the analytical results). The different spacings between craters in earlier line scans represent attempts to examine the zoning of different elements and/or to test different analytical parameters. For example, while the experiment was designed to measure the diffusion of  $D_2O$  (and compare to related experiments on  $H_2O$  diffusion) it was realized in the mid-1990s that noble metal capsules are often contaminated with Li and B, so that these samples might show diffusion profiles for other light elements. Subsequent analyses revealed high boron only at the epoxy/glass interface of this 12-hour duration experiment, but the diffusion of Li is pronounced, and reaches the baseline Li concentration in the starting rhyolite at about the same distance as  $D_2O$  (Fig. 13; Hervig, unpublished data).

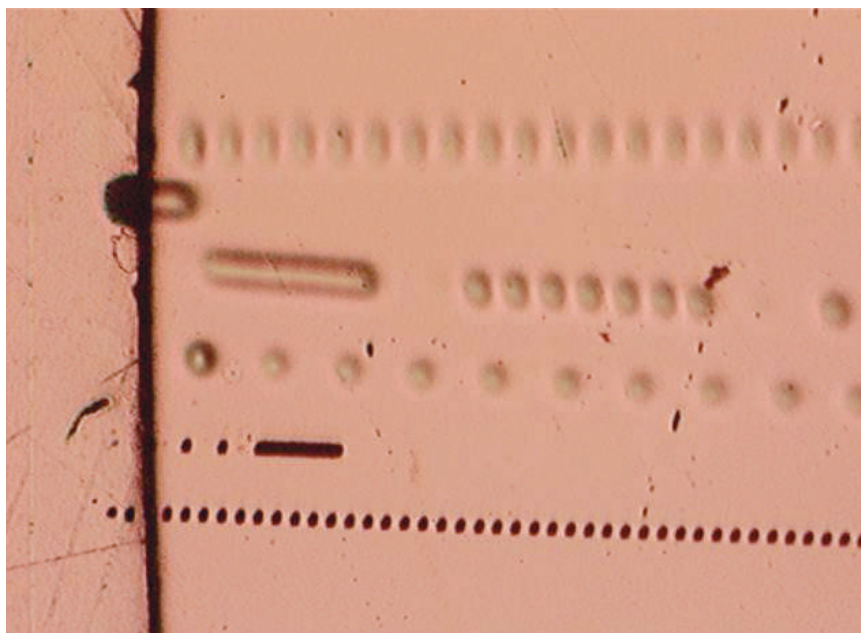


**Figure 12.** Polished sample of rhyolite glass showing several step scans across glass (reflected light image). Note the epoxy mounting medium on the left. The liquid meniscus at 750 bars was convex against the  $D_2O$  fluid. The most recent step scans show up as dark craters. The scan at the bottom represents 25  $\mu m$  steps  $\sim 1400 \mu m$  long ( $\sim 20 \mu m$  beam diameter). Most of the older step scans (illustrating a wide range of step sizes and primary beam diameters as specified by the operator) show brighter craters because the sample was re-coated with gold prior to the most recent work scans (sample from Stanton 1989). All craters were made using a primary beam of  $^{16}O^-$ .

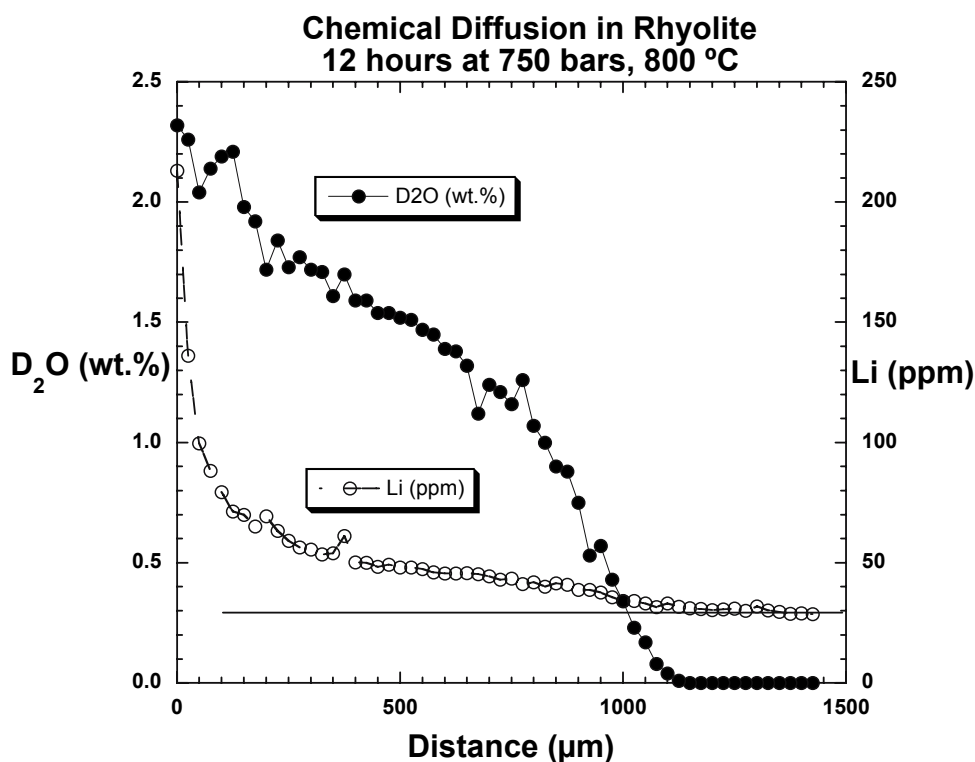


**Figure 13.** Variation in D<sub>2</sub>O and Li contents as determined by the step scan shown in Figure 2 above. The <sup>2</sup>H<sup>+</sup> signal was converted to D<sub>2</sub>O (wt%) by comparison with the <sup>2</sup>H<sup>+</sup> signals obtained on bulk-analyzed rhyolitic glasses synthesized in the presence of D<sub>2</sub>O fluid at different pressures (Stanton 1989). The Li concentration in the starting glass was ~30 ppm (Hervig, unpublished data).

The results in Figure 13 illustrate the capability of SIMS in that both volatile and trace light elements can be determined with a lateral resolution typically around 5-30 μm. The lateral resolution limitations are dominated by the performance of the primary ion source (how small one can focus the beam) and the amount of sample one needs to consume to obtain statistically meaningful analyses on a reasonable time scale (i.e., the useful ion yield; Hervig et al. 2006). The results are also interesting from a diffusion standpoint in that D<sub>2</sub>O shows the well known concentration-dependent, concave-down diffusion profile (Behrens et al. 2007; Ni and Zhang 2008) while the lithium profile is not concentration-dependent, and concave up.

SIMS line scans can also be used for isotopic diffusion (Leshner et al. 1996; Richter et al. 2003). An example from Leshner et al. (1996) is displayed in Figure 14. These experiments required the synthesis of basaltic glasses doped with <sup>30</sup>Si and <sup>18</sup>O and creation of a diffusion couple by placing these nominally anhydrous samples against basaltic glass with normal isotopic abundances. After treating the couple at high pressure and temperature, the experiment was quenched, and the resulting isotopic gradient was characterized using a primary beam of Cs<sup>+</sup> and detection of negative secondary ions. As the results show, there are gaps in the line scan. These are caused by the development of cracks in the glass quenched from high pressure, and point out the need for flat surfaces when making SIMS analyses. If the sample surface is variably tilted, measured ion intensities of different secondary species can change significantly (these outliers were removed from Fig. 14). Careful optical study of run products prior to analysis can reveal areas likely to suffer from such problems. In the case of the data in Figure 14, the results were used to document similar diffusion of silicon and oxygen in high-pressure silicate melts (Leshner et al. 1996). SIMS line scans of the run products from Richter et al. (2003) were used to document gradients in Li content and the Li isotope ratio in a chemical diffusion experiment.

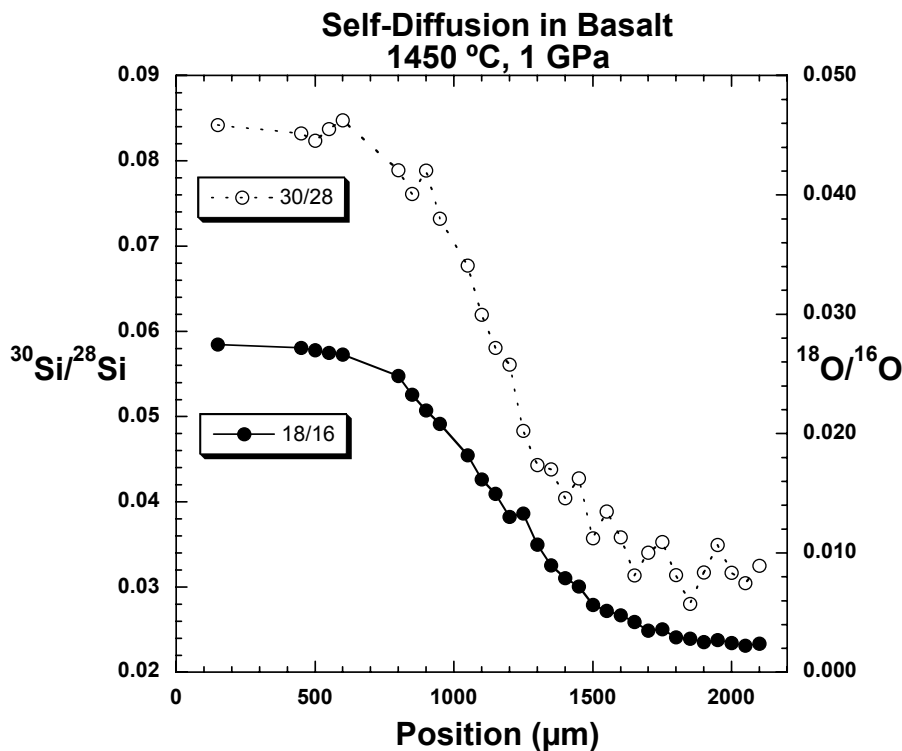


**Figure 14.** Isotopic diffusion of silicon and oxygen in basaltic liquids at 1450 °C, 1 GPa (35 minute duration). The line scans used 50 μm steps, but overlap of the beam on numerous cracks that developed in the run product during quench led to some unusable analyses. The figure was redrawn from published data (Lesher et al. 1996).

**Limitations of SIMS line scans.** Despite the advantages of using SIMS in line-scan mode to measure diffusion profiles, there are prices to pay: 1) analyses take a long time, 2) calibrations may not be linear, 3) molecular ion interferences may be difficult to resolve and may change along the profile, and 4) the diffusion length scale should be much longer than the lateral resolution as defined by the diameter of the primary ion beam.

**Analysis duration.** The time required to collect a measurement of sufficient precision at each analysis point depends on several parameters. One important value is the sputter yield,  $S$ , defined as the atoms ejected from the sample surface/primary ion impact. The sputter yield changes as a function of the target density, primary beam species, and primary beam impact energy. When an analysis is initiated, the addition of the primary beam to the sample changes the chemistry of the target. This leads to significant changes in the observed secondary ion intensities for a few minutes. For each analysis in a line scan, waiting until the ion signals of interest reach steady-state conditions (known as the “pre-sputter” time) can take as few as 1 or as many as 10 minutes (depending on primary species and intensity). For a ~60-step profile such as shown in Figure 13, this would translate into a total analysis time of ~10 hours or more, depending on how long the analyst sets the actual data collection portion within each crater.

**Linearity of secondary ion signal with concentration.** Yields of ions are generally linear (i.e., ion intensity increases with element abundance) in constant matrices (where the species of interest represents a dilute component) making measurement of concentration profiles relatively straightforward in many applications of SIMS in diffusion studies. However, there are examples where this is not true. For example, major elements (Steele et al. 1981), hydrogen in high-H glasses (Hauri et al. 2002; Tenner et al. 2009), and Li isotope ratios in olivine (Bell et al. 2009) can show non-linear effects. These are typically related to matrix effects (i.e., major element variations influencing the ionization probability of other elements, which

can also be related to changes in the way the primary beam interacts with the sample). This problem can be avoided if experiments are designed to examine diffusion of multiple elements at trace concentrations.

**Interfering molecular ions.** As indicated in Figure 11, the sputtered flux includes molecular as well as elemental ions, and some molecular ions may have the same mass/charge ratio as the diffusing species. For many potential diffusion experiments, this might not pose a problem. For example, if one wanted to measure the isotope diffusion of  $^{40}\text{Ca}$  vs.  $^{44}\text{Ca}$  across two otherwise identical basaltic glass samples, the most important interferences on the calcium isotopes would be  $^{24}\text{Mg}^{16}\text{O}$  and  $^{28}\text{Si}^{16}\text{O}$ , at the same nominal mass/charge ratios, respectively. If the Si and Mg contents were constant across the diffusion couple, these molecular species would add a constant amount to the ion signals for both calcium isotopes throughout the profile, allowing accurate diffusion coefficients to be derived in spite of the background signal. In contrast, if the Mg or Si concentration were also changing across the sample, it would be critical to eliminate these molecular ions from the mass spectrum before interpreting the SIMS analyses in the context of calcium diffusion.

The analyst has two choices for separating molecular ions from the elemental ion signal: 1) high mass resolution or 2) energy filtering. The former solution takes advantage of the fact that there is a difference in mass between an isotope of interest and a molecular ion at the same nominal mass/charge ratio. In the case of  $^{40}\text{Ca}^+$  (mass 39.962 u) vs.  $^{24}\text{Mg}^{16}\text{O}^+$  (mass 39.979 u), the mass difference is 0.017 u (the exact masses of the isotopes, based on defining  $^{12}\text{C} = 12.000$ , can be found in charts of the nuclides, textbooks, and web sites). Magnetic-sector secondary ion mass spectrometers allow the operator to close the entrance slits to the mass spectrometer to resolve these two ion signals at a nominal mass/charge ratio of 40. The mass resolution required is calculated as  $M/\Delta M$ ; in the case of the present example,  $40/0.017$  yields a mass resolving power requirement of  $\sim 2300$ . Operating the SIMS at high mass resolving powers unambiguously eliminates the molecular ion, but operation at these conditions also decreases signal intensity and decreases the width of the peak of interest, placing high demands on the stability of the secondary magnet. Planning any diffusion experiment that will utilize SIMS for characterization requires the experimentalist to carefully consider the potential molecular ion interferences and how to separate these ions from the species of interest.

In some cases, energy filtering of the secondary ion beam (Schauer and Williams 1990; Shimizu et al. 1978) will reduce molecular ion intensities to negligible levels while still leaving sufficient signal from the elemental ion to allow high-quality analyses to be obtained. This approach selects only those secondary ions that are sputtered from the sample with energies higher than can be accounted for by the potential placed on the sample. That is, some ions are ejected via the energetic collisions (initiated by primary ion impact) and have energies tens to hundreds of eV higher than the ions that are accelerated only by the potential placed on the sample. An example of an energy spectrum is shown in Figure 15. Energy filtering is generally effective at removing molecular ions composed of 3 or more atoms (e.g.,  $^{28}\text{Si}_2^{16}\text{O}_2^+$  on  $^{88}\text{Sr}^+$ ) but does not eliminate all molecular ions from the mass spectrum. Most molecules composed of two atoms are not removed by energy filtering, such as the  $^{28}\text{Si}_2$  molecule in Figure 15 (which would overlap with  $^{56}\text{Fe}$ ),  $^{24}\text{Mg}^{16}\text{O}$  and  $^{28}\text{Si}^{16}\text{O}$  interfering with Ca isotopes, and the light rare earth element oxide ions which interfere with mid- to heavy rare earth elemental ions (Zinner and Crozaz 1986). However, if *very* high-energy secondary ions are examined (Eiler et al. 1997; Hervig et al. 1989, 1992; Leshner et al. 1996; Schauer and Williams 1990) even these molecular ions can be removed, but at great expense to the signal of the elemental ion. Regardless, care must be taken to ensure that there is an appropriate approach for elimination of these molecular ions when designing diffusion experiments meant for SIMS characterization.

The examples shown for characterizing diffusion using SIMS line scans are only for silicate melts. As a general rule, diffusivities of elements in crystalline materials are orders of magnitude

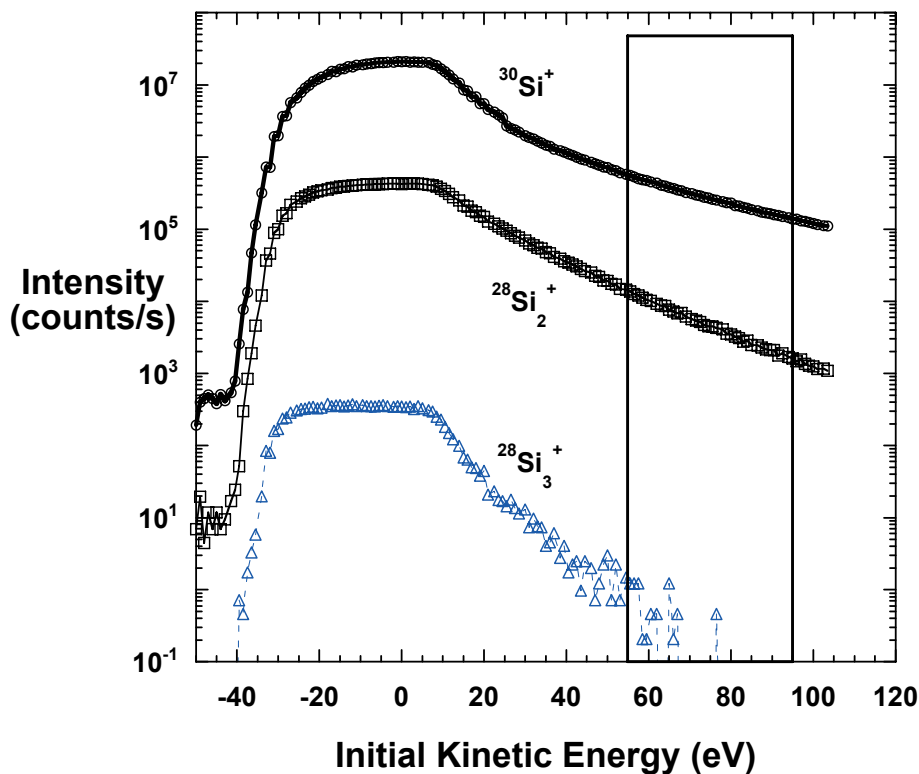


**Figure 15.** Secondary ion energy spectra showing the variation in intensity of elemental  $^{30}\text{Si}^+$  ions compared to  $^{28}\text{Si}_2^+$  and  $^{28}\text{Si}_3^+$  ions as a function of their initial kinetic energy. In this case, +10000 V was applied to a sample of quartz, and ions with a range of ~40 eV were allowed into the mass spectrometer (the energy range is a variable selected by the operator). The sample voltage was varied from 1050 V (far left side of the figure) to ~9900 V (right side). Ions with positive initial kinetic energy represent those ions ejected with high relative energies from energetic collisions in the near-surface of the sample. The signal for the elemental ion decreases with initial kinetic energy, but remains relatively intense. The complex molecular ion,  $^{28}\text{Si}_3^+$  shows a decrease in intensity by >100 $\times$  when high-energy ions are selected. In this case, these collisions also cause the molecular ion to break apart. Note that molecular ions composed of only two atoms, such as the dimer  $^{28}\text{Si}_2^+$ , are not efficiently removed by this approach. Energy filtering cannot completely remove multiply-charged species, but becomes more effective as the number of atoms in the molecular ion increases. The box on the figure represents the range of energies selected for typical analyses using energy filtering. The zero point on the figure was defined by the center of mass of the  $^{30}\text{Si}^+$  energy spectrum.

smaller than in melts, and so the scale of diffusion is not likely to be significantly larger than the diameter of the primary beam. In this case, it may be necessary to abandon line scans in favor of depth profiling analyses. Note, however, that one SIMS (NanoSIMS manufactured by Cameca) provides sub-micrometer primary beam diameters, and this instrument may be suitable for the characterization of short diffusion profiles in line scan mode.

### Depth profile analyses

Depth profile analyses take advantage of the fact that SIMS samples atoms derived from the surface of the target. As the analysis progresses, atoms from deeper and deeper in the sample are collected, providing a measure of changing chemistry with depth. The typical analysis involves focusing a primary beam of ions to a point, where those primary beams may be  $\text{Cs}^+$ ,  $\text{O}^+$ ,  $\text{O}^-$ ,  $\text{O}_2^+$ , or  $\text{O}_2^-$ . Alternative beams are more rarely employed (Hervig et al. 1989, 2004; Hervig and Williams 1986). The primary beam is swept, or rastered, over the sample surface, generally in a square pattern from ~100 to 250  $\mu\text{m}$  on a side, although the primary beam can also be shaped by an aperture to make a nearly cylindrical crater without rastering, as shown in Figure 16 (Clement and Compston 1990; Genereau et al. 2007). The process of

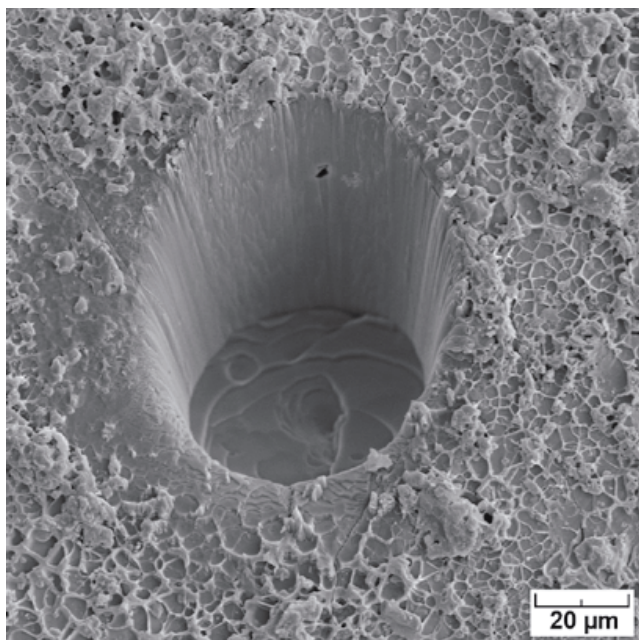


**Figure 16.** Sputtered crater in surface of volcanic plagioclase 40  $\mu\text{m}$  deep by 70  $\mu\text{m}$  in diameter obtained on the 3f SIMS in  $\sim 6$  hours using “aperture illumination,” the  $\text{O}_2^+$  primary beam, and the normal-incidence electron gun for charge neutralization (analysis and image by Dr. Kimberly Genareau, ASU). Note volcanic glass adhering to crystal surface, and the steps in the bottom of the crater. The overlap between these steps and the region of the crater floor allowed into the mass spectrometer will define the depth resolution of this profile.

sputtering the sample erodes the surface at a rate depending on the sputter yield  $S$  (defined above) together with the area of the crater and the primary current used. To make certain that the data from these depth profiles can be used for the accurate characterization of diffusion, several requirements must be fulfilled: the floor of the crater must be flat, the crater depth must be measured to calibrate the rate of erosion, any ions originating from the walls of the crater must be eliminated, the properties of the secondary ion beam should be tailored to the problem, and the effects of sputtering on the diffusion profile itself must be considered.

**Crater depth measurement.** After the analysis, the total crater depth can be measured using stylus profilometry or interferometry. An example of stylus profilometry on a sputtered crater produced by a rastered primary ion beam is shown in Figure 17. The profile shows that the crater floor is flat (unlike the SEM image of the crater in Fig. 16) with a depth of 2  $\mu\text{m}$ . It is difficult to

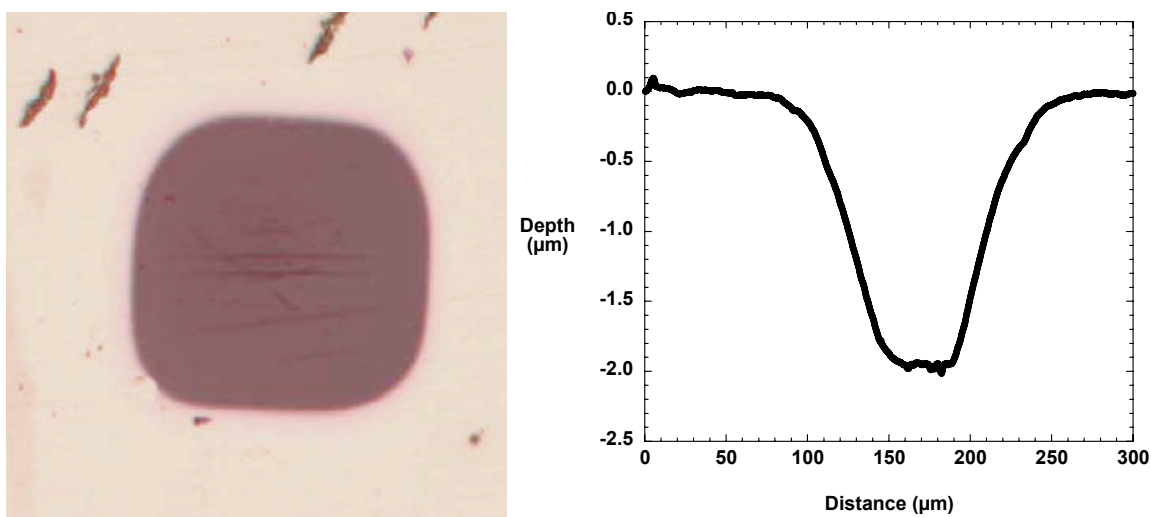


**Figure 17.** Reflected light image of a sputtered crater in Lake County plagioclase ( $\sim 100 \times 100 \mu\text{m}^2$ ) and profilometry scan showing the  $\sim 2 \mu\text{m}$  depth of the crater after the depth profile (redrawn from Genareau et al. 2007).

measure the crater depth *during* the analysis (although the Cameca Wf SIMS instrument offers an option for *in situ* crater depth measurements using laser interferometry). The analyst must assume that the erosion rate is constant over the duration of the analysis, which is not a bad assumption when the crater is several hundred nm deep, the sample is uniform in major element chemistry, and the primary beam is stable. In fact, since many geological samples are insulators, it is necessary to coat the sample surface with a thin film of carbon or gold, and the sputtering rate of these films is much different than typical silicates (Au shows a high sputter yield, while carbon has a low sputter yield). Because the Au or C coats are ~20-40 nm thick and the total crater depth is several hundred nm, the error in the sputtering rate (e.g., nm/second) is small (in addition, a gold coat can be easily removed prior to measurement of the crater depth; e.g., Van Orman et al. 2001). However, if the major element chemistry of the sample varies (for example, if diffusion of major elements occurs in the profile), the assumption of linear erosion rates must be tested (at the minimum, by determining the sputter yield on a range of homogeneous targets with appropriately varying major element chemistry).

**Contribution from crater walls.** During a depth profile, the sides (as well as the bottom) of a crater are sputtered by primary ions and so secondary ions also originate from the walls (which represent all depths in the crater). It is important to allow only those ions derived from the flat-bottomed floor of the crater into the mass spectrometer over the analysis time (= depth). The Cameca design uses stigmatic ion optics to form an image of the sample surface beyond the entrance slits of the mass spectrometer. By placing a variably-sized “field” aperture at this plane, ions from the edges of the crater floor and the crater walls can be eliminated. For those SIMS instruments that are not ion microscopes, electronic gating of the secondary ion detector can be used to eliminate ions sputtered when the primary beam is near the crater walls (note that electronic gating is not appropriate for craters formed by aperture illumination; Fig. 16). A test of whether the selected analysis condition permits crater walls to contribute a signal can be performed by sputtering an ion-implanted sample (Williams 1983). Such samples have approximately Gaussian distributions of the implanted species with depth. The baseline signal should be approximately a factor of  $10^4$  below the peak intensity (this ratio is known as the “dynamic range”). Higher background intensity for the Cameca instruments most likely suggests either an instrumental “memory” of the isotope of interest, but could also indicate that there is a contribution from the crater walls (see Fig. 18 for an example of a good depth profile through an ion-implanted silicon wafer). The above “memory effect” is a consequence of the design of the high-transmission Cameca SIMS. If a sample rich in a particular element is analyzed, some sputtered atoms of the element may be deposited on the electrically grounded plate in front of the sample (see Fig. 11). Later analyses of other samples exploring the diffusion of

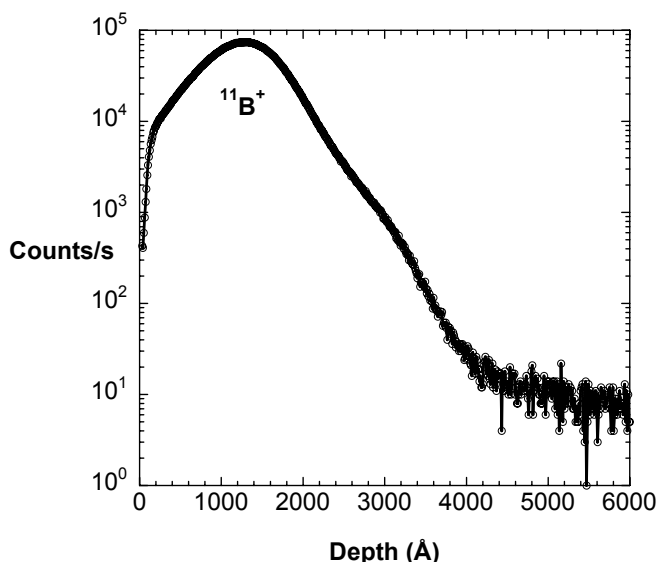


**Figure 18.** Depth profile into silicon wafer implanted with  $10^{14}$  atoms B/cm<sup>2</sup> ( $O_2^+$  primary beam, positive secondary ions detected). The background signal at ~6000 Å depth corresponds to ~0.1 ppm B. This low signal indicates that the depth profile was conducted in a manner limiting or excluding the contribution of boron from memory effects or the walls of the sputtered crater (Hervig 1996).

this same element may result in these deposits being “sputter-cleaned” from the plate and potentially landing on the floor of the crater in the new sample. Subsequent primary impacts may sputter these atoms as ions, showing up as a background signal derived from a previous sample. In addition, background signal may also be encountered if molecular ions at the same mass/charge are present. The latter topic was covered above under “Interfering molecular ions”.

**Selection of secondary species.** The yields of positive or negative ions during sputtering scales exponentially with the ionization potential or electron affinity of the element (Williams 1983). As such, the sensitivity of SIMS varies over a wide range (Hervig et al. 2006) and the analyst can select the polarity to maximize the signal for the study of trace element diffusion. Yields of secondary ions can be strongly influenced by variations in the bulk composition of the solid; such “matrix effects” were briefly described above. A typical diffusion experiment should not be strongly influenced by matrix effects, as the diffusing species is ideally contained within an unchanging matrix. However, it is common to apply a thin layer very rich in this species to the surface of a phase, and this represents a different composition than the phase of interest. Thus the secondary ion signals may fluctuate dramatically during the beginning of sputtering. These transient variations can make locating the position of the original sample surface in SIMS depth profiles difficult. This is discussed in more detail later in this volume by Ganguly (2010).

For some studies, it may not be necessary to maximize the sensitivity for a particular diffusing species if interfering molecular ions are minimal and the gradient is large. In such cases, the analyst may consider conducting the profile using simple, reproducible conditions instead of maximizing sensitivity (for example, operating at the conditions for highest sensitivity may lead to difficulties in controlling sample charging during the depth profile, as discussed below).

**Effect of sputtering.** When considering the effect of the sputtering process on a diffusion profile, there are two important items to consider. One is that the ions sputtered from the sample are dominantly derived from the top two monolayers of the sample surface (Dumke et al. 1983). The initial impression one gets from this observation is that SIMS profiles should have resolution on a similar scale. However, the other item of note is that energetic primary ions will penetrate beneath the surface and thus cause a collision cascade (multiple collisions of the atoms in the sample). The primary beam is added to the initial chemistry of the surface with the result being a more-or-less uniformly mixed chemistry over a depth corresponding to the projected range of the primary ions (Nastasi and Mayer 1994), where the projected range represents the most common depth achieved by primary ions in a sputtered sample (highest concentration of the implanted primary species). The range is a function of the impact energy and mass of the primary beam and the mass of the target. The range shows large variations; consider the two situations shown in Figure 11. In the first case, a primary beam of  $^{16}\text{O}^-$ , accelerated to  $-12.5\text{keV}$  in the duoplasmatron primary ion source, is attracted toward the sample at  $+4.5\text{keV}$  and has a total impact energy of  $17\text{keV}$ . In contrast, Figure 11b portrays a beam of  $\text{O}_2^+$ , initially accelerated to  $+12.5\text{keV}$  in the duoplasmatron but which is decelerated as it approaches the sample, striking with a total energy of  $8\text{keV}$ . In addition, the molecular beam will break into two separate oxygen projectiles upon impact, each having  $4\text{keV}$  energy. The decrease in impact energy translates into a much lower projected range (average depth of penetration) for  $\text{O}_2^+$  compared to  $\text{O}^-$ . Note that the angle of impact is different (Fig. 11), so the normal component of the impact energy is smaller for the positive primary species. The result is two-fold: the range for an  $\text{O}^-$  impact is deeper, so that the sample atoms get mixed to a greater depth than when using  $\text{O}_2^+$ , and, because the energy of the molecular  $\text{O}_2^+$  beam is restricted to near-surface interactions (and only atoms from the top two atomic layers are sputtered), more atoms are ejected per primary ion impact (higher sputter yield). The conditions presented in Figure 11b result in a sputter yield for Si metal  $\sim 4\times$  greater than in Figure 11a (Sobers et al. 2004). The implications of these changes in the instrument parameters on ion beam mixing and depth resolution are shown in Figure 19. Other modifications to the parameters are possible:

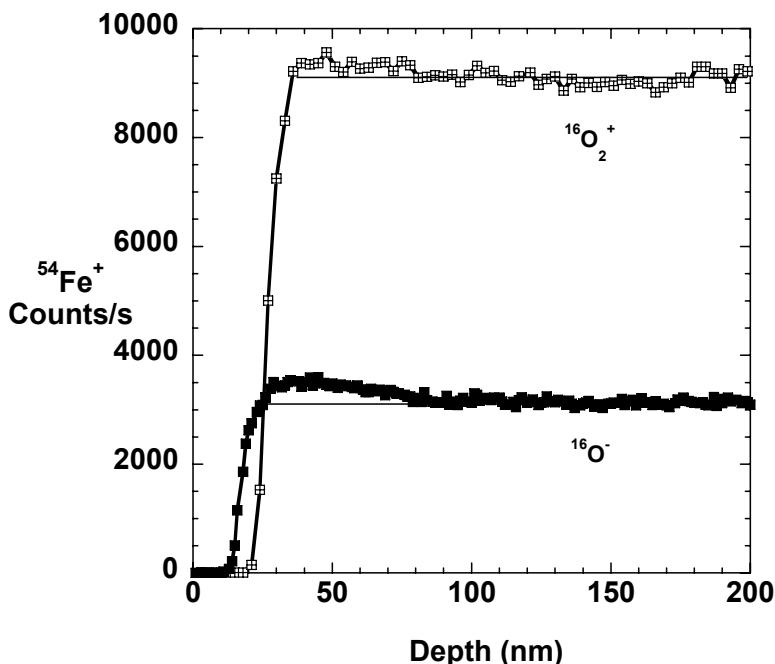


**Figure 19.** Depth profile into San Carlos olivine comparing the intensity of iron ions using  $O^-$  and  $O_2^+$  primary beams. Only the first 200 nm of the profiles are shown. The initial 20–40 nm represent sputtering through the overlying gold coat. The secondary ion signal for iron appears earlier in the profile when  $O^-$  is used because this primary species penetrates deeper into the sample and, through ion beam mixing, churns iron (and other elements in the olivine) to the surface where they can be sputtered and detected. In comparison, the smaller projected range of  $O_2^+$  mixes atoms at a shallower level, improving the depth resolution of the profile as revealed by the  $^{54}Fe$  signal appearing at a greater depth. The spacing between data points is  $\sim 3\times$  greater when  $O_2^+$  is used because the sputter yield of the molecular primary beam is  $\sim 3\times$  larger than for  $O^-$  on this phase. Note the larger transient peak for iron between 30–40 nm when  $O^-$  is used. Varying initial signals for matrix (and diffusing) elements is a common observation in depth profiles of silicates using an  $O^-$  primary species (Ganguly et al. 1998; Van Orman et al. 2001; Ito and Ganguly 2006). Using the  $O_2^+$  beam requires an auxiliary electron gun for charge neutralization (Genareau et al. 2007) and adds significant complexity to the depth profiling analysis. It also delivers the best depth resolution. However, most diffusion experiments can be designed so that the most important part of the profile is observed below the transient sputtering region, allowing straightforward use of the  $O^-$  species.

the primary beam potential can be decreased from 12.5 kV, and in some SIMS instruments, the sample potential can also be decreased to help control the impact energy (and hence the penetration depth of the primary beam) and maximize the depth resolution. Regardless of the variations in instrumental set-up, most diffusion experiments can be engineered to make the diffusion profile long compared to the short-range artifacts of sputtering.

**Sample charging.** A significant number of geologic phases are bulk insulators, and so addressing the problem of sample charging is very important. If the degree of charging varies throughout the depth profile, the secondary ion signals will vary, and different elements may be affected differently. Charge compensation is most simply addressed when a primary beam of  $^{16}O^-$  is used with the detection of positive secondary ions. In this case, accumulation of negative charge in the crater is accommodated because of the abundant secondary electrons produced during sputtering. These electrons can “hop” to the conducting gold or carbon coat surrounding the crater to drain excess negative charge. If it is necessary to use a positive primary beam, the analyst will need to use an auxiliary electron gun to alleviate positive charge build-up in the crater. This increases the complexity of the analysis, but useful depth profiles can be obtained (Genareau et al. 2009).

## **Ion implantation and SIMS**

As discussed in this volume's chapter on experimental methods by Watson and Dohmen (2010), ion implantation represents one possible experimental approach to introducing diffusants into materials for the determination of diffusion coefficients. Figure 18 shows an example of how SIMS can be used to characterize the distribution of boron in a silicon wafer after implantation. If this sample is heated, the boron will diffuse, and subsequent SIMS depth profiles in aliquots of the implanted wafer treated for different times and temperatures could be used to quantify the diffusion. While ion implantation has been coupled with analyses of profiles by RBS, NRA and ERD for diffusion studies in minerals (e.g., Cherniak et al. 1991, 2009; Ouchani et al. 1998), this type of characterization (i.e., ion implantation with SIMS analyses) has mostly been limited to the semiconductor industry, where it is important to activate the electrical properties of dopants by annealing and to know how these trace elements (e.g., Be, B, and S) have migrated during the annealing step (e.g., Tsai et al. 1979; Oberstar et al. 1982; Wilson 1984). These studies demonstrate that in general, the damage to the crystal lattice from the implantation step results in more rapid diffusion of the implanted species to the surface than into the bulk. In the case of geological samples, if the depth of the implant can be made deep enough to avoid transient effects observed during the first few nm of sputtering, and damage to crystal lattices (in the case of diffusion in minerals) can be annealed faster than the implanted species can diffuse, SIMS could be used to characterize subsequent diffusion.

### **Summary comments**

Secondary ion mass spectrometry has been an effective analytical tool for characterizing diffusion profiles. Active dialog between experimenter and SIMS laboratory is essential for designing experiments to make best use of the unique capabilities of this tool.

## **LASER ABLATION ICP-MS (LA ICP-MS)**

Laser ablation ICP-MS (LA ICP-MS) is a microanalytical technique for the determination of trace elements in solid materials. The sample to be analyzed is placed in a sample chamber with a lid transparent to UV light, and a pulsed laser beam is used to ablate a small quantity of sample material. The fine particles produced in the ablation are transported into the Ar plasma of an inductively coupled plasma mass spectrometer (ICP-MS) instrument by a stream of carrier gas (typically Ar and/or He), where they are ionized and then mass-analyzed. In the ablation process, the laser beam leaves behind an ablation crater (typically on the order of a few to tens of  $\mu\text{m}$  in diameter) where the analyzed material has been removed. Additional information on ICP-MS instrumentation and application can be found in numerous references (e.g, Montasser 1998; Taylor 2000; Sylvester 2001, 2008; Nelms 2005; Thomas 2008).

Lasers were first used with ICP-MS instruments in the 1980s. The initial ablation systems used solid-state ruby lasers (operating at 694 nm, in the infrared region), but these were found to be unsuccessful for applications in trace-element analysis due to poor laser stability, large beam diameters, and low power density, among other factors. Over the next decade, commercial laser ablation systems were developed employing Nd-YAG lasers, which produce IR laser light with a fundamental wavelength of 1064 nm. However, these faced continued limitations because IR laser light does not interact very efficiently with most solids, so further developments in the field explored the use of UV laser light (which couples more efficiently with most materials) for ablation systems given its greater potential for effective use in trace-element analysis. The interaction between UV laser light and most solids tends to involve mostly mechanical break-up of the ablated area, whereas IR laser light may produce a greater degree of sample heating and melting, which can contribute significantly to elemental fractionation and limit capabilities for analysis. More recently, some laboratories have begun to use gas-filled (excimer) lasers operating in the UV region of the electromagnetic spectrum. These lasers, including XeCl (308

nm), KrF (238 nm), and ArF (193 nm) exhibit better absorption capabilities for UV-transparent materials (e.g. silicates, calcite, fluorite), and possibly less elemental fractionation in ICP-MS than longer wavelength lasers because particles produced in ablation are smaller and easier to volatilize. Since the UV range is the fundamental wavelength for the excimer lasers, there is higher energy transfer than for Nd-YAG lasers, where UV wavelengths are produced by directing laser beams through crystals to quadruple or quintuple their frequency. The less coherent nature of the excimer beam produces better optical homogenization and therefore cleaner, flatter ablation craters, a critical factor in depth profiling. Improvements in laser optics have also provided more controlled, smaller beam spots, important in step scans and depth profiling of materials, the two methods used to obtain diffusion profiles.

Laser ablation instruments require an accurate optical system of lenses, prisms and mirrors to direct and focus the laser beam onto the sample. Several parameters are typically adjusted in analyses to optimize for a particular material and the species of interest. These parameters include laser power, laser pulse repetition rate and the number of laser pulses fired in succession. In addition, there is generally a system of apertures of different diameters that can be used to vary the beam diameter and hence the diameter of the ablation crater generated. Although the size of an ablation crater can be made very small, and small size would be advantageous in step scans of diffusion profiles, the usefulness of small volumes of material for quantitative analysis is strongly dependent on the sensitivity of the ICP-MS instrument to the elements of interest, since signal intensities for small amounts of ablated material may be low. In addition, the walls of ablation pits may yield ionic concentrations that differ from the center region because energy interactions are slightly different at the edge of the ablation spot. Further, the physical barrier of the pit edge becomes increasingly significant as ablation proceeds deeper into a sample. Because smaller spot sizes have a larger wall-to-center ratio, a greater fraction of the signal in small spot sizes will be due to contributions from the walls than would be the case for larger spots. In depth profiling of diffusion samples, apertures and rastering may be used to vary the size of the ablated area, with a larger areas removed near the sample surface (typically containing the highest concentration of diffusant) and smaller ablated areas at depth. This helps to avoid contamination at depth in the sample from the ablated material in the upper layers of the sample and from the sides of the ablation crater.

Sample chambers for laser ICPMS are typically mounted on a stage that allows the sample to be positioned relative to the laser beam in *x-y-z* coordinates and move to a particular region of interest or to perform step or area scans. In diffusion measurements, concentration profiles can be measured either through depth profiling or step scans in the direction normal to the interface between the sample and diffusant source. It should be noted that step scans are only practical for relatively fast diffusivities (down to  $\sim 1 \times 10^{-16}$  m<sup>2</sup>/sec) given typical sizes of the ablated area, so they are most useful in studies of diffusion in glasses or melts, or for some fast-diffusing species in crystalline materials. In depth profiling, since depth resolutions may range from several tenths to several  $\mu\text{m}$ , diffusion profiles will generally need to be on order of several to tens of micrometers in length, thus limiting accessible diffusivities to  $\sim 1 \times 10^{-18}$  m<sup>2</sup>/sec. Hence LA-ICPMS measurements using current instrumentation cannot access the very slow diffusivities that may be measurable by depth profiling with RBS or SIMS, and because of larger spot sizes cannot measure step scans on as fine a scale as EMPA or nanoSIMS.

In most instances, sample preparation for LA-ICPMS analysis is very simple. Samples used are typically in the form of epoxy mounts or petrographic thin sections similar to those used in electron microprobe analysis. For diffusion studies, samples would generally need to be flat and well-polished to avoid any effects on depth resolution due to surface roughness when depth profiling, and to avoid sampling problems in step scans. While sample ablation cell (the region above the sample where the carrier gas removes the ablated material) design continues to evolve and improve, it is critical that samples be configured in such a manner that they do not create eddies or pockets that could trap or fractionate the analyte, which may

compromise the ablation cell's ability to efficiently transport ablated material to the mass analyzer so that an optimal signal can be produced.

Standards are required for analytical calibration of LA-ICPMS, with standardization in most cases using various synthetic or natural reference materials of known composition. Materials commonly employed as standards are the set of silicate glasses produced by the US National Institute of Standards and Technology (NIST) containing various trace elements in a range of concentrations, standards from the US Geological Survey, or various other natural or synthetic minerals or glasses of well-determined composition. Appropriate standards will depend on the type of materials and elements to be analyzed, with ideal calibration standards matching the composition of the bulk chemical matrix of the sample (e.g., Koenig 2008). It has been found that for many crystalline silicates and glasses that 193 nm (ArF excimer) laser systems are less matrix-dependent than 213 nm (Nd:YAG) systems, and these are less matrix-dependent than longer-wavelength laser systems. Nonetheless, all LA-ICPMS analyses require calibration, and optimal reference materials that are reasonably close in bulk chemical composition to the sample, well characterized for all species of interest, homogeneous at the required scale of analysis, and available in sufficient quantities to last more than a few analyses.

Along with this external standardization, internal standardization (using elements in the sample analyzed) is typically also required in LA-ICPMS to correct raw data for differences in the ablation characteristics among standards and samples and between different elements, as well as to correct for general instrumental drift. Different groups of elements may need to be normalized against different internal standard elements to achieve high quality analyses; this will depend largely on the relative volatility of the elements. It should be noted that the elements used as internal standards must be quantified by an alternate analytical technique (e.g., electron microprobe or SXRF) in both the sample material and the external reference materials. This adds another level of complexity to the process of standardization.

Like SIMS and solution ICPMS, LA-ICPMS is subject to various mass spectrometric interferences, including isobaric, molecular and doubly-charged ion interferences. Mass spectrometric interferences are more of a concern for light elements and most of the interferences in ICP-MS systems arise from compounds made from the torch, carrier gas, and gases in the chamber atmosphere. Of secondary concern are interfering compounds generated from the major components of the matrix. Interferences may be minimized or avoided through judicious selection of isotopic species to analyze, and optimization of instrumental operating conditions. It should also be noted that when considering mass interferences in analysis that even state-of-the-art quadrupoles used in ICPMS instruments still cannot match the mass resolution of magnetic sector machines.

LA-ICPMS detection limits vary with laser power and the volume of material analyzed. Theoretical detection limits for most elements are typically in the ppb to low ppm range. LA-ICPMS provides better trace element sensitivity than the EPMA or XRF for much of the periodic table, and analyses are generally fast, with detection of the entire periodic table (except for the noble gases, H, N, O and F) at low concentrations possible in less than a minute. Despite the generally excellent trace element sensitivity of LA-ICPMS there are still cases where interferences, poor ionization in the ICP and other problems lead to compromised sensitivity, especially with small ablation spot sizes. While instrumentation has improved significantly and rapidly, questions still remain regarding control of ablation of certain types of materials, mobilization of some species in material beyond the ablated area, and, in the case of depth profiling, the effects on measured concentrations of contamination from pre-ablated material and mixing of components from several depths.

Although LA-ICPMS is finding wide application for trace-element analysis in the geosciences (e.g., Sylvester 2001, 2008), it has not yet been used extensively in diffusion studies of geological materials. Some examples include studies of Ar diffusion in K-feldspar

(Wartho et al. 1999) using depth profiling for profiles less than 50  $\mu\text{m}$  and step scans for longer profiles, Ar diffusion in quartz (Baxter 2010, this volume) with depth profiling using Nd-YAG (213 nm) and ArF excimer (193 nm) lasers, diffusion of a suite of siderophile elements (Cu, Co, Ni, Ge, Ga, As, Ru, Pd, Pt, Ir, Au) in FeNi metal (Righter et al. 2005) measured with step scans, and diffusion of rare earth elements in olivine and chromite (Spandler et al. 2007) also measured using step-scanning. With advances in instrumentation and refinements of analytical protocols, the application of this technique to investigations of diffusion in geological materials is likely to become increasingly common.

## RUTHERFORD BACKSCATTERING SPECTROMETRY (RBS)

Rutherford Backscattering Spectrometry (RBS) is a method for determining chemical composition and elemental distributions in the outer few micrometers of a material. It is based on elastic collisions from interactions between light energetic ions (typically helium, produced in a small particle accelerator) and nuclei in a sample material.  $^4\text{He}$  in the energy range of 1 to 4 MeV is the most common beam used, but other ions, including protons, deuterons,  $^3\text{He}$ , as well as those heavier than He, are also used for backscattering in certain applications. For example, protons can achieve larger depth ranges but at the expense of mass and depth resolution, and heavy ions can achieve high mass resolution, but can probe only shallow depths in a material. General overviews of RBS can be found in Chu et al. (1978) and Leavitt and McIntyre (1995).

RBS has been used to investigate diffusion in minerals for over a quarter of a century. The earliest-reported applications include the work by Melcher et al. (1983) in measuring diffusion rates of Xe in forsteritic olivine, and the study of Sneeringer et al. (1984), in which Sr diffusion in diopside was measured and results from RBS, SIMS, and radiotracer methods compared.

RBS and Nuclear Reaction Analysis (NRA, to be discussed in the next section), have depth resolutions typically ranging from a few to several tens of nm, thus permitting the measurement of diffusion coefficients down to relatively low temperatures (e.g.,  $< 700\text{ }^\circ\text{C}$ ) applicable in a wide range of geologic settings, and diffusivities down to  $\sim 10^{-23}\text{ m}^2\text{sec}^{-1}$ , avoiding in many cases the uncertainties of large down-temperature extrapolations. In addition, these methods are essentially “non-destructive” since there is no physical removal of material during the analysis.

### Basic principles of RBS

In RBS analysis, the energies of ions from scattering events are measured with a detector which is usually positioned at an angle of nearly  $180^\circ$  with respect to the incident beam, so it is referred to as “backscattering.” These collisions can be described by the equations of classical kinematics. The energies of the detected backscattered particles ( $E_n$ ) will depend on the masses of the target atoms, related to the incident energy ( $E_0$ ) by  $K_n E_0 = E_n$ , where  $K_n$  is the kinematic factor:

$$K_n = \left[ \frac{(M_n^2 - M_i^2 \sin^2 \theta)^{1/2} + M_i \cos \theta}{M_i + M_n} \right]^2 \quad (4)$$

Here,  $\theta$  is the laboratory angle through which the ion is scattered with respect to its incident direction, and  $M_i$  and  $M_n$  are the masses of the incident particle and the target atom from which it is scattered, respectively. It can be clearly seen that backscattered particle energies will be higher for heavier target atoms by simplifying the expression in taking the limiting case of  $\theta = 180^\circ$ :

$$K_n = \left[ \frac{M_n - M_i}{M_n + M_i} \right]^2 \quad (5)$$

The probabilities of occurrence of scattering events, or Rutherford scattering cross-sections, can also be determined from first principles. The scattering cross-sections are functions of target and incident particle mass and charge, as well as the scattering angle and the incident particle energy at the time of scattering. The differential scattering cross-section, or cross-section per unit solid angle  $\Omega$ , is described by the following:

$$\frac{d\sigma}{d\Omega} = \left( \frac{Z_i Z_n e^2}{4E} \right)^2 \times \frac{4 \left[ (M_n^2 - M_i^2 \sin^2 \theta)^{1/2} + M_n \cos \theta \right]^2}{M_n \sin^4 \theta (M_n^2 - M_i^2 \sin^2 \theta)^{1/2}} \quad (6)$$

Rutherford scattering cross-sections are larger for higher-Z elements (the cross-section varies as  $Z^2$ ), so the technique is more sensitive for high-Z (and larger mass) species. Detection limits can be down to a few tens of (atomic) ppm, but are considerably poorer for light elements. Since scattering cross-sections can be readily quantified and directly relate atomic concentrations to scattered particle yields, it is possible with RBS to perform quantitative elemental analysis without reference to standards.

Only a fraction of the ions comprising the ion beam incident on the sample will be backscattered from target atoms, and detected in the solid angle subtended by the detector. The detected spectrum for a particular element will include signal from scattering at the sample surface (which will have energy  $K_n E_0$ , where  $K_n$  is the K-factor for the element  $n$ , and  $E_0$  is the energy of the incident ion [i.e., initial energy of the ion beam]), as well as signal produced by scattering events with this element from greater depth in the material. Those ions not scattered from the surface will lose energy traveling deeper into the sample, primarily through inelastic collisions with the electrons of the target material, at a rate dependent on the material's density and composition. These lower-energy ions can then scatter from target atoms at depth, losing additional energy as they make their way out of the sample to the detector. If the backscattered particle energies are measured, and the energy loss rates are known or can be determined, information on the depth distribution of this element in the sample can be evaluated as follows:

$$\frac{\Delta E}{\Delta x} = [S] = \left[ K_n \left( \frac{dE}{dx} \right)_{in} + \left( \frac{1}{\cos \theta} \right) \left( \frac{dE}{dx} \right)_{out} \right] \quad (7)$$

where  $(dE/dx)_{in}$  and  $(dE/dx)_{out}$  represent the energy loss per unit distance in the material for the ions going into the sample (before scattering) and out of the sample (after scattering), also referred to as the stopping power, of the material. Stopping powers have been evaluated for ions in all elemental targets based on semi-empirical fitting of experimental data (Ziegler et al. 1985), with stopping powers for compound targets obtained through application of the Bragg Rule, which weights the contribution to the stopping power of each element in the target according to its mole fraction in the material. These values can be calculated for compounds for a range of ions and energies using, for example, the software SRIM-2006 (Ziegler and Biersack 2006; [www.srim.org](http://www.srim.org)).

An example RBS spectrum, from an experiment on Dy diffusion in fluorite, is shown in Figure 20. The RBS spectrum is a superposition of signals from all of the elements present in the outer several micrometers of the sample. Those elements with uniform distribution in the sample will each appear as a "step" (with a parabolic curve upward at lower energies because of the  $E^{-2}$  dependence of scattering cross-section) with their edge (at highest energy) at  $K_n E_0$ . In this spectrum, examples of these are the Ca and F steps for the fluorite matrix. The edge of the step for Ca, the higher mass species, is at higher energy (greater channel number) than the step edge for F. The step height is also smaller for F despite its higher molar abundance than Ca, due to its smaller scattering cross-section. Dy, of considerably greater mass than either of the major matrix elements, is at an even higher energy position, and the signal from this distribution

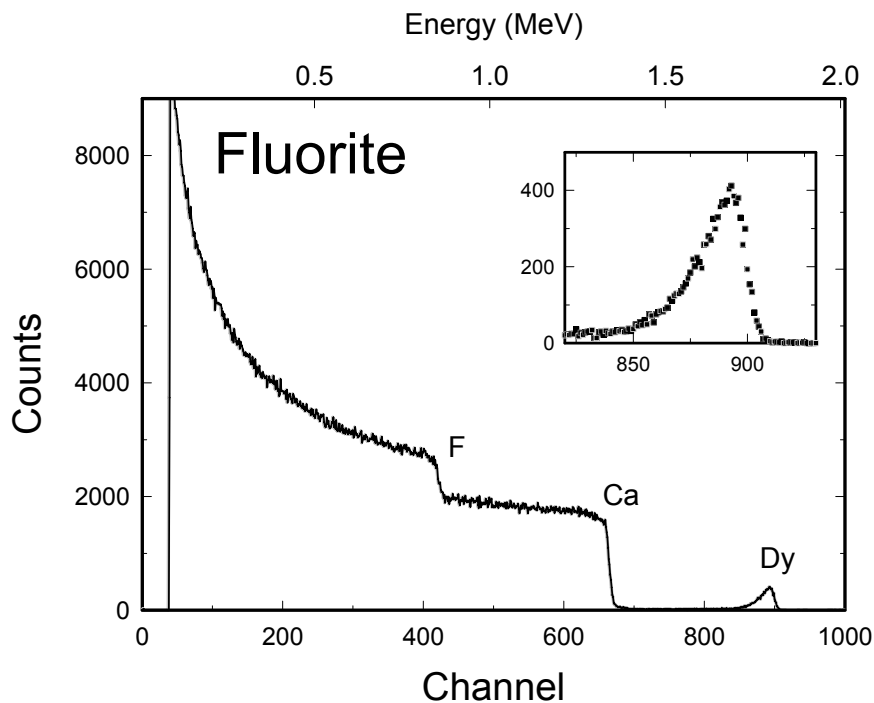


**Figure 20.** An example of an RBS spectrum taken of a sample from a diffusion experiment, in this case measuring Dy diffusion in fluorite. The “steps” toward the lower channel numbers (lower energies) represent contributions from the major elements (Ca and F). The energies of the step rises are proportional to the elemental masses, and step heights depend on Rutherford scattering cross sections, proportional to the square of the atomic number. The contribution from Dy (also shown in the inset figure) indicates a non-uniform distribution of this element, a result of it diffusing a few hundred nm into the fluorite. See text for additional details.

(which only extends a few hundred nm into the material) is well-separated from the RBS spectra constituents due to the major elements. The Dy peak maximum is about one-fifth of the near-surface height of the Ca step, but its actual concentration is much lower, as the scattering cross-section for Dy is nearly 11 times that of Ca. Elements with non-uniform distribution, like Dy in this case, will have their leading edge at  $K_n E_0$  provided there is significant concentration of the species near the sample surface, but yields will not be step-shaped. For example, a profile for a species diffusing into a material will appear as a peak with count yield decreasing with depth, extending only to the depth of penetration of the diffusing species.

In order to obtain depth distributions and elemental concentrations from RBS spectra, channel number (for the detection of particles recorded in a multichannel analyzer as in this example) is directly related to detected particle energy through calibration with major element edge positions from the sample itself or from standards analyzed in the same session. The energies in turn can be related to depth in the material (with lower detected energies of particles scattering from a given element corresponding to greater depth in the material) by using the energy loss rates in the material, as outlined above (e.g., Eqn. 7). The count yields for the element of interest can be directly related to concentrations through the scattering cross-sections for that element.

As this example illustrates, RBS is well-suited for analysis where there is a heavy impurity or species in a relatively light matrix. In contrast to some other depth profiling methods, the entire profile, including all elements present above detection limits, will be obtained in a single

analysis, so potential interferences must be considered. In diffusion studies, an ideal case would be a material composed of relatively light elements with a heavy diffusant. Diffusion profiles under best circumstances would be sufficiently short such that they would be separated from the contributions to the RBS spectrum from the major elements comprising the sample material, leaving the diffusion profile with little or no background, as is the case in the example shown in Figure 20. Although the simultaneous collection of signals from all elements may be a drawback under some circumstances, it can also be a benefit, as sample stoichiometry can be monitored, as well as changes in concentrations when multiple species are involved in chemical diffusion.

### **Depth and mass resolution**

Depth resolution of standard RBS (a few MeV energy incident helium beam, standard solid-state surface barrier detector to detect backscattered ions) in the near-surface region is about 10-20 nm. Solid-state surface barrier detectors are most common for RBS analysis given their low cost and reliability, but other types of detectors may also be used. Time-of-flight detectors, for example, may be used for backscattering when heavy ions are the incident beam, as ions heavier than Li seriously degrade solid-state surface barrier detector performance, and electrostatic analyzers have found application in various areas, including lower-energy ion scattering studies (e.g., Leavitt and McIntyre 1995). With magnetic spectrometers, electrostatic analyzers and other high-resolution detection systems (e.g., Lanford et al. 2000), near-surface resolution can be improved by about an order of magnitude over that provided by typical surface barrier detectors.

At greater depth in materials, depth resolution will degrade, primarily due to energy spread of the incident beam as it travels through the sample, referred to as “straggle.” The potential for degradation of depth resolution in this manner also has to be considered in designing experiments to be analyzed by RBS. For example, diffusion couples or “thick film” (greater than several tens of nm) sources are generally precluded because the beam either may not “see through” a thick layer to the profile beneath, or depth resolution in measurements may be seriously compromised if the beam must go through a very thick surface layer to reach the profile. In addition, samples should be well-polished (or good natural mineral growth or cleavage faces used) to avoid additional loss of resolution due to surface roughness. However, when films on sample surfaces are thin, these sources can be employed quite successfully in diffusion studies using RBS (and NRA) (e.g., Dimanov et al. 1996; Bejina and Jaoul 1996). Other studies have used powder sources (e.g., Cherniak and Watson 1992, 1994), diffusion couples where materials can be readily separated (e.g., Cherniak et al. 2007), ion implantation of diffusants (e.g., Cherniak et al. 1991; Martin et al. 1999), gas sources (e.g., Watson and Cherniak 2003), and fluid media (provided care is taken to avoid dissolution of the sample and precipitation on sample surfaces; e.g., Watson and Cherniak 1997); in short, a range of source types can be used, provided a clear, smooth sample surface or surface area can be retained for analysis following diffusion experiments.

Beam spots for standard RBS are typically in the range of 0.5-2 mm in diameter. Smaller beam spots (down to a few micrometers) can be obtained on specially designed microbeam lines with additional focusing, but usually with poorer detection limits because of much lower beam currents typical of these configurations.

Detection limits for heavy elements are good with RBS (typically to a few tens of ppm), but mass resolution becomes poorer in higher mass ranges because of the nature of the mass dependence for the kinematic factor. Therefore, there can be difficulties in separating out signals in RBS spectra from elements whose masses are in close proximity (e.g., the rare earths), and isotopes cannot be readily distinguished under most circumstances; some exceptions are described below. However, high resolution detection systems can improve mass, as well as depth, resolution. As noted above, detection limits for light elements are relatively poor in RBS,

but in some cases non-Rutherford scattering (to be discussed below) can be used to improve these detection limits, and another ion beam technique, nuclear reaction analysis (NRA), to be discussed in the next section of the chapter, may be used in some circumstances for profiling of low to medium  $Z$  atomic number elements.

Above certain energies, depending on the projectile, scattering cross-sections will depart from classical Rutherford values as a result of short-range nuclear forces. For a standard backscattering energy for  $^4\text{He}$  of 2 MeV, cross-sections for elements with  $Z$  greater than  $\sim 6$  will be Rutherford, while for 2 MeV protons this value will be  $Z \sim 20$ ; for  $^4\text{He}$  of 4 MeV energy non-Rutherford behavior will be observed for elements with  $Z$  less than  $\sim 15$ . Departure from Rutherford scattering behavior often results in large increases in scattering cross-sections; a good example is the non-Rutherford scattering cross section of  $^4\text{He}$  from  $^{16}\text{O}$  for a  $^4\text{He}$  energy just above 3 MeV (e.g., Cheng et al. 1993; Leavitt and McIntyre 1991; Demarche and Terwagne 2006) where scattering cross-sections are more than an order of magnitude greater than Rutherford values. While these enhanced cross-sections have not yet found significant direct use in diffusion studies in minerals, they have been exploited to supplement other measurements, as in the study of Cherniak (2000), where non-Rutherford  $\alpha$  scattering from  $^{28}\text{Si}$  at 6.6 MeV was used to explore substitutional processes involved in REE diffusion in fluorapatite.

### Example applications of RBS in diffusion studies

Diffusion of elements of geochronologic interest, such as Pb, can present optimal circumstances for RBS analysis, since these elements are generally of high atomic mass. Much of the focus on measuring diffusivities of atomic species of importance in geochronology has been directed toward diffusion in accessory minerals, including zircon, apatite, and monazite. Given the very slow diffusion rates of most atomic species in many accessory phases, RBS, with its superior depth resolution, has found effective application in Pb diffusion measurements (e.g., Cherniak et al. 1991, 2004a; Cherniak and Watson 2001; Gardes et al. 2006, 2007).

Since the work of Sneeringer et al. (1984) on diopside, Sr diffusion in other minerals has been investigated with RBS, including feldspars (Cherniak and Watson 1992, 1994; Cherniak 1996), apatite (Cherniak and Ryerson 1993), fluorite (Cherniak et al. 2001), and calcite (Cherniak 1997). In some of these studies, insight into substitutional processes has been obtained by monitoring changes in major constituents in RBS spectra; for example, changes in near-surface Ca in K in calcic plagioclase and K-feldspar, respectively, following Sr diffusion experiments (Cherniak and Watson 1992, 1994) suggest exchange of Sr for these species in feldspars (Fig. 21). Diffusion of a range of other minor and trace elements, including rare-earth elements (e.g., Cherniak et al. 1997a; Martin et al. 1999; Cherniak 2000), high field strength elements (e.g., Cherniak et al. 2007) and actinides (Cherniak et al. 1997b; Cherniak and Pyle 2008) have been characterized with RBS.

Measurements of diffusion of noble gases were among the earliest applications of RBS in diffusion studies in minerals, where Melcher et al. (1983) measured Xe diffusion in minerals present in meteorites (olivine, feldspar and ilmenite) in order to better understand the early chronology of the solar system. More recently, the diffusion of Ar has been measured in quartz (Watson and Cherniak 2003) as well as olivine, enstatite and corundum (Thomas et al. 2008; Watson et al. 2007) with RBS, to evaluate the potential of these major rock-forming minerals as reservoirs for noble gases within the earth. RBS measurements of Ar diffusion in quartz have also recently been coupled with measurements of Ar by laser ablation ICPMS (Baxter et al. 2006). Since these analytical methods address different length scales, their application to measurements of diffusion in the same samples can increase understanding of transport processes for noble gases in minerals. Unfortunately, because of the close energetic proximity of signals from Ar to those from K and Ca in RBS spectra, measuring Ar diffusion in minerals of interest in  $^{40}\text{Ar}/^{39}\text{Ar}$  dating (e.g., K-feldspar) with this method is problematic.

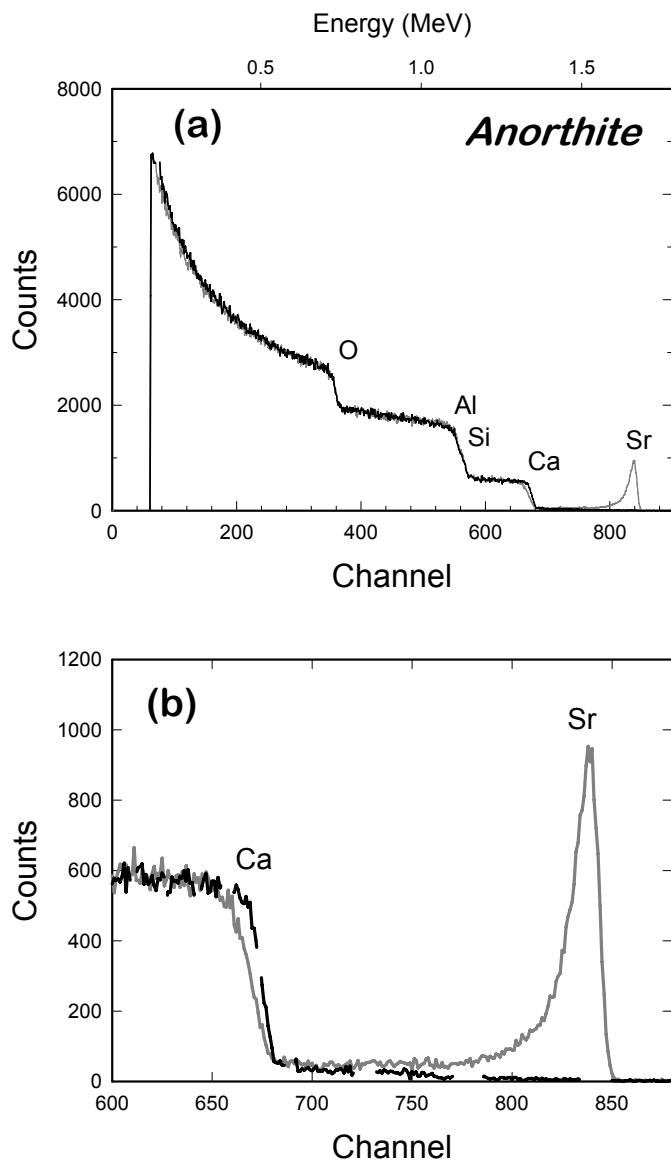


**Figure 21.** RBS spectrum of Sr diffusion in anorthite. In (a), the full spectra from a Sr diffusion experiment (grey line) and an untreated specimen of anorthite (black line) are plotted. The figure in (b) illustrates complementary Ca-Sr exchange in the process of Sr chemical diffusion, where the spectrum from the diffusion experiment shows Sr uptake accompanied by a decrease in near-surface Ca.

In certain cases, RBS can be used for measurements of major element diffusion and interdiffusion in minerals. For example, isotopic tracers can be used when there is sufficient mass separation between them and the dominant natural isotope of the element of interest (as in the case of  $^{30}\text{Si}$  or  $^{44}\text{Ca}$ ), and interdiffusion may be studied when one of the species significantly differs in mass from the other (and the heavier species is introduced through a thin film or removable source), as in the case of Fe-Mg interdiffusion. Ca self-diffusion has been measured by RBS in natural and synthetic diopside (Dimanov and Ingrin 1995; Dimanov et al. 1996; Dimanov and Jaoul 1998) using a  $^{44}\text{Ca}$  tracer deposited in a RF-sputtered isotopically enriched thin film of diopside composition. Also in diopside, RBS has been used to measure (Fe,Mn)-Mg interdiffusion (Dimanov and Sautter 2000), while Fe-Mg interdiffusion has been measured by RBS in both orthopyroxene (ter Heege et al. 2006) and olivine (Bertran-Alvarez et al. 1992; Jaoul et al. 1995a; Dohmen et al. 2007). Silicon diffusion has been measured by RBS, using  $^{30}\text{Si}$  tracers, in a range of mineral phases, including olivine (Houlier et al. 1988, 1990), pyroxene (Bejina and Jaoul 1996), zircon (Cherniak 2008), quartz and feldspars (Bejina and Jaoul 1996; Cherniak 2003). Recently, S diffusion in pyrite and sphalerite (Watson et al. 2009) has been measured by RBS using a  $^{34}\text{S}$  tracer.

In addition to single crystal studies, RBS has also been used in investigations of diffusion in polycrystalline materials, for example in characterizing diffusion of heavy elements such as cadmium, the rare earths, and actinides with applications to environmental problems and radioactive waste storage. RBS has been used by Toulhoat et al. (1996) to measure Cd diffusion in hydroxyapatite; diffusion of colloids in granitic rocks has been studied by RBS (Alonso et al. 2007a,b) to better understand transport from waste repositories and migration of other contaminants.

Although geologic applications of RBS in diffusion studies have largely focused on diffusion in crystalline materials, RBS has also been used to investigate diffusion controlled-processes in glasses, including dynamic oxidation in Fe-bearing aluminosilicate glasses and basaltic melts (Cooper et al. 1996; Cook and Cooper 2000).

### NUCLEAR REACTION ANALYSIS (NRA)

In certain respects, NRA is similar to RBS in that a beam of ions produced in an accelerator is used to probe the chemical composition of the outer few micrometers of a material. However, for NRA, the ions are sufficiently energetic to overcome the Coulomb barrier and interact with specific target nuclei, resulting in a nuclear reaction. Products of these reactions (which may be gamma rays or light charged particles) are then detected, providing information about the depth distribution and concentrations of specific species in the material. Because this method relies on inducing nuclear reactions, it is isotope-specific. NRA has been applied in studies of diffusion in geologically significant materials over several decades. Among the earliest studies was an investigation of oxygen diffusion in quartz using the nuclear reaction  $^{18}\text{O}(p,\alpha)^{15}\text{N}$  (Choudhury et al. 1965). By the 1980s, applications of Nuclear Reaction Analysis to diffusion problems became more frequent.

Given the beam energies accessible to accelerators commonly used for these techniques (typically up to several MeV), NRA is most often exploited for the detection of light elements. Many useful nuclear reactions, especially those induced by protons, require beam energies of only a few hundred keV, so relatively low-energy accelerators can be used for some types of measurements. Instrumentation required is generally similar to that for RBS, although nuclear reaction analysis methods that rely on the measurement of gamma rays induced in the reaction require scintillation detectors rather than the charged particle detectors used for RBS, and for NRA when charged particles are the product from the nuclear reaction detected. The isotope-specificity of NRA makes it suitable for a range of applications involving a tracer species, including diffusion studies. A good example is the use of an  $^{18}\text{O}$  tracer and the nuclear reaction  $^{18}\text{O}(p,\alpha)^{15}\text{N}$  to measure oxygen diffusion in minerals. The expression in the previous sentence is the abbreviated way of writing the reaction



where a proton beam is used to induce a nuclear reaction with an  $^{18}\text{O}$  atom. The products of the reaction are a  $^{15}\text{N}$  atom and an alpha particle, with the latter species being detected.

NRA can be done in either resonant or non-resonant modes, depending on the reaction used and its cross-section. The reaction cross-section describes the probability of occurrence of a specific reaction as a function of incident particle energy and the angle between the incident particle and measured reaction product. As a function of energy, reaction cross-sections can have narrow energy-width regions of large cross-section (“resonances”), with regions of relatively small cross section in energy regions above and below these resonances; for some reactions there may also be broader-width energy regions with enhanced cross-sections (e.g., Fig. 22). For application of NRA in the resonant mode, the ideal reaction would have a large cross-section at the resonance energy  $E_r$  and negligible or comparatively small cross-section

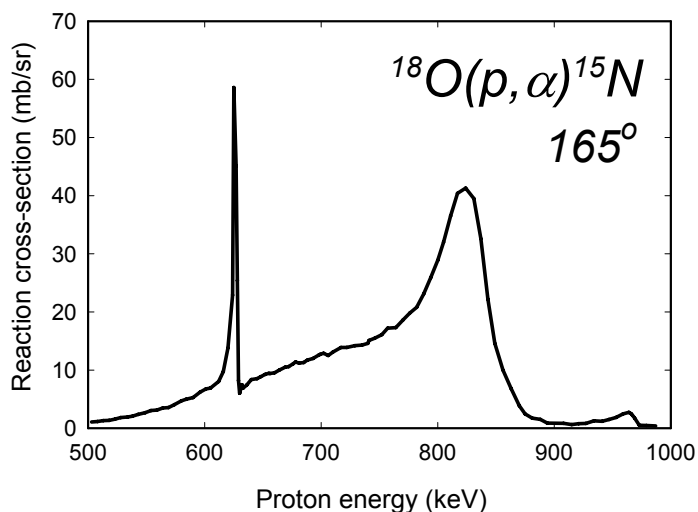


**Figure 22.** An example of a reaction cross section as a function of incident ion energy, in this case the reaction  $^{18}\text{O}(p, \alpha)^{15}\text{N}$  at a laboratory angle (angle between incident beam and detector) of  $165^\circ$ . The reaction cross-section (which describes the probability of the reaction occurring) shows a broad region of enhanced cross-section in the range of 800 keV, and a narrow energy region of enhanced cross-section (a resonance) at  $\sim 629$  keV. The cross section is plotted as millibarns (where a barn is  $10^{-24}$  cm $^2$ ) per unit of solid angle (in steradians). Cross section data are from Amsel and Samuel (1967).

at other nearby energies. Perhaps the best example is the  $^1\text{H} + ^{15}\text{N} \rightarrow ^{12}\text{C} + ^4\text{He} + \gamma$  resonant reaction (resonance energy 6.385 MeV), which is used to profile  $^1\text{H}$  (with a  $^{15}\text{N}$  beam), one of the few means to obtain quantitative depth profiles of H in materials. This method was used by Laursen and Lanford (1978) in their pioneering study on the hydration of natural obsidian, in which they explored the mechanism of hydration and developed an interdiffusion model. With an incident proton beam, this same reaction can also be employed to profile  $^{15}\text{N}$ .

The application of resonant profiling is illustrated schematically in Figure 23. When the incident beam is at the resonance energy  $E_r$ , the concentration of the species of interest at the sample surface is detected. Depth profiling is done by increasing the incident beam energy, thus increasing the depth in the material at which the resonance (and enhanced yield of the products of the nuclear reaction) occurs. Depth scales are determined by the difference between the beam energy and the resonance energy, and the rate of energy loss for the incident ions in the material. Concentrations of the element or isotopic species of interest at a particular depth are determined from the detected yields of the product of the nuclear reaction for the number of particles of the incident beam delivered to the sample, with detected yields of products of the nuclear reaction dependent on the reaction cross-section at the resonance energy, beam-detector geometry, and efficiency of the detector.

Resonant profiling is also used with a range of other nuclear reactions that have found application in diffusion studies, such as  $^{27}\text{Al}(p, \gamma)^{28}\text{Si}$  (using the 992 keV resonance, e.g., Sautter et al. 1988) to measure Al diffusion in diopside,  $^{30}\text{Si}(p, \gamma)^{31}\text{P}$  (using the 620 keV resonance, e.g., Jaoul et al. 1995b; Bějina and Jaoul 1996; Cherniak 2003, 2008) to measure Si diffusion in quartz, diopside and zircon, and  $^{48}\text{Ti}(p, \gamma)^{49}\text{V}$  (Cherniak and Watson 2007) to measure Ti diffusion in zircon.

When reaction cross-sections are sufficiently large and vary smoothly over an extended energy range, the entire depth profile may be obtained using a single incident beam energy. This is referred to as non-resonant profiling. In non-resonant mode, the depth scales are determined by energy loss rates of incident and outgoing product particles from the nuclear reaction. Non-resonant profiling can be used with many reactions in which particles (e.g., protons, deuterons,  $^3\text{He}$ ,  $\alpha$  particles), rather than  $\gamma$  rays, are the detected reaction product, since  $\gamma$  rays do not experience the energy losses particles do in passing through the sample material and thus cannot provide depth information.

The measurement of  $^{18}\text{O}$  using the nuclear reaction  $^{18}\text{O}(p, \alpha)^{15}\text{N}$  is a typical application of non-resonant profiling.  $^{18}\text{O}$  profiling is most often done in non-resonant mode at incident

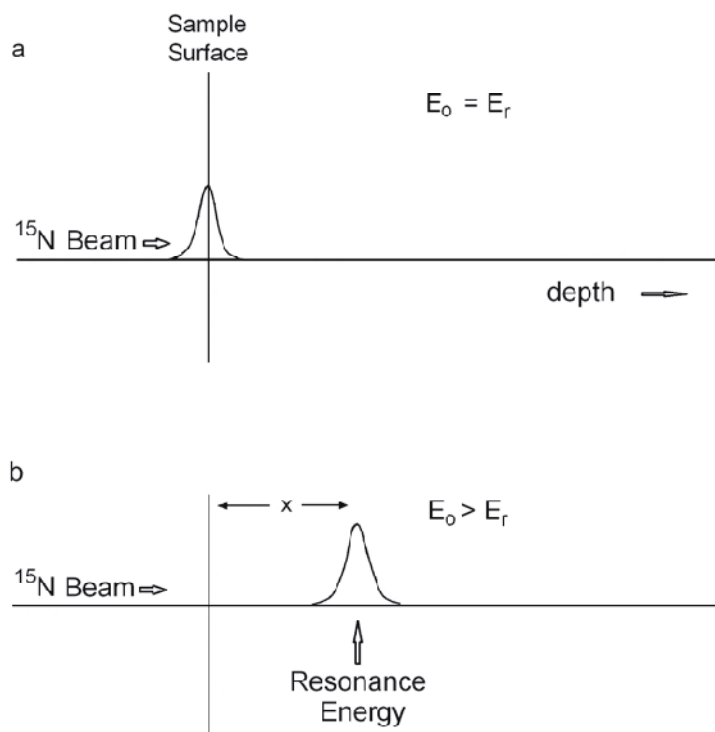


**Figure 23.** Schematic drawings illustrating the method of resonant NRA. This example shows the use of the reaction  ${}^1\text{H}({}^{15}\text{N},\alpha\gamma){}^{12}\text{C}$  to measure  ${}^1\text{H}$ . An incident  ${}^{15}\text{N}$  beam is used, and  $\gamma$  rays of characteristic energy produced in the reaction are detected. When the  ${}^{15}\text{N}$  beam is at the resonant energy ( $E_r$ ), hydrogen concentrations at the sample surface are measured. At higher incident  ${}^{15}\text{N}$  energies, H concentrations at depth in the material are sampled, with the depth ( $x$ ) determined by the difference in energy between the incident beam and the resonant energy, divided by the energy loss rate for  ${}^{15}\text{N}$  in the sample material.

energies of around 800 keV (e.g., Reddy et al. 1980; Ryerson et al. 1989), taking advantage of a region of fairly large and smoothly varying reaction cross-section (Amsel and Samuel 1967) (Fig. 22). A spectrum of  $\alpha$  particles over a range of energies is collected, representing contributions from  ${}^{18}\text{O}$  at various depths in the material (Fig. 24). This reaction has been used for oxygen diffusion studies in many mineral phases, including olivine (Reddy et al. 1980; Gérard and Jaoul 1989; Ryerson et al. 1989; Jaoul et al. 1980), zircon (Watson and Cherniak 1997), rutile (Derry et al. 1981; Moore et al. 1998), monazite (Cherniak et al. 2004b) and titanite (Zhang et al. 2006). It should be noted that  ${}^{18}\text{O}$  also can be profiled using the resonant technique, with, for example, the sharp resonance at 629 keV (Fig. 22).

In addition to resonant and non-resonant approaches described above, “hybrid” methods are sometimes used in which energies are varied, but the cross-section is sufficiently broad that the signal is comprised of integrated contributions from a significant range of depths in the material at each energy step. This approach is usually employed in cases of faster diffusing species where diffusion distances are comparatively long. Some examples are measurement of He diffusion using the  ${}^3\text{He}(\text{d,p}){}^4\text{He}$  reaction (e.g., Cherniak et al. 2009, Miro et al. 2006).

Interpretation of NRA spectra and conversion to concentration profiles is slightly more complicated than for RBS for a few reasons. In RBS, Rutherford scattering cross-sections can be described analytically; in contrast, cross-sections for nuclear reactions depend on nuclear structure and can vary quite dramatically with incident particle energy and with elemental and isotopic species. Cross-sections must be empirically determined through careful measurement as functions of incident energy and beam-detector angle. Fortunately, cross-sections for many useful reactions have been measured and tabulated for analytical purposes. Tables of reactions

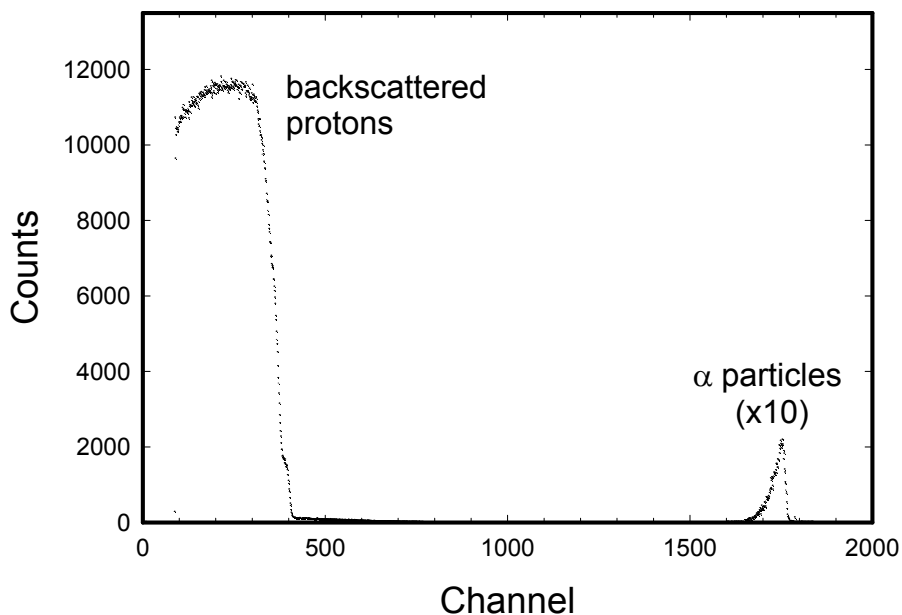


**Figure 24.** An example spectrum for non-resonant nuclear reaction analysis, in this case measuring oxygen diffusion in olivine using the  $^{18}\text{O}(\text{p},\alpha)^{15}\text{N}$  reaction. The count yields in the alpha peak (toward the right of the figure) are proportional to the  $^{18}\text{O}$  concentration in the material, with yields at lower channel numbers (and lower energies) corresponding to  $^{18}\text{O}$  at greater depths in the material. Also detected in the spectrum are protons backscattered from the constituents of the olivine; these are toward the lower channel number (lower energy) end of the spectrum. Because the energy released in the nuclear reaction is relatively large (3.98 MeV) the alpha particles produced in the reaction will be fairly energetic, with much larger energies than the backscattered protons. However, reaction cross-sections are generally much smaller than Rutherford scattering cross-sections, so the count yields of alpha particles produced in the reaction are considerably less than those of the backscattered protons. Samples from Ryerson et al. (1989).

used in NRA can be found in Cherniak and Lanford (2001) and Tesmer and Nastasi (1995); the online database IBANDL (the Ion Beam Analysis Nuclear Data Library, at <http://www-nds.iaea.org/ibandl/>) has a frequently updated compilation of reaction cross-sections as a function of energy for a range of nuclei and projectiles.

An additional complication in interpreting spectra is that the incident particles and product species from the nuclear reaction will not be the same, as they are in elastic scattering, and thus can have quite different energy loss rates in the sample material. Using the example of the  $^{18}\text{O}(\text{p},\alpha)^{15}\text{N}$  reaction, the incident protons will lose energy at a much smaller rate while traversing a given distance in the material than the alpha particles that are the product of the reaction. When gamma rays are the species measured, for example when profiling H and Al with the reactions  $^1\text{H}(\text{p},\gamma)^2\text{H}$  and  $^{27}\text{Al}(\text{p},\gamma)^{28}\text{Si}$ , respectively, depth information can only be obtained through varying the energy of the incident beam since the gammas will travel through the material without losing energy as will product particles such as protons, alphas, or deuterons.

In some cases, a multiple ion beam techniques can be employed in analysis of a single sample or set of samples to provide added information about the diffusional process. For example, RBS measurements of Pb and Sr diffusion in feldspars (Cherniak and Watson 1992, 1994; Cherniak 1995a) were supplemented by NRA measurements of Al and Na in order to provide insight into substitutional mechanisms involved in Pb and Sr exchange in alkali feldspars and sodic plagioclase. Similarly, measurements of phosphorus using the reaction  $^{31}\text{P}(\alpha,\text{p})^{34}\text{S}$  were made to accompany RBS measurements of REE diffusion profiles in zircon to investigate the role of the substitution  $\text{REE}^{+3} + \text{P}^{+5} \rightarrow \text{Zr}^{+4} + \text{Si}^{+4}$  in rare-earth element diffusion in zircon

(Cherniak et al. 1997b). In addition, in some studies of Si diffusion, both RBS and NRA (using the  $^{30}\text{Si}(p,\gamma)^{31}\text{P}$  reaction) have been employed to measure Si diffusion on the same samples, with good agreement among results (e.g., Bějina and Jaoul 1996; Cherniak 2003, 2008).

### ELASTIC RECOIL DETECTION (ERD)

ERD (Elastic Recoil Detection) is another ion-beam method for measuring depth profiles of light elements ( $Z = 1$  to  $\sim 10$ ). It is like RBS in that it relies upon elastic scattering; however, the incident ions must be heavier than the element to be profiled. Typical incident beams employed (e.g., Petit et al. 1990; Cookson 1991) are  $^4\text{He}$  at a few MeV (for profiling hydrogen) or heavier ions such as C, Si or Cl at higher energies ( $\approx 1$  MeV/amu). The light target atoms will recoil in a forward direction upon collision with the heavier incident ions; if the sample is tilted these recoiled atoms will escape the sample and can be detected. ERD can also be performed in transmission mode, where the detector is placed behind the sample and recoiled atoms exiting the back of the sample are detected, but this can only be done for thin (typically a few micrometers) self-supporting films (such as polymers), so this approach is of limited use in geological studies. The energy of the detected recoils  $E_r$  will provide information about the depth distribution of the recoiling species, as described in the expression:

$$E_r = E_0 \frac{4M_1M_2 \cos^2 \phi}{(M_1 + M_2)^2} = K_r E_0 \quad (9)$$

where  $E_r$  is the energy of the recoiled atom,  $E_0$  is the energy of the incident ion,  $M_1$  and  $M_2$  are the masses of the incident and recoiled species, respectively, and  $180^\circ - \phi$  is the angle between the incident beam and the detector used to detect the recoiled atoms. In general,  $\phi$  will be set at angles between  $10$  and  $30^\circ$ . To prevent scattered incident ions from interfering with the signal from the light recoils, an absorber foil is typically placed in front of the detector to stop these heavier ions. When the absorber foil is used, the detected particle energy is not  $E_r$ , but a lower value  $E_{det}$ , with

$$E_{det} = E_r - \delta_f S_f \quad (10)$$

where  $\delta_f$  and  $S_f$  are, respectively, the thickness of the foil, and “stopping power” or energy loss for the ions in the foil per unit thickness. As with RBS and NRA, depth scales for the detected particles are constructed from information on energy loss in the sample material. If an incident ion penetrates to a specific depth (measured normal to the sample surface) before a recoil event occurs, the incident ion will have lost energy in inelastic collisions while traveling through the material. Similarly, the recoil atom will lose energy traveling out of the sample to its surface. If the energy-averaged stopping powers for the incident and recoil species are  $S_i$  and  $S_r$ , respectively, the initial depth of the recoil species can be determined from the expression

$$\text{depth} = (E_{det} + \delta_f S_f - K_r E_0) \left( \frac{K_r S_i}{\sin \alpha} + \frac{S_r}{\sin \beta} \right)^{-1} \quad (11)$$

where  $\alpha$  and  $\beta$  are the acute angles between the sample surface and the incident beam, and the sample surface and the detector. Depth resolution will depend on the energy loss variations of both the incident and recoiling atoms in the material and the recoiling atoms in the foil, and will typically be in the range of tens of nm. Better resolution (by up to an order of magnitude) can be obtained by eliminating the stopper foil and using other detection systems, such as a magnetic spectrometer, rather than standard surface barrier detectors.

Although it holds considerable promise for analysis of light elements, thus far ERD has been used to only a limited extent in diffusion studies of geological materials. An example is

measurement of He diffusion in fluorapatite by Ouchani et al. (1998). Additional information on the technique (along with schematics of experimental configurations for ERD analysis) can be found in Barbour and Doyle (1995).

## FOURIER TRANSFORM INFRARED SPECTROSCOPY

Infrared (IR) spectroscopy uses infrared radiation to probe the chemical species and molecular clusters in solids, liquids or gases by exciting the vibrational modes (which absorb in the infrared region) in molecules or clusters. Infrared radiation is electromagnetic radiation with frequencies lower than visible light but higher than radio wave frequencies. The infrared spectrum covers the wavelength range from 0.75 to 100  $\mu\text{m}$ , longer than visible light (400-750 nm) but shorter than the radio wave. The infrared spectrum is often subdivided into the near-infrared (NIR, wavelength 0.75-3  $\mu\text{m}$ ), mid-infrared (MIR, 3-30  $\mu\text{m}$ ), and far-infrared (FIR, 30-100  $\mu\text{m}$ ) regions. Both the frequency and wavelength are related to the infrared radiation energy. The most common way to express infrared energy in plots of infrared spectra is by wavenumber, which in spectroscopy equals the number of waves per unit length (most often expressed in units of  $\text{cm}^{-1}$ , but  $\text{mm}^{-1}$  will be used here).

Infrared spectroscopy is widely applied in identification of specific chemical bonds, species and clusters. Its application in quantitative analyses (the focus of this chapter) is mostly in the measurement of  $\text{H}_2\text{O}$  and  $\text{CO}_2$  concentrations, as well as concentrations of the individual species (molecular  $\text{H}_2\text{O}$  and the hydroxyl ion for total  $\text{H}_2\text{O}$ , and molecular  $\text{CO}_2$  and the carbonate ion for total  $\text{CO}_2$ ). In the geological literature, these analytical capabilities were pioneered by Stolper (1982a,b), Aines and Rossman (1984), Fine and Stolper (1985, 1986), Newman et al. (1986), Paterson (1986), Rossman (1988), and Bell and Rossman (1992). In addition to the aforementioned species,  $\text{NH}_4^+$  concentrations in mica (Busigny et al. 2003, 2004) have also been measured by IR spectroscopy. Although the number of components that can be analyzed by infrared spectroscopy is limited,  $\text{H}_2\text{O}$  and  $\text{CO}_2$  are major volatile components in the Earth and in melts and minerals, and they cannot be analyzed easily by other methods. Furthermore, infrared spectroscopy is a non-destructive method (but preparation of doubly-polished sections for analysis will cause sample loss) with high sensitivity, high precision, and high spatial resolution. Recent development has resulted in nanoSIMS having even better sensitivity and spatial resolution than infrared spectroscopy (e.g., Saal et al. 2008), but infrared spectroscopy is still the only method available to quantitatively determine the concentrations of species, which may provide critical structural information and further insight into diffusional processes. Below we introduce the basic principles describing the molecular vibrational modes that often cause infrared absorption, the instrumentation used in infrared spectroscopy, and applications to measurement of  $\text{H}_2\text{O}$  and  $\text{CO}_2$  concentrations and their use in diffusion studies.

### Vibrational modes and infrared absorption

Basic principles of vibrational motion in multi-atom “molecules” (including ionic clusters) have been discussed in numerous texts and papers (e.g., Colthup et al. 1990; Ihinger et al. 1994; Beran and Libowitzky 2004). The vibrational motion absorbs in the infrared region. For an OH group in a structure, there is a stretching mode (Fig. 25), absorbing near  $355 \text{ mm}^{-1}$ . For an  $\text{H}_2\text{O}$  molecule ( $\text{H}_2\text{O}_m$ ), there are 3 vibrational modes (symmetric stretching at  $365 \text{ mm}^{-1}$ , asymmetric stretching at  $375 \text{ mm}^{-1}$ , and bending at  $163 \text{ mm}^{-1}$ ; Fig. 26). For a  $\text{CO}_2$  molecule, because it is a linear molecule, there are 4 vibrational modes (symmetric stretching at  $139 \text{ mm}^{-1}$  that is IR inactive, asymmetric stretching at  $235 \text{ mm}^{-1}$ , and two identical bending modes at  $67 \text{ mm}^{-1}$ ; Fig. 27). For a carbonate ion ( $\text{CO}_3^{2-}$ , a triangular ion), there are 6 independent vibrational modes (symmetric stretching at  $106 \text{ mm}^{-1}$  that is IR inactive, two asymmetric stretching at about  $142 \text{ mm}^{-1}$  that may split into a pair of peaks, two in-plane bending modes at about  $68 \text{ mm}^{-1}$ , and one out-of-plane bending mode at  $88 \text{ mm}^{-1}$ ).



**Figure 25.** Stretching mode of an OH cluster, where the small solid circle represents H, and the large open circle represents O. The diagram only shows one direction of motion during vibration. By reversing the direction of all arrows, one gets the other type of motion in this and other examples below.

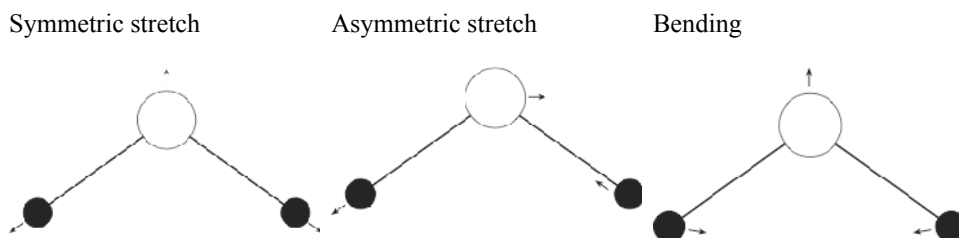


**Figure 26.** Vibrational modes of the  $\text{H}_2\text{O}$  molecule, where the small solid circles represent H, and large open circles represent O.

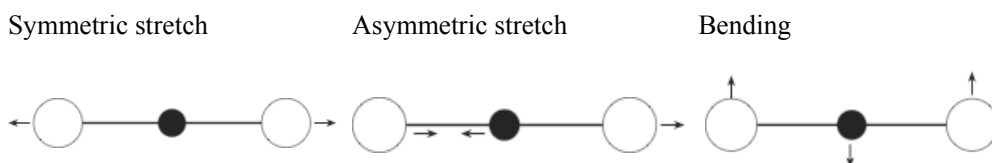


**Figure 27.** Vibrational modes of the  $\text{CO}_2$  molecule, where small solid circles represent C, and large open circles represent O.

Based on quantum mechanics, the quantized energy level of a harmonic oscillator (an approximation for a vibrational mode) can be expressed as follows (Fig. 28):

$$E = (n+1/2)hn, \text{ where } n = 0, 1, 2, \dots \quad (12)$$

where  $E$  is the quantized energy level,  $n$  is the quantum number,  $h$  is the Planck constant, and  $\nu$  is the characteristic vibrational frequency, which is related to the force constant  $k$  as:

$$\nu = \sqrt{\frac{k}{m^*}} \quad (13)$$

where  $m^*$  is the reduced mass, for a diatomic cluster defined as

$$m^* = \frac{1}{\frac{1}{m_1} + \frac{1}{m_2}} \quad (14)$$

where  $m_1$  and  $m_2$  are the masses of atom 1 and atom 2 in the diatomic cluster. Based on this definition, the reduced mass  $m^*$  is smaller than either  $m_1$  or  $m_2$ . For example, for O-H stretching,  $m_1 = 1.0079$  u, and  $m_2 = 15.9994$  u, leading to a reduced mass  $m^* = 0.9482$  u.

On the basis of Equation (12), the lowest energy (ground state) of a harmonic oscillator is  $(1/2)h\nu$  when  $n = 0$ , which is called the zero-point energy. By absorbing an energy of  $h\nu$  (corresponding to the fundamental vibrational band in an IR spectrum), the harmonic oscillator can be excited to the energy of  $1.5h\nu$  (Fig. 28). By absorbing an energy of  $2h\nu$  (corresponding to the first overtone in an IR spectrum), the harmonic oscillator can be excited to the energy of  $2.5h\nu$ , and so on. If the oscillator is perfectly harmonic, the selection rule states that overtones should not occur. Because the energy versus distance relation for a chemical bond is slightly different from that of a harmonic oscillator (Fig. 29), (1) the overtones do occur with an

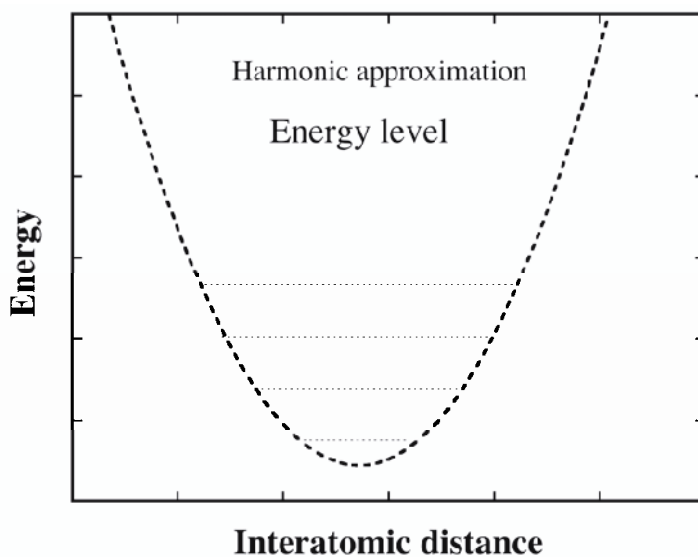


**Figure 28.** Quantized energy levels of a harmonic oscillator.

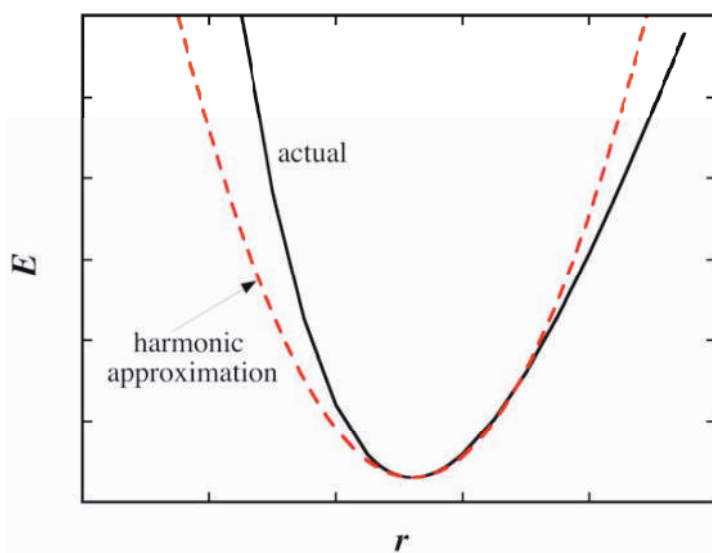


**Figure 29.** Potential energy of a diatomic molecule as a function of distance between the two atoms. The solid curve is the actual energy and the dashed curve is the harmonic approximation. The  $r$  that corresponds to the energy minimum is the bond length (or equilibrium distance  $r_e$ ).

intensity about two orders of magnitude lower than the fundamental modes, and (2) the first overtone may occur at a slightly different wavenumber from exactly 2 times the fundamental band. A photon may also simultaneously excite two modes (combination modes). The intensity of the combination modes is between those of the fundamental modes and overtones.

Not all vibrational modes can be detected by infrared spectroscopy. If a molecule has a zero dipole moment (or a center of symmetry), and if the vibrational mode is symmetric so that it does not generate a dipole moment, it would be IR-inactive, meaning that in theory it cannot be excited by infrared radiation. In practice, however, IR-inactive modes still absorb in the IR region but the absorption is very weak. For example,  $\text{H}_2$ ,  $\text{N}_2$  and  $\text{O}_2$  are all IR-inactive. On the other hand, if a molecule does not have a center of symmetry (such as the case of a CO molecule), or if the vibration is asymmetric for a molecule with center of symmetry

(such as asymmetric stretching of the O=C=O molecule), the vibrational mode is IR-active. When a vibrational mode is IR-inactive, it is Raman-active. When a vibrational mode is IR-active, its absorption in Raman is weak. Hence, IR spectroscopy and Raman spectroscopy are complementary. For example, H<sub>2</sub> is IR inactive but can be easily detected by Raman for diffusion studies (e.g., Shang et al. 2009). Furthermore, the spatial resolution of Raman spectroscopy is much better than IR spectroscopy, especially because the Raman beam can be focused to a specific spot (including a specific depth in a sample) with 1-2  $\mu\text{m}$  resolution (e.g., Di Muro et al. 2006). However, the reliability of using Raman spectroscopy for quantitative analyses has been debated due to complications in its calibration when internal calibration has been used (e.g., Thomas 2000; Arredondo and Rossman 2002). Recent attempts using external calibration (or the “comparator technique”) show promise for determining total H<sub>2</sub>O contents (Di Muro et al. 2006; Thomas et al. 2008). Even though determining total H<sub>2</sub>O contents may be possible, extracting concentrations of hydrous species (H<sub>2</sub>O<sub>m</sub> and OH) does not seem to be possible (Behrens et al. 2006). Due to its high spatial resolution and its ability to be focused at specific depths in a material, future development may potentially make Raman spectroscopy a much more powerful tool in quantitative analyses of volatile species and in diffusion studies.

Two infrared spectra are shown in Figure 30, one for a low-H<sub>2</sub>O glass in which the fundamental OH stretching band (at 355 mm<sup>-1</sup>) can be seen clearly, and one for a high-H<sub>2</sub>O glass, in which the first overtone (about 710 mm<sup>-1</sup>) of the fundamental OH stretching band, and the combination bands at 452 mm<sup>-1</sup> for X-OH (this band is characteristic of OH not associated with H<sub>2</sub>O molecules) and at 523 mm<sup>-1</sup> for H-O-H (this peak is characteristic of molecular H<sub>2</sub>O) can be observed. The fundamental stretch peak is too high (over-scale) to be shown in Figure 30b.

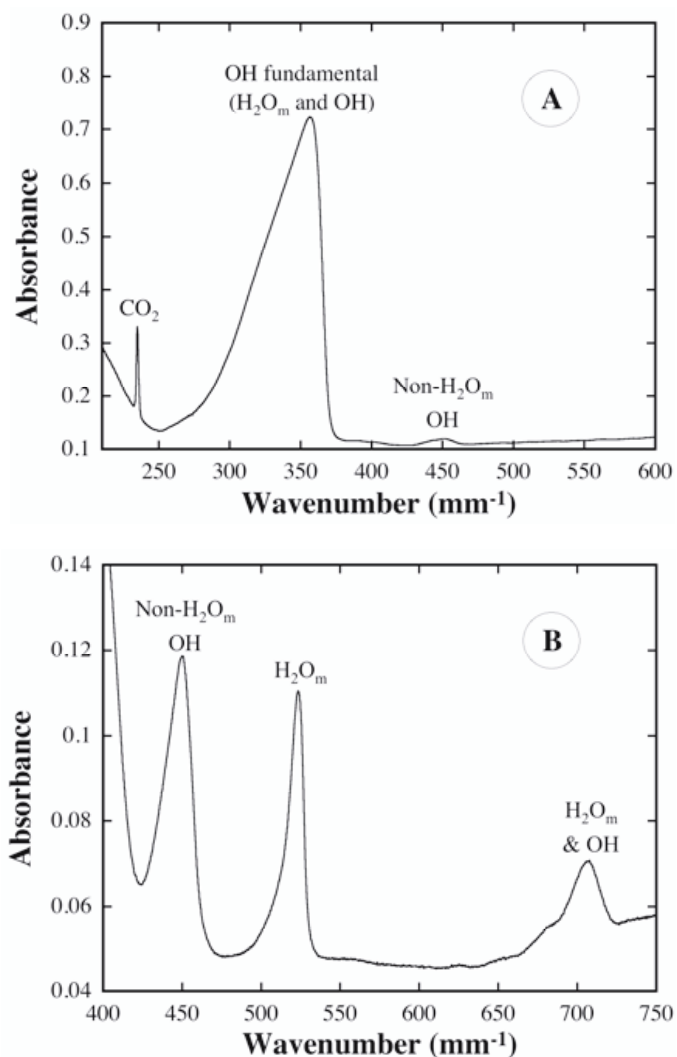


**Figure 30.** Two IR spectra, one for low H<sub>2</sub>O content and one for high H<sub>2</sub>O content. The sharp peak at 235 mm<sup>-1</sup> is the asymmetric stretching of molecular CO<sub>2</sub>; the peak at 355 mm<sup>-1</sup> is the fundamental stretching of OH (which indicates the sum of H<sub>2</sub>O<sub>m</sub> and OH because H<sub>2</sub>O<sub>m</sub> also contains OH bonds); the peak at 450 mm<sup>-1</sup> is a combination mode indicating OH, the peak at 523 mm<sup>-1</sup> is a combination mode indicating H<sub>2</sub>O<sub>m</sub>, and the peak at 710 mm<sup>-1</sup> is the first overtone of OH fundamental stretching. From Zhang and Behrens (2000) and Ni et al. (2009a).

## Instrumentation for Infrared Spectroscopy

The classical infrared spectrometer uses the wavelength dispersive method to measure infrared spectra. Even though it is no longer used, we introduce the principles of the wavelength dispersive infrared spectrometer because their explanation is straightforward. The dispersive infrared spectrometer consists of four parts: energy source, prism, sample chamber, and detector. An energy source (which depends on whether one is interested in MIR or NIR), emits energy at all wavenumbers in the MIR or NIR region. The energy passes through a prism (or diffraction grating or monochromator) so that only the energy in a narrow wavenumber range is allowed through. The energy then passes through an aperture to limit the beam diameter, and then into the sample chamber with or without a sample. Finally, the remaining intensity is determined by a detector. To measure a full spectrum, the monochromator must be able to adjust so that radiation of different wavelengths can be let through. By adjusting the monochromator, the entire wavenumber range can be scanned.

If no sample is present, the intensity is denoted as  $I_0$ . If a sample is present, the detected intensity is denoted as  $I$ . Transmission is defined as  $I/I_0$ . Absorbance is defined as  $-\log(I/I_0) = \log(I_0/I)$ . Hence, if the sample does not absorb the energy at a given wavenumber, the transmission is 100%, and the absorbance is 0. If the sample absorbs significantly, the transmission becomes much less than 1 and absorbance would have a positive value. When the absorbance is greater than 2 or 3, there is very little energy detectable after passing through the sample; the error then becomes very large and absorbance loses its quantitative meaning.

Since the 1990s, Fourier transform infrared spectrometers have become more widely available and classical infrared spectrometers are no longer commonly used. Nowadays, when IR instrumentation is discussed, it is implicitly FTIR, not the classical wavelength-dispersive IR. Classical IR spectrometers have distinct disadvantages compared with FTIR: (i) they only use a small fraction of the total energy from the source at every instant of time, wasting most of the energy and leading to large noise/signal ratios, (ii) one scan takes a long time (several minutes to an hour, depending on the precision needed), (iii) they require intensity calibrations, and (iv) their signals are affected by stray light.

Fourier transform infrared (FTIR) technology eliminates all of the above disadvantages. In FTIR, the monochromator is replaced by a unit (Michelson interferometer) that uses a beamsplitter to split the input beam into two equal parts, which are reflected back by mirrors and recombined. The recombined light then goes to the sample and then to the detector. The recombination leads to interference, so that the recombined signal is equivalent to the Fourier transform of the input signal. That is, in the input beam the intensity depends on the wavenumber, which cannot be detected by the detector, whereas in the recombined beam the intensity depends on time, which can be detected by the detector. After the detector records the intensity versus time signal, the digital data are then Fourier transformed back through software into a function of intensity versus wavenumber. Without the sample, the same signal as the input is obtained. With absorption by the sample, the spectrum would display the absorption bands.

### Different types of IR spectra

IR spectra can be taken either on powders mixed and pressed with KBr into a disc, or on glass or single crystal wafers. Powder spectra are for qualitative identification, but for quantitative analyses of geological materials, spectra of glass plates or single-crystal wafers are most often obtained.

If the sample is isotropic (including glass and isometric minerals), then a typical FTIR configuration with a nonpolarized (or partially polarized because the mirrors and beamsplitter can cause polarization) beam works well for quantitative analyses. If the sample is anisotropic (all minerals with symmetry lower than isometric minerals), the absorption band intensity will depend on the orientation of the crystal as well as how the E (electric field) vector is oriented.

Libowitzky and Rossman (1996) discussed the principles of quantitative IR measurements of anisotropic minerals. In addition to transmission spectra, in which light passes through the sample and goes to the detector, reflectance spectra can also be taken (e.g., Moore et al. 2000), in which light strikes the surface of a sample, is reflected, and then reaches the detector. Peaks in reflectance spectra are usually weak and reflectance spectra are more difficult to quantify. For quantitative analyses, transmission spectra have been the method of choice except for remote sensing.

Depending on the infrared wavenumber region one is interested in, it is necessary to decide whether to obtain MIR spectra (typically 40-400  $\text{mm}^{-1}$ ), using the energy source, beamsplitter and detector for the MIR region, or to obtain NIR spectra (typically 200-900  $\text{mm}^{-1}$ ). A typical IR instrument is set up for MIR analyses, with a Globar (a silicon carbide rod heated electrically to high temperature so that it glows) energy source, a KBr beamsplitter, and a DTGS (Deuterated Triglycine Sulfate) detector. If one needs to obtain NIR spectra, a special energy source (tungsten light source), beamsplitter, and detector ( $\text{LN}_2$ -cooled InSb) must be added. For  $\text{CO}_2$  analyses, MIR bands are used. For  $\text{H}_2\text{O}$  analyses, NIR bands are often used (except for the bending mode) for analyzing water-rich glasses (e.g.,  $\geq 0.3$  wt%  $\text{H}_2\text{O}_i$ ), whereas either NIR or MIR can be used for water-poor glasses (e.g.,  $\leq 0.5$  wt%  $\text{H}_2\text{O}_i$ ) and most minerals. To measure small samples, an FTIR microscope system is necessary, typically equipped with a  $\text{LN}_2$ -cooled MCT (mercury-cadmium-telluride) detector that can be used with either MIR or NIR source and beamsplitter.

If large samples are available and there is no need to measure the spatial variation of species concentration, then the main chamber of the spectrometer is often used. An advantage of the main chamber is that the rays in the incidence beam are roughly parallel and the beam is perpendicular to the sample surface. Hence, the light will not bend much and the light path length is similar to the sample thickness so results are more reproducible from one lab to another. On the other hand, if the sample is small (e.g.,  $< 0.1$  mm in diameter) or one needs high spatial resolution (e.g., measurement of a diffusion profile), then a FTIR microscope must be used, in which the incidence beam is focused (converged) to a thin beam. However, the rays in the beam are not parallel but are first converging, reaching a minimum beam diameter, and then diverging. Therefore, the beam will be refracted in the sample, and the beam path is longer than the sample thickness, so reproducibility between different laboratories is not as good as in the case when main chambers are used. Furthermore, because light rays in the beam focused by a microscope are not parallel, they diverge in the sample, leading to a spatial resolution inferior to that indicated by the aperture size. For example, Ni and Zhang (2008) showed that with a 20  $\mu\text{m}$  wide aperture and a sample thickness of 200  $\mu\text{m}$ , the actual spatial resolution (FWHM) is about 30  $\mu\text{m}$ .

### Calibration

In order to convert an IR absorption peak intensity from an infrared spectrum to a concentration, it is necessary to carry out a calibration using samples with known concentrations of the species of interest. The calibration for total  $\text{H}_2\text{O}$  content ( $\text{H}_2\text{O}_t$ ) and species concentrations is used as example here. No method is available to directly determine the species concentrations in Fe-bearing glasses (i.e., natural glasses), which is a difficulty in the calibration. (For Fe-free glasses, NMR is able to determine the concentration ratio of the two species based on peak area ratio without calibration so that once  $\text{H}_2\text{O}_t$  content is known, concentrations of both  $\text{H}_2\text{O}_m$  and OH can be determined, see Schmidt et al. 2001; Yamashita et al. 2008.) Concentrations of  $\text{H}_2\text{O}_t$  may be determined by manometry (e.g., Epstein and Taylor 1970; Newman et al. 1986), or by Karl-Fischer titration (e.g., Turek et al. 1976; Westrich 1987; Behrens et al. 1996).

According to Beer's law, for dilute solutions, the concentration of a species  $i$  ( $C_i$ ) and the absorbance at a peak for species  $i$  ( $A_i$ ) are related as follows:

$$C_i = \frac{18.015A_i}{\rho d \epsilon_i} \quad (15)$$

where  $\rho$  is the density,  $d$  is the thickness, and  $\epsilon_i$  is the molar absorptivity at this peak. The thickness of the sample is measured using a micrometer. Glass density is measured as a function of  $H_2O_t$ ; for glasses with the same anhydrous composition but different  $H_2O_t$ , the density can often be expressed as  $\rho = \rho_0(1 - aC)$  where  $C$  is the mass fraction of  $H_2O_t$  and  $a$  is a constant (often about 0.6, e.g., see the summary in Table 3 of Zhang 1999). A more accurate expression uses the partial molar volume of  $H_2O$  of  $12.0(\pm 0.5) \times 10^{-6} \text{ m}^3$  (Richet et al. 2000). Either the peak height (linear absorbance) or the peak area (integrated absorbance) may be used for  $A$ . In the literature, peak height is more often used because it is simpler and the precision is about the same (at least for  $H_2O$  species). If  $C$  is the  $H_2O_t$  concentration (mass fraction or weight percent),  $C_1$  is the  $H_2O_m$  concentration, and  $C_2$  is the concentration of  $H_2O$  present in the form of OH (i.e., it is the mass of two OH groups minus one oxygen),  $H_2O_t$  concentration as the sum of  $H_2O_m$  and OH can be expressed as follows, since the  $H_2O_m$  peak occurs at  $\sim 523 \text{ mm}^{-1}$ , and the OH peak occurs at  $\sim 452 \text{ mm}^{-1}$ :

$$C = C_1 + C_2 = \frac{18.015A_{523}}{\rho d \epsilon_{523}} + \frac{18.015A_{452}}{\rho d \epsilon_{452}} \quad (16)$$

where  $A_{523}$  and  $A_{452}$  are the absorbance for the  $523 \text{ mm}^{-1}$  and  $452 \text{ mm}^{-1}$  peaks,  $\epsilon_{523}$  and  $\epsilon_{452}$  are the molar absorptivities for the  $523 \text{ mm}^{-1}$  and  $452 \text{ mm}^{-1}$  peaks.

Based on Equation (16), from the measurement of  $H_2O_t$  concentration by an absolute method, and measurement of peak heights  $A_{523}$  and  $A_{452}$  in an infrared spectrum, one equation relating  $C$ ,  $A_{523}$  and  $A_{452}$  can be obtained. Because there are two unknowns ( $\epsilon_{523}$  and  $\epsilon_{452}$ ) in Equation (16), it is necessary to conduct the analyses over a large range of values of  $C$  to yield numerous linearly independent equations (meaning that  $C_1$  and  $C_2$  concentrations must not be proportional as  $C$  increases) so that both  $\epsilon_{523}$  and  $\epsilon_{452}$  can be determined. A feature of the species equilibrium in the melt (quenched to glass) between  $H_2O_m$  and OH is that the concentrations of the two species are not proportional to each other, allowing the determination of both  $\epsilon_{523}$  and  $\epsilon_{452}$ . One method to obtain  $\epsilon_{523}$  and  $\epsilon_{452}$  from data is through direct multi-linear regression of  $C$  versus  $A_{523}$  and  $A_{452}$  (Newman et al. 1986) by making the intercept be zero. Another method is to rewrite Equation (16) in the following form (Behrens et al. 1996):

$$\frac{18.015A_{523}}{\rho d C} = \epsilon_{523} - \frac{\epsilon_{523}}{\epsilon_{452}} \frac{18.015A_{452}}{\rho d C} \quad (17)$$

and plot  $18.015A_{523}/(\rho d C)$  on the  $y$ -axis versus  $18.015A_{452}/(\rho d C)$  on the  $x$ -axis. The  $y$ -intercept is  $\epsilon_{523}$ , the  $x$ -intercept is  $\epsilon_{452}$ , and the slope is  $-\epsilon_{523}/\epsilon_{452}$ .

The above treatments assume that  $\epsilon_{523}$  and  $\epsilon_{452}$  are constant (independent of  $H_2O_t$ ). Because  $H_2O_t$  in glasses is relatively high (typically a couple of wt%), the assumption may or may not be accurate. For example, Zhang et al. (1997) showed that the  $\epsilon_{523}/\epsilon_{452}$  ratio in rhyolite glasses derived from a calibration based on different samples and the ratio from heating the same sample to different temperatures are different, indicating either the calibrations are not accurate, or  $\epsilon_{523}$  and  $\epsilon_{452}$  depend on  $H_2O_t$ . The uncertainty on  $\epsilon_{523}$  and  $\epsilon_{452}$  affect the species concentrations more than  $H_2O_t$  content. By combining manometry data and heating data, Zhang et al. (1997) carried out a calibration by treating  $\epsilon_{523}$  and  $\epsilon_{452}$  to be a function of  $A_{523}$  and  $A_{452}$ . The calibration by Zhang et al. (1997) works well at  $H_2O_t \leq 3.0 \text{ wt}\%$ , but the error increases as  $H_2O_t$  increases above  $3.0 \text{ wt}\%$  (Zhang and Behrens 2000). Schmidt et al. (2001) found that the molar absorptivities in alkali aluminosilicate glasses are independent of  $H_2O$  concentrations, whereas Yamashita et al. (2008) showed that the molar absorptivities in sodium silicate glasses depend on concentrations. The issue of whether and how molar absorptivities

in various hydrous glasses vary with  $H_2O_t$  at greater  $H_2O_t$  remains to be resolved.

At low  $H_2O_t$  concentrations, the  $355\text{ mm}^{-1}$  peak (fundamental stretching of OH) can be used, which is about a factor of 50 larger than the NIR peaks ( $452\text{ mm}^{-1}$  and  $523\text{ mm}^{-1}$ ). At low  $H_2O_t$ , OH is the dominant species. Hence, the calibration involves only one molar absorptivity (e.g., Dobson et al. 1989; Dixon et al. 1995). For a sample of about 1 mm thickness, the detection limit of  $H_2O_t$  using the  $355\text{ mm}^{-1}$  peak is about 1 ppm. Examples for the use of the  $355\text{ mm}^{-1}$  peak include investigation of water diffusion in basalt melt (Zhang and Stolper 1991). For the IR measurement of molecular  $CO_2$  and  $CO_3^{2-}$  concentrations, the calibration procedures are similar when only one of the two species is present in the given glass.

Sample preparation for infrared analyses is in general straightforward. The sample must be doubly polished and the thickness well-determined. For transmission infrared spectra, the surface of the sample must be cleaned without leaving a residue that may contribute to the species to be measured. The surface along the IR path must not be covered by plastic tape or double-sided tape. Cracks, especially cracks filled by epoxy, must be avoided because epoxy has a large IR signal that would superimpose on the bands of interest.

### Applications to geology

The most important geological applications of FTIR are to analyze total  $H_2O$  concentrations, concentrations of  $H_2O$  species, total  $CO_2$  concentrations, and concentrations of  $CO_2$  species in natural silicate glasses and minerals. Absorption bands involving H and C are often at much higher wavenumbers and far separated from structural IR bands due to silicate network vibrations and are hence easily quantified. This is because the masses of H and C are small (leading to small values of reduced mass, Eqn. 14), so that at the same bond strength (force constant  $k$ ), the vibrational frequencies (or wavenumbers) are much higher than those for other species (Eqn. 13).

Stolper (1982a,b) pioneered infrared studies of dissolved water in natural silicate melts and glasses, and was first in the earth sciences to discover the presence of both molecular  $H_2O$  and hydroxyl groups in silicate melts and glasses and to study the equilibrium between  $H_2O$  molecules and OH groups. At high total  $H_2O$  contents (such as  $> 4\text{ wt}\%$ ), the concentration of  $H_2O_m$  becomes higher than that of OH.

With the advancement of IR microbeam techniques,  $H_2O$  diffusion profiles can be measured, along with species concentrations and total concentration using step scans (Zhang et al. 1991a; Zhang and Stolper 1991) or automatic line scans (e.g., Zhang and Behrens 2000). The analyses of data on species concentration demonstrated that  $H_2O_m$  is the diffusing species and that OH is largely immobile compared to  $H_2O_m$  (Zhang et al. 1991a; Doremus 1995; Zhang and Behrens 2000; Behrens et al. 2004; Liu et al. 2004b; Ni and Zhang 2008; Ni et al. 2009a,b; Wang et al. 2009), an inference reached earlier by some glass scientists based on the shape of diffusion profiles representing total  $H_2O$  at low  $H_2O_t$  contents (Doremus 1969, 1973; Ernsberger 1980; Smets and Lommen 1983; Nogami and Tomozawa 1984). The comparison between  $H_2O$  diffusion and  $^{18}O$  “self” diffusion also led to the realization that oxygen diffusion in melts and minerals in the presence of  $H_2O$  often occurs through  $H_2O$  diffusion (Zhang et al. 1991b; Behrens et al. 2007; see also *ab initio* calculation results by McConnell 1995). Infrared spectroscopy has also been applied to investigate diffusion of hydrous components in olivine (Mackwell and Kohlstedt 1990), pyroxene (Skogby and Rossman 1989; Ingrin et al. 1995), and garnet (Wang et al. 1996). Other applications include speciation studies (e.g., Ihinger et al. 1999; Liu et al. 2004a; Hui et al. 2009), solubility studies (e.g., Blank et al. 1993; Tamic et al. 2001; Liu et al. 2005), and kinetic and geospeedometry studies (Zhang et al. 1997b; Zhang et al. 2000; Wallace et al. 2003).

IR measurements of  $H_2O$  species concentrations and profiles are much more difficult in glasses with high FeO concentration because (i) the degree of transparency of the glass is

reduced and (ii) the broad Fe absorption band in the NIR overlaps with the  $523\text{ mm}^{-1}$  peak (e.g., Ohlhorst et al. 2001; Liu et al. 2004a,b; Ni et al. 2009b). One way to get around this difficulty is to use Fe-free melts using equimolar amounts of MgO and CaO to replace FeO (e.g., Ni et al. 2009a).

Stolper and coworkers also pioneered the infrared study of  $\text{CO}_2$  in silicate melts and glasses (Fine and Stolper 1985, 1986). It was found that dissolved  $\text{CO}_2$  in polymerized (or silicic) melts is present as molecular  $\text{CO}_2$ . As the melt composition changes from rhyolite to andesite to dacite to basalt, increasingly more of the dissolved  $\text{CO}_2$  is present in the form of carbonate ions ( $\text{CO}_3^{2-}$ ). Infrared measurements of  $\text{CO}_2$  and  $\text{CO}_3^{2-}$  concentrations have been applied to investigate total  $\text{CO}_2$  diffusion (Blank 1993; Sierralta et al. 2002; Nowak et al. 2004) and solubility (e.g., Blank et al. 1993; Tamic et al. 2001; Behrens 2010).

### SYNCHROTRON X-RAY FLUORESCENCE MICROANALYSIS ( $\mu$ -SRXRF)

The  $\mu$ -SRXRF (“microscopic”-synchrotron radiation X-ray fluorescence) technique is a well-established microanalytical technique for trace element analysis, which in the last decades has been continuously improved in its instrumentation and in the quantification of X-ray spectra (see reviews by Smith and Rivers 1995, Haller and Knöchel 1996, Janssens et al. 2000, Hansteen et al. 2000, Sutton et al. 2002). Due to the outstanding properties of synchrotron radiation, such as high brightness, high degree of polarization and extremely low divergence,  $\mu$ -SRXRF offers a number of interesting advantages in comparison with other trace element analytical tools: (1) non-destructive analysis which enables long-time acquisitions under steady-state conditions, even for fragile biological materials, (2) easy quantification by using a standard-free fundamental-parameter approach, (3) the possibility of calculating matrix effects by using fundamental-parameter approaches, (4) the collection of multi-element spectra with one acquisition; (5) low detection limits (ppm level) at a high spatial resolution, and (6) sensitivity ranging over six orders of magnitude.

In the last decades, the  $\mu$ -SRXRF technique has been applied to many disciplines of the earth sciences (see the overviews by Smith and Rivers 1995 and Sutton et al. 2002). Baker and Watson (1988) and Baker (1989, 1990) were the first to apply  $\mu$ -SRXRF to study trace element diffusion in silicate glasses, measuring diffusion profiles of a few selected elements. Koepke and Behrens (2001) improved the technique by using a modern energy dispersive detector to simultaneously analyze 18 trace element diffusivities in a single experiment. With this multi-element approach, the relative errors of the diffusion coefficients are minimized, resulting in “internally consistent” data sets (Mungall et al. 1999; Koepke and Behrens 2001).

#### Instrumental setup, spectra acquisition and data processing

Most studies on diffusion in silicate glasses using  $\mu$ -SRXRF as an analytical tool have been performed at the HASYLAB synchrotron source of the DESY in Hamburg, Germany (Koepke and Behrens 2001; Koepke et al. 2003; Hahn et al. 2005; Behrens and Haack 2007; Behrens and Hahn 2009). Therefore, the experimental  $\mu$ -SRXRF setup installed at beamline L of the HASYLAB is described here in detail (Fig. 31). Similar setups can be found in other synchrotron radiation facilities around the world (Brown et al. 2006)

For the measurements, the “white” X-ray continuum of a bending magnet is used, which shows maximum brilliance at 16.0 keV (critical energy). During routine analysis, the resulting X-ray spectral distribution enables simultaneous K-shell excitation of elements with atomic numbers from 25 (Mn) to 82 (Pb). The excitation conditions are normally optimized for single elements or element groups by using suitable absorbers. For minimizing the background radiation caused by Rayleigh and Compton scattering, the “horizontal” geometry is used, (for details see Haller and Knöchel 1996; Janssens et al. 2000), for which the radiation is detected

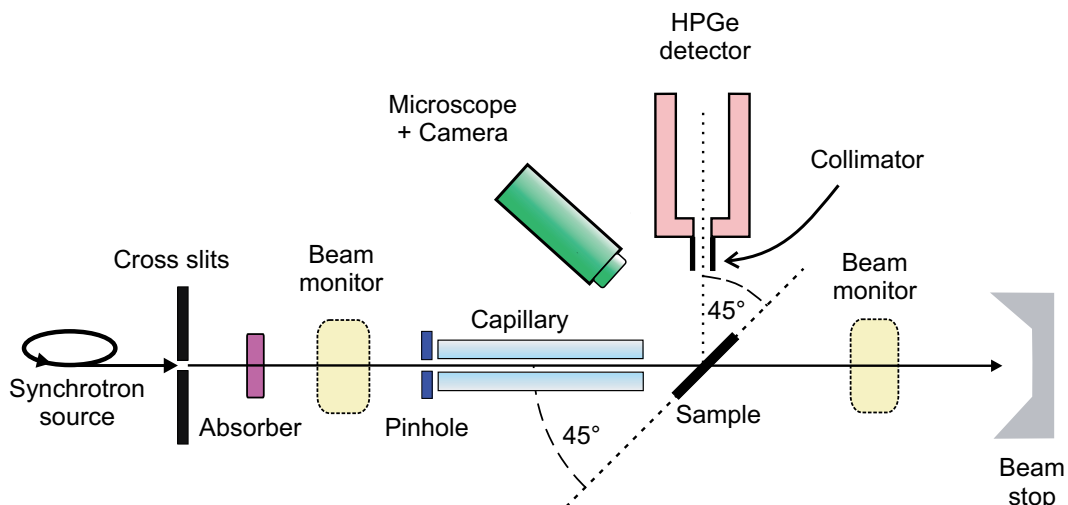


**Figure 31.** Schematic drawing of the  $\mu$ -SRXRF analytical setup installed at beamline L of DORIS III synchrotron radiation source at HASYLAB (view from the top).

in the plane of maximum polarization at an angle of  $90^\circ$  (Fig. 31). For this geometry, the angle of incidence of the synchrotron beam on the sample is  $45^\circ$ . For a sufficiently high spatial resolution, a reduction of the diameter of the incoming synchrotron beam is necessary, which can be accomplished by using different types of glass capillaries as collimators (e.g., Haller et al. 1995; Janssens et al. 2000). For most diffusion studies, the beam size of the incoming synchrotron beam on the sample varies between 2 and 20  $\mu\text{m}$ .

Samples analyzed are typically thin sections of diffusion couples, usually oriented so that the incoming synchrotron beam is perpendicular to the direction of diffusion (Fig. 32). Because the high-energy synchrotron beam penetrates through the whole thickness of the

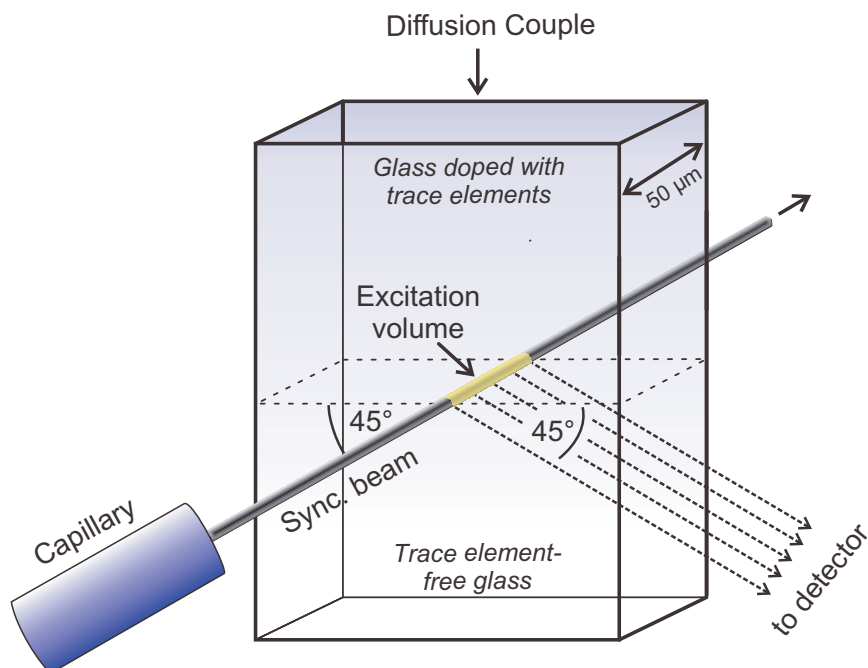


**Figure 32.** Sample geometry for the analysis of trace element diffusion profiles in the  $\mu$ -SRXRF spectrometer.

sample without significant loss of energy, the variation with depth cannot be resolved. This characteristic is similar to transmission infrared spectroscopy, but differs from EMPA, LA-ICP-MS or SIMS, where volumes from near-surface spots are analyzed. Therefore, for diffusion studies using  $\mu$ -SRXRF analyses, the contact plane of the diffusion couple is aligned parallel to the plane of the incoming beam and the direction of detection.

Fluorescence-derived X-ray photons, the  $K_{\alpha}$  lines of elements, are detected with an energy-dispersive high-purity germanium detector. Due to the high brilliance of the synchrotron source, acquisition times are generally low, e.g., 240 seconds in the studies of Koepke and Behrens (2001) and Hahn et al. (2005) resulting in detection limits in the range of 1 to 15 ppm for the measured elements. Peak fitting and determination of the net peak areas are routinely performed using commercial software (e.g., Van Espen et al. 1977), with the option of processing multi-element spectra (Fig. 33a). For example, in the study of Hahn et al. (2005) 24 trace elements were measured simultaneously. Net intensities are routinely normalized to an internal standard (typically Ca or Fe) to correct for variations in synchrotron beam intensity, dead time and thickness of the sample. For most trace element diffusion studies using diffusion couples, the major element matrix is identical throughout the sample. Therefore, the normalized intensities are directly proportional to the concentration of trace elements in the glass, and the determination of absolute concentrations is not necessary. Typical profiles of trace elements with different geochemical behaviors are presented in Figure 33b. Normalized peak areas may be used directly for the calculation of diffusion coefficients.

### Sample preparation

Samples for typical trace element diffusion studies using  $\mu$ -SRXRF are couples of trace element-doped and undoped silicate melts (for experimental details see Koepke and Behrens 2001; Koepke et al. 2003; Hahn et al. 2005). After experimental runs, capsules are cut perpendicular to the contact plane of the couple for preparation of doubly polished thin sections. Due to the complete penetration of the incoming beam through the sample, the spatial resolution of this method is strongly dependent on the sample thickness. Moreover, since self-absorption is relatively high for the elements used for internal standardization, and practically negligible for elements of high atomic numbers, it must be ensured that the samples are of homogeneous thickness. Therefore, samples for  $\mu$ -SRXRF studies have to be prepared as reasonably thin sections; for example,  $50 \pm 1 \mu\text{m}$  thick sections were used in the studies of Koepke and Behrens (2001) and Hahn et al. (2005). It should be noted that a decrease of sample thickness will also reduce the intensity of the fluorescence lines, resulting in lower precision and poorer detection limits of the analyzed elements.

### Applications of $\mu$ -SRXRF for measuring trace element diffusivities in silicate melts

Pioneering studies using  $\mu$ -SRXRF to investigate diffusion in silicate glasses were conducted by Baker and Watson (1988), who measured diffusion profiles in complex Cl- and F-bearing silicate melts, Baker (1989) who investigated tracer versus trace element diffusion using Sr isotopes, and Baker (1990) who analyzed Rb, Zr, Sr and Nb concentration profiles generated during chemical interdiffusion between a dacite and a rhyolite melt. Carroll et al. (1993) measured Kr diffusion in different silicic melts including pure  $\text{SiO}_2$  and rhyolitic compositions. All of these studies considered only a few selected elements, which were analyzed by  $\mu$ -SRXRF. Ten years later, Koepke and Behrens (2001) benefited from advancements in  $\mu$ -SRXRF permitting the collection of multi-element spectra with one acquisition, and started to obtain "internally consistent" data sets for trace element diffusivities in a synthetic haploandesitic melt with and without added water. This approach minimizes the relative errors of the diffusion coefficients, and such datasets provide the opportunity to explore systematic dependencies of diffusivities on ionic charge and radius. Doped elements can be grouped geochemically as LFSE (Rb, Sr, Ba), REE (La, Nd, Sm, Eu, Gd, Er, Yb, Y), HFSE (Ti, Zr, Nb, Hf, Ta), and transition elements

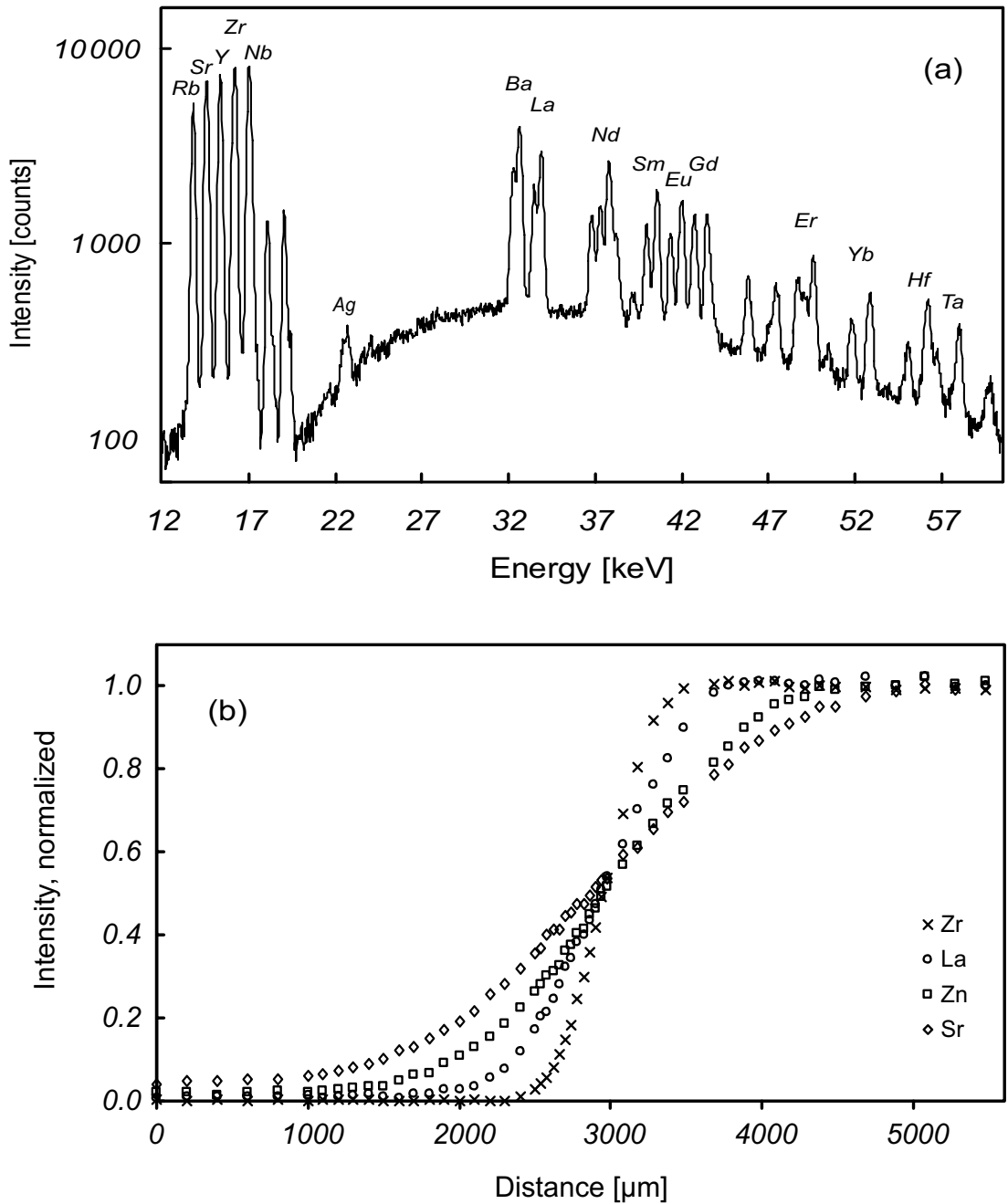


**Figure 33.** (a)  $\mu$ -SRXRF spectrum of a haploandesitic glass doped with various trace elements at the  $\sim 300$  ppm level, which was used as starting material in the trace element diffusion study of Koepke and Behrens (2001). Only the  $K\alpha$ -lines are indicated. Above  $\sim 32$  keV both  $K\alpha_1$  and  $K\alpha_2$  lines are visible. Peaks not labeled correspond to  $K\beta$ -lines. Conditions for the  $\mu$ -SRXRF measurements: 20- $\mu$ m capillary; acquisition time of 400 seconds (real time); Al absorber of 1 mm thickness. The presence of Ag is a due to a contamination resulting from sample polishing. (b) Diffusion profiles for selected trace elements measured with  $\mu$ -SRXRF obtained from a diffusion couple of haploandesitic melt containing 5 wt%  $H_2O$ . Experimental conditions: Temperature = 1583 K; pressure = 500 MPa; run time = 1 hour. Conditions for the  $\mu$ -SRXRF measurements: Acquisition time = 240 seconds (real time) for each spectrum, resulting in  $\sim 4$  h for the whole profile; absorber = 1 mm thick Al; capillary = diameter of 20  $\mu$ m, non-focusing. The profiles are normalized to the peak net area of Ca. Shown are examples for trace elements of different chemical behavior with fast (Sr), medium (Zn, La), and slow (Zr) diffusivity. For details see Koepke and Behrens (2001).

(Sc, Cr, Fe, Ni, Zn). Most of the investigated elements showed a linear relation between log diffusivity and log viscosity, permitting the prediction of diffusivities in hydrous andesite systems at various conditions. This relation could potentially be used to estimate trace element diffusivities for silicate melts with different compositions provided viscosity data are available. Due to the simultaneous measurement of all trace elements, ratios between diffusion coefficients can be obtained with high precision. The precision of the analytical method is determined mainly by the scatter of data points along a profile, which decreases with increasing intensity of the fluorescence signal of the element (e.g., high fluorescence signal for elements like Y and Zr; and low signals for elements like Ta or Hf; see Fig. 33). This results in a slightly different fit parameter when evaluating duplicate analyses of concentration profiles from the same sample. Based on duplicate profiles in different samples, the elements can be divided into three groups: those with high reproducibility of diffusion coefficients (within 3-5 %): Rb, Sr, Y, Zr, Nb; those with intermediate reproducibility (within 10-15 %): Ba, Cr, Fe, Ni, Zn, light REE; and those with low reproducibility (within 30-50 %): Yb, Er, Hf (for details and individual errors of estimated diffusion coefficients see Koepke and Behrens 2001).

Difficulties arise in systems with many trace elements in complex matrices due to spectral interferences between elements of interest. Behrens and Hahn (2009) overcame this problem by separating the conflicting trace elements into two sets. Hahn et al. (2005) used the same analytical equipment in measuring 24 trace elements, representing different geochemical groups, in hydrous rhyolitic glasses. These authors applied both  $\mu$ -SRXRF and SIMS in analyzing the concentration profiles, and found that multiple diffusivities derived from both techniques are in very good agreement for most elements. They showed that some trace elements could not be reliably quantified with  $\mu$ -SRXRF. These include Ta and Pb (these elements are used for detector collimator material), Ti, V (low energy of  $K_{\alpha}$  lines), Co ( $K_{\alpha}$  lines for Co have overlaps with Fe  $K_{\alpha}$  lines) and Cr, Ni, Cu, Zn (overlaps with L-lines of REEs). In contrast to  $\mu$ -SRXRF, in SIMS analyses elements are measured sequentially, which is much more time-consuming, so fewer trace elements could be analyzed in a single session. In addition, some elements are difficult to analyze with SIMS due to isobaric interferences (for example, interference of NaSi with V, and interference of CaO with Ni) or very low yields (e.g., Sn). Recently Behrens and Haack (2007) and Behrens and Hahn (2009) obtained “internally consistent” data sets for trace element diffusivities using  $\mu$ -SRXRF in soda-lime-silicate glass melts and in potassium-rich trachytic/phonolitic melts, respectively.

## ACKNOWLEDGMENTS

We thank Harald Behrens for his careful review of the chapter and insightful comments. RLH acknowledges NSF (EAR-0622775) for support of the ASU SIMS facilities and helpful advice from J. Ganguly (University of Arizona), J. Boyce (UCLA) and Y. Guan (Caltech). YZ acknowledges support by NSF (EAR-0838127). DJC thanks Jon Price for helpful advice and comments on various sections of the chapter.

## REFERENCES

- Aines RD, Rossman GR (1984) Water content of mantle garnets. *Geology* 12:720-723
- Alonso U, Missana T, Patelli A, Rigato V (2007a) Bentonite colloid diffusion through the host rock of a deep geological repository. *Phys Chem Earth* 32:469-476
- Alonso U, Missana T, Patelli A, Rigato V, Ravagnan J (2007b) Colloid diffusion in crystalline rock; an experimental methodology to measure diffusion coefficients and evaluate colloid size dependence. *Earth Planet Sci Lett* 259:372-383
- Amsel G, Samuel D (1967) Microanalysis of the stable isotopes of oxygen by means of nuclear reactions. *Anal Chem* 39:1689-1698

- Anderson TF (1969) Self-diffusion of carbon and oxygen in calcite by isotope exchange with carbon dioxide. *J Geophys Res* 74:3918-3932
- Anderson TF (1972) Self-diffusion of carbon and oxygen in dolomite. *J Geophys Res* 77:857-861
- Arredondo EH, Rossman GR (2002) Feasibility of determining the quantitative OH content of garnet with Raman spectroscopy. *Am Mineral* 87:307-311
- Baker DR (1989) Tracer versus trace element diffusion: Diffusional decoupling of Sr concentrations from Sr isotope composition. *Geochim Cosmochim Acta* 53:3015-3023
- Baker DR (1990) Chemical interdiffusion of dacite and rhyolite: Anhydrous measurements at 1 atm and 10 kbar, application of transition state theory and diffusion in zoned magma chambers. *Contrib Mineral Petrol* 104:407-423
- Baker DR, Watson EB (1988) Diffusion of major and trace elements in compositionally complex Cl- and F-bearing silicate melts. *J Non-Cryst Solids* 102:62-70
- Baker M, Taylor A (1969) Cation diffusion in fluorite single crystals. *J Phys Chem Solids* 30:1003-1007
- Baldwin SL, Harrison TM, Fitz Gerald JD (1990) Diffusion of  $^{40}\text{Ar}$  in metamorphic hornblende. *Contrib Mineral Petrol* 105:691-703
- Barbour JC, Doyle BL (1995) Elastic recoil detection: ERD. *In: Handbook of Modern Ion Beam Materials Analysis*. Tesmer JR, Nastasi MA (eds) Materials Research Society, p 83-138
- Baschek G, Johannes W (1995) The estimation of NaSi-CaAl interdiffusion rates in peristerite by homogenization experiments. *Eur J Mineral* 7:295-307
- Baxter EF, Clay PL, Kelley SP, Watson EB, Cherniak DJ, Thomas JB (2006) Two diffusive pathways for argon in quartz and feldspar. Abstracts of the 16th annual V. M. Goldschmidt conference. *Geochim Cosmochim Acta* 70:A41
- Baxter EF (2010) Diffusion of noble gases in minerals. *Rev Mineral Geochem* 72:509-557
- Behrens H (2010) Ar, CO<sub>2</sub> and H<sub>2</sub>O diffusion in silica glass at 2 kbar pressure. *Chem Geol* 272: 40-48
- Behrens H, Haack M (2007) Cation diffusion in soda-lime-silicate glass melts. *J Non-Cryst Solids* 353:4743-4752
- Behrens H, Hahn M (2009) Trace element diffusion and viscous flow in potassium-rich trachytic and phonolitic melts. *Chem Geol* 259:63-77
- Behrens H, Johannes W, Schmalzried H (1990) On the mechanisms of cation diffusion processes in ternary feldspars. *Phys Chem Miner* 17:62-78
- Behrens H, Romano C, Nowak M, Holtz F, Dingwell DB (1996) Near-infrared spectroscopic determination of water species in glasses of the system  $\text{MAlSi}_3\text{O}_8$  (M=Li, Na, K): an interlaboratory study. *Chem Geol* 128:41-63
- Behrens H, Roux J, Neuville DR, Siemann M (2006) Quantification of dissolved H<sub>2</sub>O in silicate glasses using confocal microRaman spectroscopy. *Chem Geol* 229:96-112
- Behrens H, Zhang Y (2001) Ar diffusion in hydrous silicic melts: implications for volatile diffusion mechanisms and fractionation. *Earth Planet Sci Lett* 192:363-376
- Behrens H, Zhang Y, Leschik M, Miedenbeck M, Heide G, Frischat GH (2007) Molecular H<sub>2</sub>O as carrier for oxygen diffusion in hydrous silicate melts. *Earth Planet Sci Lett* 254:69-76
- Behrens H, Zhang Y, Xu Z (2004) H<sub>2</sub>O diffusion in dacitic and andesitic melts. *Geochim Cosmochim Acta* 68:5139-5150
- Béjina F, Jaoul O (1996) Silicon self-diffusion in quartz and diopside measured by nuclear micro-analysis methods. *Phys Earth Planet Inter* 97:145-162
- Bell DR, Hervig RL, Buseck PR, Aulbach S (2009) Lithium isotope analysis of olivine by SIMS: Calibration of a matrix effect and application to magmatic phenocrysts. *Chem Geol* 258:5-16
- Bell DR, Rossman GR (1992) Water in Earth's mantle: The role of nominally anhydrous minerals. *Science* 255:1391-1397
- Beran A, Libowitzky E (2004) *Spectroscopic Methods in Mineralogy: University Textbook*. Eotvos University Press, Budapest
- Berard MF (1971) Self-diffusion of Ca in single-crystal CaF<sub>2</sub>. *J Am Ceram Soc* 54:144-146
- Bertran-Alvarez Y, Jaoul O, Liebermann RC (1992) Fe-Mg interdiffusion in single crystal olivine at very high pressure and controlled oxygen fugacity; technological advances and initial data at 7 GPa. *Phys Earth Planet Inter* 70:102-118
- Blackburn TJ, Stockli DF, Walker JD (2007) Magnetite (U-Th)/He dating and its application to the geochronology of intermediate to mafic volcanic rocks. *Earth Planet Sci Lett* 259:360-371
- Blank JG (1993) An Experimental Investigation of the Behavior of Carbon Dioxide in Rhyolitic Melt, Ph.D. dissertation, California Institute of Technology, Pasadena
- Blank JG, Stolper EM, Carroll MR (1993) Solubilities of carbon dioxide and water in rhyolitic melt at 850 °C and 750 bars. *Earth Planet Sci Lett* 119:27-36
- Boyce JW, Hodges KV, Olszewski WJ, Jercinovic MJ (2005) He diffusion in monazite: implications for (U-Th)/He thermochronometry. *Geochem Geophys Geosyst* 6:Q12004

- Brady JB, McCallister RH (1983) Diffusion data for clinopyroxenes from homogenization and self-diffusion experiments, *Am Mineral* 68:95-105
- Brady JB, Yund RA (1983) Interdiffusion of K and Na in alkali feldspars; homogenization experiments. *Am Mineral* 68:106-111
- Brown Jr GE, Sutton SR, Calas G (2006) User facilities around the world. *Elements* 2:9-14
- Busigny V, Cartigny P, Philippot P, Javoy M (2003) Ammonium quantification in muscovite by infrared spectroscopy. *Chem Geol* 198:21-31
- Busigny V, Cartigny P, Philippot P, Javoy M (2004) Quantitative analysis of ammonium in biotite using infrared spectroscopy. *Am Mineral* 89:1625-1630
- Carroll MR (1991) Diffusion of Ar in rhyolite, orthoclase and albite composition glasses. *Earth Planet Sci Lett* 103:156-168
- Carroll MR, Sutton SR, Rivers ML, Woolum DS (1993) An experimental study of krypton diffusion and solubility in silicic glass. *Chem Geol* 109:9-28
- Castaing R (1951) Application des Sondes Électroniques à une Méthode D'analyse Ponctuelle Chimique et Crystallographique. Ph.D. Thesis. Univ. of Paris
- Chen JH, Harvey WW (1975) Cation self-diffusion in chalcopyrite and pyrite. *Metallurg Trans B (Process Metallurgy)* 6B:331-339
- Chen WK, Peterson NL (1980) Iron diffusion and electrical conductivity in magnesio-wüstite solid solutions (Mg, Fe)O. *J Phys Chem Solids* 41:335-339
- Chen WK, Peterson NL. (1975) Effect on the deviation from stoichiometry on cation self-diffusion and isotope effect in wüstite, Fe<sub>1-x</sub>O. *J Phys Chem Solids* 36:1097-1103
- Cheng H, Shen H, Yang F, Tang J (1993) Cross sections for non Rutherford backscattering of <sup>4</sup>He from some light elements. *Chinese J Nucl Phys* 15:333-336
- Cherniak DJ (1995a) Diffusion of Pb in plagioclase and K-feldspar measured by Rutherford Backscattering spectroscopy and resonant nuclear reaction analysis. *Contrib Mineral Petrol* 120:358-371
- Cherniak DJ (1996) Strontium diffusion in sanidine and albite, and general comments on Sr diffusion in alkali feldspars. *Geochim Cosmochim Acta* 60:5037-5043
- Cherniak DJ (1997) An experimental study of Sr and Pb diffusion in calcite, and implications for carbonate diagenesis and metamorphism. *Geochim Cosmochim Acta* 61:4173-4179
- Cherniak DJ (2000) Rare earth element diffusion in apatite. *Geochim Cosmochim Acta* 64:3871-3885
- Cherniak DJ (2003) Silicon self-diffusion in single-crystal natural quartz and feldspar. *Earth Planet Sci Lett* 214:655-668
- Cherniak DJ (2008) Si diffusion in zircon. *Phys Chem Miner* 35:179-187
- Cherniak DJ, Lanford WA (2001) Nuclear Reaction Analysis. *In: Non-Destructive Elemental Analysis*. Alfassi Z, (ed.) Blackwell Science, p 308-338
- Cherniak DJ, Pyle JM (2008) Thorium diffusion in monazite. *Chem Geol* 256:52-61
- Cherniak DJ, Ryerson FJ (1993) A study of strontium diffusion in apatite using Rutherford Backscattering and ion implantation. *Geochim Cosmochim Acta* 57:4653-4662
- Cherniak DJ, Watson EB (1992) A study of strontium diffusion in K-feldspar, Na-K feldspar and anorthite using Rutherford Backscattering Spectroscopy. *Earth Planet Sci Lett* 113:411-425
- Cherniak DJ, Watson EB (1994) A study of strontium diffusion in plagioclase using Rutherford Backscattering Spectroscopy. *Geochim Cosmochim Acta* 58:5179-5190
- Cherniak DJ, Watson EB (2001) Pb diffusion in zircon. *Chem Geol* 172:5-24
- Cherniak DJ, Watson EB (2007) Ti diffusion in zircon. *Chem Geol* 242:473-486
- Cherniak DJ, Hanchar JM, Watson EB (1997a) Diffusion of tetravalent cations in zircon. *Contrib Mineral Petrol* 127:383-390
- Cherniak DJ, Hanchar JM, Watson EB (1997b) Rare earth diffusion in zircon. *Chem Geol* 134:289-301
- Cherniak DJ, Lanford WA, Ryerson FJ (1991) Lead diffusion in apatite and zircon using ion implantation and Rutherford Backscattering techniques. *Geochim Cosmochim Acta* 55:1663-1673
- Cherniak DJ, Watson EB, Grove M, Harrison TM (2004a) Pb diffusion in monazite: a combined RBS/SIMS study. *Geochim Cosmochim Acta* 68:829-840
- Cherniak DJ, Watson EB, Thomas JB (2009) He diffusion in zircon and apatite. *Chem Geol* 268:155-166
- Cherniak DJ, Watson EB, Wark DA (2007) Ti diffusion in quartz. *Chem Geol* 236:65-74
- Cherniak DJ, Zhang XY, Nakamura M, Watson EB (2004b) Oxygen diffusion in monazite. *Earth Planet Sci Lett* 226:161-174
- Cherniak DJ, Zhang XY, Wayne NK, Watson EB (2001) Sr, Y and REE diffusion in fluorite. *Chem Geol* 181:99-111
- Choudhury A, Palmer DW, Amsel G, Curlen H, Baruch P (1965) Study of oxygen diffusion in quartz by using the nuclear reaction <sup>18</sup>O(p,α)<sup>15</sup>N. *Solid State Commun* 3:119-122
- Chu WK, Mayer JW, Nicolet MA (1978) Backscattering Spectrometry, Academic Press

- Clement SWJ, Compston W (1990) SIMS at high sensitivity and high mass resolution. *In: Secondary Ion Mass Spectrometry, SIMS VII*. Benninghoven A (ed). J. Wiley & Sons, Chichester, p 815-819
- Colthup NB, Daly LH, Wiberly SE (1990) *Introduction to Infrared and Raman Spectroscopy*. 547 p. Academic Press, Inc., Boston
- Cook GB, Cooper RF (2000) Iron concentration and the physical processes of dynamic oxidation in an alkaline earth aluminosilicate glass. *Am Mineral* 85:397-406
- Cookson JA (1991) Nuclear microprobe and competing techniques. *Nucl Instr Meth* 54:433-439
- Cooper RF, Fanselow JB, Weber JKR, Merkle DR, Poker DB (1996) Dynamics of oxidation of a Fe<sup>2+</sup>-bearing aluminosilicate (basaltic) melt. *Science* 274:1173-1176
- Demarche J, Terwagne G (2006) Precise measurement of the differential cross section from the <sup>16</sup>O( $\alpha$ ,  $\alpha'$ )<sup>16</sup>O elastic reaction at 165° and 170° between 2.4 and 6.0 MeV. *J Appl Phys* 100:124909-1-7
- den Hartog, H, Welch DO, Royce BSH (1972) The diffusion of calcium, phosphorus, and OD-ions in fluorapatite. *Phys Status Solidi* 53:201-212
- Derry DJ, Lees DG, Calvert JM (1981) A study of oxygen self-diffusion in the c-direction of rutile using a nuclear technique. *J Phys Chem Solids* 42:57-64
- Di Muro A, Villemant B, Montagnac G, Scaillet B, Reynard B (2006) Quantification of water content and speciation in natural silicic glasses (phonolite, dacite, rhyolite) by confocal microRaman spectroscopy. *Geochim Cosmochim Acta* 70:2868-2884
- Dimanov A, Ingrin J (1995) Premelting and high-temperature diffusion of calcium in synthetic diopside: an increase of the cation mobility. *Phys Chem Miner* 22:437-442
- Dimanov A, Jaoul O (1998) Calcium self-diffusion in diopside at high temperature: implications for transport properties. *Phys Chem Miner* 26:116-127
- Dimanov A, Jaoul O, Sautter V (1996) Calcium self-diffusion in natural diopside single crystals. *Geochim Cosmochim Acta* 60:4095-4106
- Dimanov A, Sautter V (2000) "Average" interdiffusion of (Fe,Mn)-Mg in natural diopside. *Eur J Mineral* 12:749-760
- Dixon JE, Pan V (1995) Determination of the molar absorptivity of dissolved carbonate in basaltic glass. *Am Mineral* 80:1339-1342
- Dobson PF, Epstein S, Stolper EM (1989) Hydrogen isotope fractionation between coexisting vapor and silicate glasses and melts at low pressure. *Geochim Cosmochim Acta* 53:2723-2730
- Dohmen R, Becker HW, Chakraborty S (2007) Fe-Mg diffusion in olivine; I, Experimental determination between 700 and 1,200 degrees C as a function of composition, crystal orientation and oxygen fugacity. *Phys Chem Miner*, 34:389-407
- Doremus RH (1969) The diffusion of water in fused silica. *In: Reactivity of Solids*. Mitchell JW, Devries RC, Roberts RW, Cannon P (eds) Wiley, New York, p. 667-673
- Doremus RH (1973) *Glass Science*. Wiley, New York
- Doremus RH (1995) Diffusion of water in silica glass. *J Mater Res* 10:2379-2389
- Dumke MF, Tombrello TA, Weller RA, Housley RM, Cirlin EH (1983) Sputtering of the gallium-indium eutectic alloy in the liquid phase. *Surf Science* 124 407-412
- Eiler JM, Graham C, Valley JW (1997) SIMS analysis of oxygen isotopes: Matrix effects in complex minerals and glasses. *Chem Geol*, 138:221-244
- Epstein S, Taylor Jr. HP (1970) The concentration and isotopic composition of hydrogen, carbon and silicon in Apollo 11 lunar rocks and minerals. *Apollo 11 Lunar Science Conference Proc* 2:1085-1096
- Ernsberger FM (1980) The role of molecular water in the diffusive transport of protons in glasses. *Phys Chem Glasses* 21:146-149
- Farley KA (2000) Helium diffusion from apatite: General behavior as illustrated by Durango fluorapatite. *J Geophys Res* 105:2903-2914
- Farley KA (2007) He diffusion systematics in minerals; evidence from synthetic monazite and zircon structure phosphates. *Geochim Cosmochim Acta* 71:4015-4024
- Fechtig H, Kalbitzer S (1966) The diffusion of argon in potassium-bearing solids. *In: Potassium Argon Dating*. Schaeffer OA, Zahringer J (eds) Springer-Verlag, New York, p 68-107
- Fine G, Stolper EM (1985) The speciation of carbon dioxide in sodium aluminosilicate glasses. *Contrib Mineral Petrol* 91:105-121
- Fine G, Stolper EM (1986) Dissolved carbon dioxide in basaltic glasses: concentrations and speciation. *Earth Planet Sci Lett* 76:263-278
- Foland KA (1974) Alkali diffusion in orthoclase. *In: Geochemical Transport and Kinetics*. Hofmann AW, Giletti BJ, Yoder, Jr HS, Yund RA (eds) Carnegie Institution of Washington Publication 634, Carnegie Institution of Washington, Washington DC, p 77-98
- Foland KA, Xu Y (1990) Diffusion of <sup>40</sup>Ar and <sup>39</sup>Ar in irradiated orthoclase. *Geochim Cosmochim Acta* 54:3147-3158
- Fortier SM, Giletti BJ (1991) Volume self-diffusion of oxygen in biotite, muscovite, and phlogopite micas. *Geochim Cosmochim Acta* 55:1319-1330

- Ganguly J (2010) Cation diffusion kinetics in aluminosilicate garnets and geological applications. *Rev Mineral Geochem* 72:559-601
- Ganguly J, Bhattacharya RN, Chakraborty S (1988) Convolution effect in the determination of compositional profiles and diffusion coefficients by microprobe step scans. *Am Mineral* 73:901-909
- Ganguly J, Tazzoli V (1994) Fe<sup>2+</sup>-Mg interdiffusion in orthopyroxene: retrieval from data on intracrystalline exchange reaction. *Am Mineral* 79:930-937
- Ganguly J, Tirone M, Hervig RL (1998) Diffusion kinetics of samarium and neodymium in garnet, and a method for determining cooling rates in rocks. *Science* 281:805-807
- Gardés E, Jaoul O, Montel J, Seydoux-Guillaume A, Wirth R (2006) Pb diffusion in monazite; an experimental study of Pb<sup>2+</sup> ↔ Th<sup>4+</sup> ↔ 2 Nd<sup>3+</sup> interdiffusion. *Geochim Cosmochim Acta* 70:2325-2333
- Gardés E, Montel JM, Seydoux-Guillaume AM, Wirth R (2007) Pb diffusion in monazite: New constraints from the experimental study of Pb<sup>2+</sup> ↔ Ca<sup>2+</sup> interdiffusion. *Geochim Cosmochim Acta* 71:4036-4043
- Genareau K, Clarke AB, Hervig RL (2009) New insight into explosive volcanic eruptions: Connecting crystal-scale chemical changes with conduit-scale dynamics. *Geology* 37:367-370
- Genareau K, Hervig R, Clarke A (2007) Geochemical variations in late-stage growth of volcanic phenocrysts revealed by SIMS depth-profiling. *Am Mineral* 92:1374-1382
- Gérard O, Jaoul O (1989) Oxygen diffusion in San Carlos olivine. *J Geophys Res* 94 B4:4119-4128
- Giletti BJ (1974) Diffusion related to geochronology. *In: Geochemical Transport and Kinetics*. Hofmann AW, Giletti BJ, Yoder, Jr HS, Yund RA (eds) Carnegie Institution of Washington Publication 634, Carnegie Institution of Washington, Washington DC, p 61-76
- Gobrecht H, Nelkowski H, Baars JW, Weigt M (1967) Self diffusion of sulphur in zinc sulphide. *Solid State Commun* 5:777-778
- Goldstein JI, Newbury DE, Joy DC, Lyman CE, Echlin P, Lifshin E, Sawyer L, Michael J (2003) *Scanning Electron Microscopy and X-Ray Microanalysis (Third Edition)*. Kluwer Academic/Plenum Publishers
- Grove M, Harrison TM (1996) <sup>40</sup>Ar\* diffusion in Fe-rich biotite. *Am Mineral* 81:940-951
- Grove TL, Baker MB, Kinzler RJ (1984) Coupled CaAl-NaSi diffusion in plagioclase feldspar: experiments and applications to cooling rate speedometry. *Geochim Cosmochim Acta* 48:2113-2121
- Hahn M, Behrens H, Tegge-Schüring A, Koepke J., Rickers K, Falkenberg G, Wiedenbeck M (2005) Trace element diffusion in rhyolitic melts: comparison between synchrotron radiation X-ray fluorescence microanalysis ( $\mu$ -SRXRF) and secondary ion mass spectrometry (SIMS). *Eur J Mineral* 17:233-242
- Haller M, Knöchel A (1996) X-ray fluorescence analysis using synchrotron radiation (SYXRF). *J Trace Microprobe Techniques* 14:461-488
- Haller M, Knöchel A, Radtke M (1995) New glass capillary optics for the SYXRF microprobe. *Hasylab Annual Report* 2:993-994
- Hansteen TH, Sachs PM, Lechtenberg F (2000) Synchrotron-XRF microprobe analysis of silicate reference standards using fundamental-parameter quantification. *Eur J Mineral* 12:25-31
- Harrison TM (1981) Diffusion of <sup>40</sup>Ar in hornblende. *Contrib Mineral Petrol* 78:324-331
- Hauri E, Wang J, Dixon JE, King PL, Mandeville C, Newman S (2002) SIMS analysis of volatiles in silicate glasses I. Calibration, matrix effects and comparisons with FTIR. *Chem Geol* 183:99-114
- Hayashi T, Muehlenbachs K (1986) Rapid oxygen diffusion in melilite and its relevance to meteorites. *Geochim Cosmochim Acta* 50:585-591
- Hervig RL (1996) Analyses of geological materials for boron by secondary ion mass spectrometry. *Rev Mineral* 33:789-803
- Hervig RL, Williams P (1986) Non-oxygen negative ion beams for oxygen isotopic analysis in insulators. *In: Secondary Ion Mass Spectrometry, SIMS V*. Benninghoven A, Colton RJ, Simons DS., Werner HW (eds), p. 152-154. Springer Verlag, Heidelberg
- Hervig RL, Mazdab FK, Danielson LR, Sharp TG, Hamed A, Williams P (2004) SIMS microanalyses for Au in silicates. *Am Mineral* 89:498-504
- Hervig RL, Mazdab FK, Williams P, Guan Y, Huss GR, Leshin LA (2006) Useful ion yields for Cameca IMS 3f and 6f SIMS: Limits on quantitative analysis. *Chem Geol* 227:83-99
- Hervig RL, Thomas RM, Williams P (1989) Charge neutralization and oxygen isotope analysis of insulators using the ion microprobe. *US Geol Surv Bull* 1890:137-143
- Hervig RL, Williams P, Thomas RM, Schauer SN, Steele IM (1992) Microanalysis of oxygen isotopes in insulators by secondary ion mass spectrometry. *Int J Mass Spec Ion Proc* 120:45-63
- Hoepfner UD, Kramar UE, Puchelt H (1990) Sulphur isotope exchange between sulphides and fluid sulphur; consequences for geothermometric application. *Eur J Mineral* 2:655-665
- Hofmann AW, Magaritz M (1977) Diffusion of Ca, Sr, Ba, and Co in a basalt melt; implications for the geochemistry of the mantle. *J Geophys Res* 82:5432-5440
- Houlier B, Cheraghmakani M, Jaoul O (1990) Silicon diffusion in San Carlos olivine. *Phys Earth Planet Inter* 62:329-340

- Houlier B, Jaoul O, Abel F, Liebermann RC (1988) Oxygen and silicon self-diffusion in natural olivine at T = 1300°C. *Phys Earth Planet Inter* 50:240-250
- Hui H, Zhang Y, Xu Z, Del Gaudio P, Behrens H (2009) Pressure dependence of viscosity of rhyolitic melts. *Geochim Cosmochim Acta* 73:3680-3693
- Ihinger PD, Hervig RL, McMillan PF (1994) Analytical methods for volatiles in glasses. *Rev Mineral* 30:67-121
- Ihinger PD, Zhang Y, Stolper EM (1999) The speciation of dissolved water in rhyolitic melt. *Geochim Cosmochim Acta* 63:3567-3578
- Ingrin J, Hercule S, Charton T (1995) Diffusion of hydrogen in diopside: results of dehydration experiments. *J Geophys Res* 100:15489-15499
- International Commission on Radiation Units and Measurements (1984) International Commission on Radiation Units and Measurements (ICRU) Report 37, Stopping Powers for Electrons and Positrons. ICRU, Bethesda, MD
- Ito M, Ganguly J (2006) Diffusion kinetics of Cr in olivine and  $^{53}\text{Mn}$ - $^{53}\text{Cr}$  thermochronology of early solar system objects. *Geochim Cosmochim Acta* 70:799-809
- Jambon A (1983) Diffusion dans les silicates fondus; un bilan des connaissances actuelles (Diffusion in silicates melts; a review). Conference on liquid silicates. *Bulletin de Mineralogie* 106:229-246
- Janssens K, Adams F, Rindby A (2000) Microscopic X-ray Fluorescence Analysis. Wiley, Chichester
- Jaoul O, Béjina F, Élie F, Abel F (1995b) Silicon self-diffusion in quartz. *Phys Rev Lett* 74:2038-2041
- Jaoul O, Bertran-Alvarez Y, Liebermann RC, Price GD (1995a) Fe-Mg interdiffusion in olivine up to 9 GPa at T = 600-900°C; experimental data and comparison with defect calculations. *Phys Earth Planet Inter* 89:199-218
- Jaoul O, Froidevaux C, Durham WB, Michaut M (1980) Oxygen self-diffusion in forsterite: implications for the high-temperature creep mechanism. *Earth Planet Sci Lett* 47:391-397
- Kelley SP (2006) High spatial resolution analysis of noble gases using UV lasers. Abstracts of the 16th annual V. M. Goldschmidt conference. *Geochim Cosmochim Acta* 70, 18S, A311
- Knoll M, Ruska E (1932) Electron microscope. *Z Physik* 78:318-339
- Koenig AE (2008) Advances in quantitative elemental analyses by laser ablation ICP-MS. *Microsc Microanal* 14(Suppl 2):170-171
- Koepke J, Behrens H (2001) Trace element diffusion in andesitic melts: An application of synchrotron X-ray fluorescence analysis. *Geochim Cosmochim Acta* 65:1481-1498
- Koepke J, Falkenberg G, Rickers K, Diedrich O (2003) Trace element diffusion and element partitioning between garnet and andesite melt using synchrotron X-ray fluorescence microanalysis ( $\mu$ -SRXRF). *Eur J Mineral* 15:883-892
- Lanford WA, Bedell S, Amadon S, Haberl A, Skala W, Hjorvarsson B (2000) Characteristics of Albany's compact high-resolution magnetic spectrometer. *Nucl Instrum Methods B* 161-163:202-206
- Laursen T, Lanford WA (1978) Hydration of obsidian. *Nature* 276:153-156
- Leavitt JA, McIntyre Jr. LC (1991) Non-Rutherford  $^4\text{He}$  cross sections for ion beam analysis. *Nucl Instrum Methods B* 56-57:734-739
- Leavitt JA, McIntyre Jr. LC (1995) Backscattering Spectrometry. *In: Handbook of Modern Ion Beam Materials Analysis*. Tesmer JR, Nastasi MA (eds) Materials Research Society, p 37-81
- Leshner CE, Hervig RL, Tinker D (1996) Self diffusion of network formers (Si and O) in naturally occurring aluminosilicate liquids. *Geochim Cosmochim Acta* 60:405-413
- Libowitzky E, Rossman GR (1996) Principles of quantitative absorbance measurements in anisotropic crystals. *Phys Chem Miner* 23:319-327
- Lin TH, Yund RA (1972) Potassium and sodium self-diffusion in alkali feldspar. *Contrib Mineral Petrol* 34:177-184
- Lindner R, Parfitt GD (1957) Diffusion of radioactive magnesium in magnesium oxide crystals. *J Chem Phys* 26:182-185
- Liu M, Yund RA (1992) NaSi-CaAl interdiffusion in plagioclase. *Am Mineral* 77:275-283
- Liu Y, Behrens H, Zhang Y (2004a) The speciation of dissolved H<sub>2</sub>O in dacitic melt. *Am Mineral* 89:277-284
- Liu Y, Zhang Y, Behrens H (2004b) H<sub>2</sub>O diffusion in dacitic melt. *Chem Geol* 209, 327-340
- Liu Y, Zhang Y, Behrens H. (2005) Solubility of H<sub>2</sub>O in rhyolitic melts at low pressures and a new empirical model for mixed H<sub>2</sub>O-CO<sub>2</sub> solubility in rhyolitic melts. *J Volcanol Geotherm Res* 143:219-235
- Lovera OM, Richter FM, Harrison TM (1991) Diffusion domains determined by  $^{39}\text{Ar}$  released during step heating. *J Geophys Res* 96 (B2):2057-2069
- Mackwell SJ, Kohlstedt DJ (1990) Diffusion of hydrogen in olivine: implications for water in the mantle. *J Geophys Res* 95(B4):5079-5088
- MacRae CM, Wilson NC, Notoya S (2006) Improvements in Mapping and Microanalysis by FEG-EPMA. *Microsc Microanal* 12 (Suppl. 2): 1378 CD
- Magaritz M, Hofmann AW (1978a) Diffusion of Sr, Ba and Na in obsidian. *Geochim Cosmochim Acta* 42:595-606

- Magaritz M, Hofmann AW (1978b) Diffusion of Eu and Gd in basalt and obsidian. *Geochim Cosmochim Acta* 42:847-858
- Martin P, Carlot G, Chevarier A, Den-Auwer C, Panczer G (1999) Mechanisms involved in thermal diffusion of rare earth elements in apatite. *J Nucl Mater* 275:268-276
- McCormell JDC (1995) The role of water in oxygen isotope exchange in quartz. *Earth Planet Sci Lett* 136:97-107
- McDougall I, Harrison TM (1999) *Geochronology and Thermochronology by the  $^{40}\text{Ar}/^{39}\text{Ar}$  Method*. Oxford University Press, New York
- McKay HAC (1938) Self-diffusion coefficient of gold [with discussion]. *Trans Faraday Soc* 34:845-850
- Medford GA (1973) Calcium diffusion in a mugearite melt. *Can J Earth Sci* 10:394-402
- Mehrer H (2007) *Diffusion in Solids: Fundamentals, Methods, Materials, Diffusion-Controlled Processes*. Volume 155 of Springer series in Solid-State Sciences. Springer
- Melcher CL, Tombrello TA, Burnett DS (1983) *Geochim Cosmochim Acta* 47:1707-1712
- Miller Jr. PH, Banks FR (1942) Self-diffusion of zinc. *Phys Rev* 61:648-652
- Miro S, Studer F, Costantini JM, Huassy J, Trouslard P, Grob JJ (2006) Effect of composition on helium diffusion in fluorapatites investigated with nuclear reaction analysis. *J Nucl Mater* 355:1-9
- Montasser A (1998) *Inductively Coupled Plasma Mass Spectrometry*. Wiley-VCH
- Moore DK, Cherniak DJ, Watson EB (1998) Oxygen diffusion in rutile from 750 to 1000 °C and 0.1 to 1000 MPa. *Am Mineral* 83:700-711
- Moore G, Chizmeshya A, McMillian PF (2000) Calibration of a reflectance FTIR method for determination of dissolved CO<sub>2</sub> concentration in rhyolitic glasses. *Geochim Cosmochim Acta* 64:3571-3579
- Morioka M, Kamata Y, Nagasawa H (1997) Diffusion in single crystals of melilite: III. Divalent cations in gehlenite. *Geochim Cosmochim Acta* 61:1009-1016
- Morioka M, Nagasawa H (1991) Diffusion in single crystals of melilite. II. Cations. *Geochim Cosmochim Acta* 55:751-759
- Moseley HGJ (1913) High frequency spectra of the elements. *Philos Mag* 26:1024-1034
- Mungall JE, Dingwell DB, Chaussidon M (1999) Chemical diffusivities of 18 trace elements in granitoid melts. *Geochim Cosmochim Acta* 63:2599-2610
- Nastasi M, Mayer JW (1994) Ion beam mixing in metallic and semiconductor materials. *Mat Sci Eng R12*:1-52
- Nelms S (ed) (2005) *Inductively Coupled Plasma Mass Spectrometry Handbook*. Blackwell
- Newman S, Stolper EM, Epstein S (1986) Measurement of water in rhyolitic glasses: calibration of an infrared spectroscopic technique. *Am Mineral* 71:1527-1541
- Ni H, Behrens H, Zhang Y (2009b) Water diffusion in dacitic melt. *Geochim Cosmochim Acta* 73:3642-3655
- Ni H, Liu Y, Wang, L, Zhang Y (2009a) Water speciation and diffusion in haploandesitic melts at 743-873 K and 100 MPa. *Geochim Cosmochim Acta* 73:3630-3641
- Ni H, Zhang Y (2008) H<sub>2</sub>O diffusion models in rhyolitic melt with new high pressure data. *Chem Geol* 250:68-78
- Nogami M, Tomozawa M (1984) Diffusion of water in high silica glasses at low temperature. *Phys Chem Glasses* 25:82-85
- Nowak M, Schreen D, Spickenbom K (2004) Argon and CO<sub>2</sub> on the race track in silicate melts: a tool for the development of a CO<sub>2</sub> speciation and diffusion model. *Geochim Cosmochim Acta* 68:5127-5138
- Oberstar JD, Streetman BG, Baker JE, Williams P (1982) SIMS studies of <sup>9</sup>Be implants in semi-insulating InP. *J Electrochem Soc: Solid-State Sci Tech* 129:1312-1320
- Ohlhorst S, Behrens H, Holtz F (2001) Compositional dependence of molar absorptivities of near-infrared OH- and H<sub>2</sub>O bands in rhyolitic to basaltic glasses. *Chem Geol* 174:5-20
- Ouchani S, Dran JC, Chaumont J (1998) Exfoliation and diffusion following helium ion implantation in fluorapatite: implications for radiochronology and radioactive waste disposal. *Appl Geochem* 13:707-714
- Pankrath R, Flörke OW (1994) Kinetics of Al-Si exchange in low and high quartz: calculation of Al diffusion coefficients. *Eur J Mineral* 6:435-457
- Paterson MS (1986) The thermodynamics of water in quartz. *Phys Chem Miner* 13:245-255
- Peterson NL, Chen WK, Wolf D (1980) Correlation and isotope effects for cation diffusion in magnetite. *J Phys Chem Solids* 41:709-719
- Petit JC, Dran JC, Della Mea G (1990) Energetic ion beam analysis in the earth sciences. *Nature* 344:621-626
- Potts PJ (1987) *A handbook of Silicate Rock Analysis*. Chapman and Hall, New York. 622 pp
- Pouchou JL, Pichoir F (1986a) Basic expression of "PAP" computation for quantitative EMPA. *In: 11th Intl Congress on X-ray Optics and Microanalysis*. 249. Brown JD, Packwood RH (eds) Graphic Services U.W.O., London, Canada, p 249-253
- Pouchou JL, Pichoir F (1986b) Very light elements X-ray microanalysis. Recent models of quantification. *Journal de Microscopie et de Spectroscopie Electronique* 11:229-250
- Pouchou JL, Pichoir F (1988) A simplified version of the "PAP" model for matrix corrections in EPMA. *In: Microbeam Analysis*. Newbury DE (ed) San Francisco Press, p 315-318

- Pouchou JL, Pichoir F (1991) Quantitative analysis of homogeneous or stratified microvolumes applying the model "PAP". *In: Electron Probe Quantitation*. Heinrich KFJ, Newbury DE (eds) Plenum Press, p 31-75
- Reddy KPR, Oh SM, Major jr. LD, Cooper AR (1980) Oxygen diffusion in forsterite. *J Geophys Res* 85 B1:322-326
- Reed SJB (1993) *Electron Microprobe Analysis* (2nd Ed.) Cambridge University Press
- Reed SJB (2005) *Electron Microprobe Analysis and Scanning Electron Microscopy in Geology* (2nd Ed.). Cambridge University Press
- Reed, SJB (1995) *Electron Microprobe Microanalysis*. *In: Microprobe Techniques in the Earth Sciences*. The Mineralogical Society Series, Volume 6. Potts PJ, Bowles JFW, Reed SJB, Cave MR (eds) Chapman and Hall, p 49-90
- Reiners PW, Farley KA (1999) Helium diffusion and (U-Th)/He thermochronometry of titanite. *Geochim Cosmochim Acta* 63:3845-3859
- Reiners PW, Spell TL, Nicolescu S, Zanetti KA (2004) Zircon (U-Th)/He thermochronometry. He diffusion and comparisons with  $^{40}\text{Ar}/^{39}\text{Ar}$  dating. *Geochim Cosmochim Acta* 68:1857-1887
- Richet P, Whittington A, Holtz F, Behrens H, Ohlhorst S, Wilke M (2000) Water and the density of silicate glasses. *Contrib Mineral Petrol* 138:337-347
- Richter FM, Davis, AM, DePaolo DJ, Watson EB (2003) Isotope fractionation by chemical diffusion between molten basalt and rhyolite. *Geochim Cosmochim Acta* 67:3905-3923
- Righter K, Campbell AJ, Humayun M (2005) Diffusion of trace elements in FeNi metal; application to zoned metal grains in chondrites. *Geochim Cosmochim Acta* 69:3145-3158
- Rossmann GR (1988) Vibrational spectroscopy of hydrous components. *Rev Mineral* 18:193-206
- Ryerson FJ (1987) Diffusion measurements; experimental methods. *In: Geophysics; Part A, Laboratory Measurements*. *Methods of Experimental Physics*, Vol. 24. Sammis CG, Henyey TL (eds) Academic Press, New York, p 89-130
- Ryerson FJ, Durham WB, Cherniak DJ, Lanford WA (1989) Oxygen diffusion in olivine: Effect of oxygen fugacity and implications for creep. *J Geophys Res* 94:4105-4118
- Saal AE, Hauri EH, Cascio ML, Van Orman JA, Rutherford MJ, Cooper RF (2008) Volatile content of lunar volcanic glasses and the presence of water in the Moon's interior. *Nature* 454:192-196
- Sautter V, Jaoul O, Abel F (1988) Aluminum diffusion in diopside using the  $^{27}\text{Al}(p,\gamma)^{28}\text{Si}$  nuclear reaction: preliminary results. *Earth Planet Sci Lett* 89:109-114
- Schauer SN, Williams P (1990) Elimination of cluster interferences in secondary ion mass spectrometry using extreme energy filtering. *Int J Mass Spectrom Ion Proc* 103:21-29
- Schmidt BC, Behrens H, Riemer T, Kappes R, Dupree R (2001) Quantitative determination of water speciation in aluminosilicate glasses: a comparative NMR and IR spectroscopic study. *Chem Geol* 174:195-208
- Seitz MG (1973) Uranium and thorium diffusion in diopside and fluorapatite. *Year Book - Carnegie Institution of Washington* 72, p 586-588
- Shang LB, Chou IM, Lu WJ, Burruss RC, Zhang Y (2009) Determination of diffusion coefficients of hydrogen in fused silica between 296 and 523 K by Raman spectroscopy and application of fused silica capillaries in studying redox reactions. *Geochim Cosmochim Acta* 73:5435-5443
- Shimizu N, Semet MP, Allègre CJ (1978) Geochemical applications of quantitative ion-microprobe analysis. *Geochim Cosmochim Acta* 42:1321-1334
- Shuster DL, Farley KA, Sisterson JM, Burnett DS (2003) Quantifying the diffusion kinetics and spatial distribution of radiogenic  $^4\text{He}$  in minerals containing proton-induced  $^3\text{He}$ . *Earth Planet Sci Lett* 217:19-32
- Sierralta M, Nowak M, Keppler H (2002) The influence of bulk composition on the diffusivity of carbon dioxide in Na aluminosilicate melts. *Am Mineral* 87:1710-1716
- Sippel RF (1963) Sodium self diffusion in natural minerals. *Geochim Cosmochim Acta* 27:107-120
- Skogby H, Rossmann GR (1989)  $\text{OH}^-$  in pyroxene: An experimental study of incorporation mechanisms and stability. *Am Mineral* 74:1059-1069
- Smets J, Lommen TPA (1983) The role of molecular water in the leaching of glasses. *Phys Chem Glasses* 24:35-36
- Smith DG (1976) *Short Course in Microbeam Techniques*. Mineralogical Association of Canada
- Smith JV, Rivers ML (1995) Synchrotron X-ray microanalysis. *In: Microprobe Techniques in the Earth Sciences*. Potts PJ, Bowles JFW, Reed SJB, Cave MR (eds) Chapman and Hall, London, p 163-233
- Sneeringer M, Hart SR, Shimizu N (1984) Strontium and samarium diffusion in diopside. *Geochim Cosmochim Acta* 48:1589-1608
- Sobers Jr. RC, Franzreb K, Williams P (2004) Quantitative measurement of O/Si ratios in oxygen-sputtered silicon using  $^{18}\text{O}$  implant standards. *Appl Surf Sci* 231-232:729-733
- Spandler C, O'Neill HSC, Kamenetsky KS (2007) Survival times of anomalous melt inclusions from element diffusion in olivine and chromite. *Nature* 447:303-306
- Stanton TR (1989) High pressure, isotopic studies of the water diffusion mechanism in silicate melts and glasses. Ph.D. dissertation, Department of Chemistry, Arizona State University, Tempe

- Steele IM, Hervig RL, Hutcheon ID, Smith JV (1981) Ion microprobe techniques and analyses of olivine and low-Ca pyroxene. *Am Mineral* 66:526-546
- Stolper EM (1982a) Water in silicate glasses: an infrared spectroscopic study. *Contrib Mineral Petrol* 81:1-17
- Stolper EM (1982b) The speciation of water in silicate melts. *Geochim Cosmochim Acta* 46:2609-2620
- Sutton SR, Bertsch PM, Newville M, Rivers ML, Lanzirotti A, Eng P (2002) Microfluorescence and microtomography analyses of heterogeneous earth and environmental materials. *Rev Mineral Geochem* 49:429-483
- Sylvester PJ (ed) (2001) *Laser-ablation-ICPMS in the Earth Sciences: Principles and Applications*. Mineralogical Association of Canada
- Sylvester PJ (ed) (2008) *Laser Ablation ICP-MS in the Earth Sciences: Current Practices and Outstanding Issues*. Mineralogical Association of Canada
- Tamic N, Behrens H, Holtz F (2001) The solubility of H<sub>2</sub>O and CO<sub>2</sub> in rhyolitic melts in equilibrium with a mixed CO<sub>2</sub>-H<sub>2</sub>O fluid phase. *Chem Geol* 174:333-347
- Taylor HE (2000) *Inductively Coupled Plasma-Mass Spectrometry*. Academic Press
- Tenner TJ, Hirschmann M, Withers AC, Hervig RL (2009) Hydrogen partitioning between nominally anhydrous upper mantle minerals and melt between 3 and 5 GPa and applications to hydrous peridotite partial melting. *Chem Geol* 262:42-56
- ter Heege JH, Dohmen R, Becker H, Chakraborty S (2006) Experimental determination of Fe-Mg interdiffusion coefficients in orthopyroxene using pulsed laser ablation and nanoscale thin films. *Eos, Transactions, American Geophysical Union*, December 2006, Vol. 87, Issue Fall Meeting Suppl
- Tesmer JR, Nastasi MA (eds) (1995) *Handbook of Modern Ion Beam Materials Analysis*. Materials Research Society
- Thomas JB, Cherniak DJ, Watson EB (2008) Lattice diffusion and solubility of argon in forsterite, enstatite, periclase, quartz and corundum. *Chem Geol* 253:1-22
- Thomas R (2000) Determination of water contents of granite melt inclusions by confocal laser Raman microprobe spectroscopy. *Am Mineral* 85:868-872
- Thomas R (2008) *A Practical Guide to ICP-MS* CRC Press, Boca Raton
- Thomas SM, Thomas R, Davidson P, Reichart P, Koch-Muller M, Dollinger G (2008) Application of Raman spectroscopy to quantify trace water concentrations in glasses and garnets. *Am Mineral* 93:1550-1557
- Toulhoat N, Potocek V, Neskovic C, Federoff M, Jeanjean J, Vincent U (1996) Perspectives for the study of the diffusion of radionuclides into minerals using the nuclear microprobe techniques. *Radiochim Acta* 74:257-262
- Tsai MY, Day DS, Streetman BG, Williams P, Evans CAJ (1979) Recrystallization of implanted amorphous silicon layers II. Migration of fluorine in BF<sub>2</sub><sup>+</sup>-implanted silicon. *J Appl Phys* 50:188-192
- Turek A, Riddle C, Cozens BJ, Tetley NW (1976) Determination of chemical water in rock analysis by Karl Fischer titration. *Chem Geol* 17:261-267
- Vad K, Csik A, Langer GA (2009) Secondary neutral mass spectrometry - a powerful technique for quantitative elemental and depth profiling analyses of nanostructure. *Spectroscopy Europe* 21:13-16
- Van Der Laan SR, Zhang Y, Kennedy A, Wylie PJ (1994) Comparison of element and isotope diffusion of K and Ca in multicomponent silicate melts. *Earth Planet Sci Lett* 123:155-166
- Van Espen PJ, Nullens H., Adams F (1977) A computer analysis of X-ray fluorescence spectra. *Nucl Instrum Method* 142:269-273
- Van Orman JA, Grove TL, Shimizu N (2001) Rare earth element diffusion in diopside: influence of temperature, pressure, and ionic radius, and an elastic model for diffusion. *Contrib Mineral Petrol* 141:687-703
- Verhoogen J (1952) Ionic diffusion and electrical conductivity in quartz. *Am Mineral* 37:637-655
- Wallace PJ, Dufek J, Anderson AT, Zhang Y (2003) Cooling rates of Plinian-fall and pyroclastic-flow deposits in the Bishop Tuff: inferences from water speciation in quartz-hosted glass inclusions. *Bull Volcanol* 65:105-123
- Wang H, Xu Z, Behrens H, Zhang Y (2009) Water diffusion in Mount Changbai peralkaline rhyolitic melt. *Contrib Mineral Petrol* 158:471-484
- Wang L, Zhang Y, Essene EJ (1996) Diffusion of the hydrous component in pyrope. *Am Mineral* 81:706-718
- Wark DA, Watson EB (2006) TitanQ: a titanium-in-quartz geothermometer. *Contrib Mineral Petrol* 152:743-754
- Wartho J, Kelley SP, Brooker RA, Carroll MR, Villa IM, Lee MR (1999) Direct measurement of Ar diffusion profiles in a gem-quality Madagascar K-feldspar using the ultra-violet laser ablation microprobe (UVLAMP). *Earth Planet Sci Lett* 170:141-153
- Watson EB, Dohmen R (2010) Non-traditional and emerging methods for characterizing diffusion in minerals and mineral aggregates. *Rev Mineral Geochem* 72:61-105
- Watson EB (1979a) Calcium diffusion in a simple silicate melt to 30 kbar. *Geochim Cosmochim Acta* 43:313-322
- Watson EB (1979b) Diffusion of cesium ions in H<sub>2</sub>O-saturated granitic melt. *Science* 205:1259-1260
- Watson EB, Cherniak DJ (1997) Oxygen diffusion in zircon. *Earth Planet Sci Lett* 148:527-544

- Watson EB, Cherniak DJ (2003) Lattice diffusion in quartz, with constraints on Ar solubility and evidence of nanopores. *Geochim Cosmochim Acta* 67:2043-2062
- Watson EB, Cherniak DJ, Frank EA (2009) Retention of biosignatures and mass-independent fractionations in pyrite: Self-diffusion of sulfur. *Geochim Cosmochim Acta* 73:4792-4802
- Watson EB, Sneeringer MA, Ross A (1982) Diffusion of dissolved carbonate in magmas; experimental results and applications. *Earth Planet Sci Lett* 61, 346-358
- Watson EB, Thomas JB, Cherniak DJ (2007) <sup>40</sup>Ar retention in the terrestrial planets. *Nature* 449:299-304
- Westrich HR (1987) Determination of water in volcanic glasses by Karl-Fischer titration. *Chem Geol* 63:335-340
- Williams DB, Carter CB (1996) *Transmission Electron Microscopy (First Edition)*. Plenum Press
- Williams P (1983) Secondary ion mass spectrometry. *In: Applied Atomic Collision Physics*, 4. Datz S (ed) Academic Press, New York, p 327-377
- Williams P, Streit LA (1986) Quantitative analysis using sputtered neutrals in a secondary ion microanalyzer. *Nucl Instrum Methods B* 15:159-164
- Wilson RG (1984) Depth distributions of sulfur implanted into silicon as a function of ion energy, ion fluence, and anneal temperature. *J Appl Phys* 55:3490-3494
- Wolf RW, Farley KA, Silver LT (1996) Helium diffusion and low temperature thermochronometry of apatite. *Geochim Cosmochim Acta* 60:4231-4240
- Yamashita S, Behrens H, Schmidt BC, Dupree R (2008) Water speciation in sodium silicate glasses based on NIR and NMR spectroscopy. *Chem Geol* 256:231-241
- Yund RA (1986) Interdiffusion of NaSi-CaAl in peristerite. *Phys Chem Mineral* 13:11-16
- Zhang XY, Cherniak DJ, Watson EB (2006) Oxygen diffusion in titanite: lattice diffusion and fast-path diffusion in single crystals. *Chem Geol* 235:105-123
- Zhang Y (1999) H<sub>2</sub>O in rhyolitic glasses and melts: measurement, speciation, solubility, and diffusion. *Rev Geophys* 37:493-516
- Zhang Y (2008) *Geochemical Kinetics*. Princeton University Press, Princeton, NJ
- Zhang Y, Behrens H (2000) H<sub>2</sub>O diffusion in rhyolitic melts and glasses. *Chem Geol* 169:243-262
- Zhang Y, Belcher R, Ihinger PD, Wang L, Xu Z, Newman S (1997) New calibration of infrared measurement of water in rhyolitic glasses. *Geochim Cosmochim Acta* 61:3089-3100
- Zhang Y, Jenkins J, Xu Z (1997b) Kinetics of the reaction H<sub>2</sub>O + O = 2OH in rhyolitic glasses upon cooling: geospeedometry and comparison with glass transition. *Geochim Cosmochim Acta* 61:2167-2173
- Zhang Y, Stolper EM (1991) Water diffusion in basaltic melts. *Nature* 351:306-309
- Zhang Y, Stolper EM, Wasserburg GJ (1991a) Diffusion of water in rhyolitic glasses. *Geochim Cosmochim Acta* 55:441-456
- Zhang Y, Stolper EM, Wasserburg GJ (1991b) Diffusion of a multi-species component and its role in the diffusion of water and oxygen in silicates. *Earth Planet Sci Lett* 103:228-240
- Zhang Y, Xu Z, Behrens H (2000) Hydrous species geospeedometer in rhyolite: improved calibration and application. *Geochim Cosmochim Acta* 64:3347-3355
- Zhao D (1998) *Diamonds and mantle xenoliths in kimberlites from the North China Craton and the Canadian Northwest Territories*. Ph.D. Thesis. Univ. of Michigan
- Ziegler JF, Biersack JP (2006) The stopping and range of ions in matter. Computer code SRIM 2006, <http://www.srim.org>
- Ziegler JF, Biersack JP, Littmark U (1985) *Stopping and range of ions in solids*. Pergamon Press, New York
- Zinner E, Crozaz G (1986) A method for the quantitative measurement of rare earth elements in the ion microprobe. *Int J Mass Spec Ion Proc* 69:17-38

